



| | |
|--------------|--|
| Title | Electrical detection of magnetic fluctuations in nanoscale frustrated magnetic materials |
| Author(s) | 谷口, 祐紀 |
| Citation | 大阪大学, 2020, 博士論文 |
| Version Type | VoR |
| URL | https://doi.org/10.18910/76369 |
| rights | |
| Note | |

The University of Osaka Institutional Knowledge Archive : OUKA

<https://ir.library.osaka-u.ac.jp/>

The University of Osaka

Electrical detection of magnetic fluctuations in nanoscale frustrated magnetic materials

Hiroki Taniguchi

2020/02/03

Contents

| | | |
|-----------|---|-----------|
| I | Frustrated magnetic systems | 2 |
| 1 | Spin glasses | 3 |
| 1.1 | History of spin glasses | 3 |
| 1.1.1 | Randomness and frustration in spin glasses | 5 |
| 1.1.2 | Mean field theory of spin glasses | 6 |
| 1.2 | Determination of T_f | 11 |
| 1.3 | Electrical conductivity in spin glasses | 14 |
| 2 | Triangular antiferromagnet | 17 |
| 2.1 | Frustration on triangular antiferromagnet | 17 |
| 2.2 | Ising triangular antiferromagnet | 19 |
| 2.3 | Basic properties of Ag_2CrO_2 | 21 |
| 2.3.1 | Crystal structure | 21 |
| 2.3.2 | Magnetization measurement | 22 |
| 2.3.3 | Specific heat measurement | 23 |
| 2.3.4 | Electrical conductivity | 24 |
| 2.3.5 | Neutron scattering measurement | 26 |
| II | Spin transport measurement | 28 |
| 3 | Spintronics | 29 |
| 3.1 | History of spintronics | 29 |
| 3.1.1 | Giant magnetoresistance | 29 |
| 3.1.2 | Nonlocal spin valve | 32 |
| 3.2 | Spin Hall effect | 36 |
| 3.2.1 | Spin Hall effect in magnetic materials | 41 |
| 3.2.2 | Spin Hall effect near the magnetic transition | 42 |
| 3.3 | Theory of anomalous Hall effect | 45 |
| 3.3.1 | Intrinsic mechanism | 45 |
| 3.3.2 | Extrinsic mechanism | 48 |
| 3.3.3 | Scaling relation | 54 |
| 3.3.4 | Relation between anomalous Hall effect and spin Hall effect | 56 |
| 3.4 | One-dimensional Spin diffusion model | 58 |
| 3.4.1 | Nonlocal spin valve | 58 |

| | | |
|------------|--|------------|
| 3.4.2 | Nonlocal spin valve with a middle wire | 61 |
| 3.4.3 | Spin Hall measurement using Spin Absorption Method | 62 |
| 4 | Purpose of this thesis | 64 |
| III | Experimental results | 65 |
| 5 | Experimental setup | 66 |
| 5.1 | Nanofabrication method | 66 |
| 5.1.1 | Lift off method | 66 |
| 5.1.2 | Evaporation methods of thin films | 69 |
| 5.1.3 | Fabrication of nonlocal spin valve device | 71 |
| 5.1.4 | Measurement setup | 76 |
| 5.2 | Nonlocal spin valve measurements without middle wire | 77 |
| 6 | Spin transport measurement in Spin Glass | 81 |
| 6.1 | <i>dc</i> magnetization of CuMnBi | 81 |
| 6.2 | Extraordinary Hall effect of CuMnBi | 84 |
| 6.2.1 | The surface effect of Bi impurities | 87 |
| 6.3 | Inverse spin Hall effect in CuMnBi | 88 |
| 6.3.1 | Spin Hall angle of CuMnBi | 91 |
| 6.3.2 | Discussion: origin of reduction of inverse spin Hall effect | 92 |
| 6.3.3 | Spin treacle region | 94 |
| 6.3.4 | Spin diffusion length of CuMnBi | 97 |
| 7 | Detection of Spin Fluctuations in Ag₂CrO₂ | 100 |
| 7.1 | Fabrication of Ag ₂ CrO ₂ thin film | 100 |
| 7.2 | STEM | 102 |
| 7.3 | Electrical transport measurements | 103 |
| 7.3.1 | Transport properties of Ag ₂ CrO ₂ thin film | 103 |
| 7.3.2 | Magnetoresistance | 104 |
| 7.3.3 | Discussion: origin of the magnetoresistance | 108 |
| 7.3.4 | Hall effect | 111 |
| 8 | Conclusions and perspectives | 114 |
| | Appendix | 117 |
| | References | 121 |
| | Acknowledgements | 128 |

Abstract

Frustration is a situation where various optimization conditions compete with each other, and thus the system cannot satisfy them simultaneously. The frustration in magnetic materials is induced by competition of various interactions between magnetic moments. Such frustration generates large and unusual fluctuations in magnetically-frustrated systems. As a result, new ordered phases, thermodynamic states, and peculiar non-equilibrium dynamics appear in frustrated magnetic materials. Thus, the magnetically-frustrated system is one of the important research topics in modern condensed matter physics [1–4].

On the other hand, a research field “spintronics” is rapidly growing in recent years. Spintronics is based on the conventional electronics with use of the spin degree of freedom. The most important concept of spintronics is “pure spin current” that is the flow of spin angular momentum without a charge flow. Unlike a charge current, a pure spin current cannot be detected by ordinary electrical measurements because it is not a conserved quantity. The spin Hall effect (SHE) and its inverse (ISHE) enable us to generate and detect the pure spin current [5–11]. In particular, the ISHE is modulated near the magnetic transition temperature where spin fluctuations are strong [12]. This result indicates that there is a strong correlation between spin fluctuations of the magnetic moment and the pure spin current. By using this correlation, the pure spin current can be used as a new probe to investigate the spin dynamics in frustrated magnetic systems.

To demonstrate the impact of the pure spin current on magnetically-frustrated systems, we have chosen the following two frustrated magnetic materials. The first one is the spin glass system. Spin glass is one of the magnetic ordering states with complex spin structures. When magnetic atoms are randomly distributed in a host non-magnetic metal, and this randomness induces magnetic frustration. As a result, a unique cusp structure appears in the temperature dependence of magnetization at low temperatures. The cusp temperature is called “spin freezing temperature T_f ”. Since the discovery of spin glasses in 1970s, various theories and experiments have been conducted and the basic understanding of the system is well-established. It is commonly believed that most of localized moments in spin glasses are frozen below T_f . However, according to the recent work on the ISHE in $\text{Cu}_{99.5-x}\text{Mn}_x\text{Bi}_{0.5}$ [13], the spin Hall (SH) signal, that is the conversion yield between the spin current and charge current, starts to decrease at a temperature, which is 4 times higher than T_f determined from the magnetization measurement. Furthermore, the SH signal continuously decreases even below T_f . These facts indicate that finite spin fluctuations exist even below T_f and are not intuitively consistent with the conventional spin-glass picture. In order to deeply understand the relation between the spin current and spin-glass state, further experiments are highly desirable.

In this thesis, we have measured the ISHE of $\text{Cu}_{99.5-x}\text{Mn}_x\text{Bi}_{0.5}$ ($x = 4.2, 8.2,$ and 10.6) by using the spin absorption method [6]. With increasing the Mn concentration, T_f shifts to the higher temperature side. This enables us to investigate the effect of spin fluctuation below T_f in detail. We have observed a saturation of ISHE in the low temperature regime. The saturation originates from the depolarization of conduction electron spins due to randomly frozen localized moments. We conclude that the temperature at which the ISHE saturates corresponds to the real T_f of the spin-glass nanowire. This result also demonstrates that the spin transport measurement is a powerful method to determine the magnetic transition temperature of nanometer-scale magnet which is difficult to measure by conventional magnetization measurements. In addition, the temperature at which the ISHE starts to decrease is several times higher than T_f . Between this temperature and T_f , the localized moments are cooperatively fluctuated and this temperature region has never been characterized *quantitatively* in previous magnetization measurements. Thus, the present result is a clear demonstration that conduction electron spins can be used as a sensitive probe to detect fluctuations of localized moments.

The second target is the triangular antiferromagnetic system. It is a typical frustrated magnetic system due to its geometry and has been studied for a long time both from the experimental and theoretical viewpoints. Although most of the triangular antiferromagnetic materials are insulators, here we focus on an electrically conductive triangular antiferromagnet: Ag_2CrO_2 . This material exhibits a unique thermodynamic property, so-called *partially disordered* (PD) *state*, below the antiferromagnetic transition temperature $T_N = 24$ K [14–16]. However, the magnetic structure of the PD state is not still elucidated because the single crystal has not been synthesized yet.

In this thesis, we have fabricated a micrometer-size Ag_2CrO_2 device and measured its magnetotransport in order to investigate the effect of PD spin fluctuations on the electrical transport property. By establishing the mechanical exfoliation technique based on the scotch tape method [17], we have been able to fabricate a micrometer-size Ag_2CrO_2 , which is almost a single crystal, from the Ag_2CrO_2 polycrystalline sample [18]. We observed a clear butterfly-shaped magnetoresistance (MR) only when the magnetic field direction was out-of-plane. We compared this result with a theoretical model. It turned out that the unique MR originates from the strong spin fluctuations near T_N . Such a unique MR has never been observed in other antiferromagnets. We also measured a Hall effect and found an anomaly which might be related to the magnetic structure of the Ag_2CrO_2 . These results provide important information for understanding the spin state in the PD phase.

The results obtained in this thesis demonstrate the importance of electric and spin transport measurements in frustrated magnetic systems, and also provide an experimental milestone for investigating the magnetic dynamics.

Construction of thesis

First of all, we explain the research background of frustrated magnets in Part I. Part II is devoted to explain brief backgrounds about spin transport measurements and the motivation of our work. In Part III, we show experimental results on spin transport measurements in spin glasses and electrical conductivity measurements in Ag_2CrO_2 . Finally, we summarize this thesis and mention some perspectives in Part IV.

Abbreviations

| | |
|----------------|---|
| AH(E) | anomalous Hall (effect) |
| AMR | anisotropic magnetoresistance |
| DSHE | direct spin Hall effect |
| EHE | extraordinary Hall effect |
| ESR | electron spin resonance |
| ISHE | inverse spin Hall effect |
| MR | magnetoresistance |
| NLSV | nonlocal spin valve |
| NMR | nuclear magnetic resonance |
| PD | partially disordered |
| Py | permalloy |
| SEM | scanning electron microscope |
| SH(E) | spin Hall (effect) |
| SDL | spin diffusion length |
| SO(C) | spin – orbit (coupling) |
| SOI | spin – orbit interaction |
| STEM | scanning transmission electron microscope |
| μSR | muon spin rotation |
| (Z)FC | (zero) field cooling |

Part I

Frustrated magnetic systems

Chapter 1

Spin glasses

In Part I, we review spin glasses (in this chapter) and two-dimensional (2D) triangular antiferromagnets with classical spins (in the next chapter) as two typical magnetic frustrated systems.

Spin glasses are one of the magnetic ordering states with complex spin structures. For several decades, spin glasses have been extensively studied as a prototype of complex system characterized by frustration and randomness. Nowadays, the treatment of randomness based on spin-glass theorem is used not only in condensed matter physics but also in the field of quantum information such as quantum annealing [19] and neuromorphic computers.

In this chapter, we first review the history of spin glasses using some experimental results and also theoretical models with the mean field theory. After that, we explain the method to determine the spin freezing temperature T_f which is closely related to the present thesis.

1.1 History of spin glasses

Spin glasses were first reported by Cannella and Mydosh in 1972 [20]. They measured magnetic susceptibilities of diluted magnetic alloys $\text{Au}_{100-x}\text{Fe}_x$ and found a sharp cusp-like anomaly at low temperatures (see Fig 1.1). The cusp temperature is called “spin freezing temperature” T_f . It depends on the concentration of magnetic impurities. For instance, T_f is about 8 K for $\text{Au}_{99}\text{Fe}_1$ and increases with increasing the Fe concentration x . Such a cusp structure was observed not only in AuFe but also in AuMn, AgMn and CuMn. The combination of noble metals (Au, Ag, Cu) and magnetic impurities (Mn, Fe, ...) are called “canonical spin glasses”. They have been investigated so far as a prototype of complex system characterized by frustration and randomness.

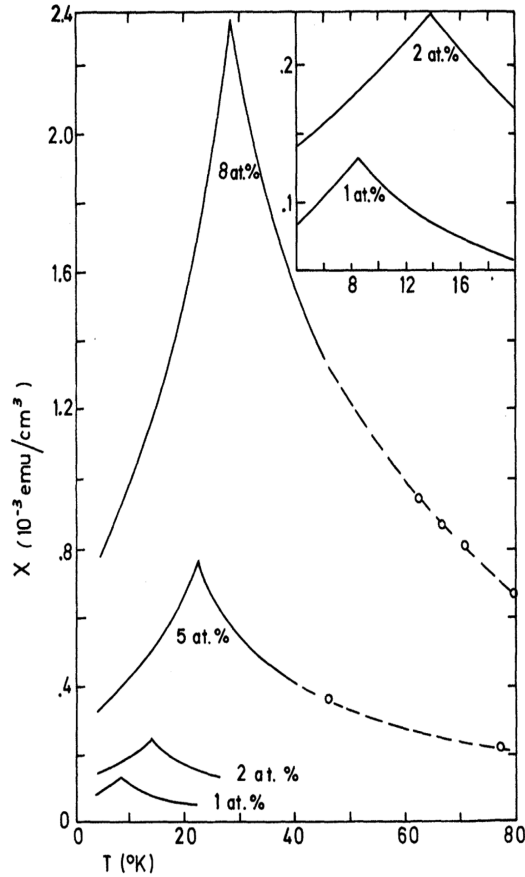


Figure 1.1: Magnetic susceptibility χ of $\text{Au}_{100-x}\text{Fe}_x$ as a function of temperature [20].

Another important character of spin glasses appears in the cooling process. As shown in Fig. 1.2, the dc magnetization takes a different value between zero field cooling (ZFC) process and field cooling (FC) process [21]. The reduction of χ in ZFC below T_f indicates that there is an internal magnetic field whose direction is opposite to the external magnetic field. This fact was confirmed from the Mössbauer spectroscopy measurement in 1963 [22]. On the other hand, according to neutron scattering measurements [23], there is no spin order at a typical wave number. Furthermore, the result of ac magnetization measurement shows that a non-linear susceptibility of spin glass χ_2 diverges at T_f [24]. These experimental facts imply that the spin-glass state is a new magnetic ordering state and the spin-glass transition is a phase transition¹.

¹Whether the spin glass is really a phase transition or not is still controversial.

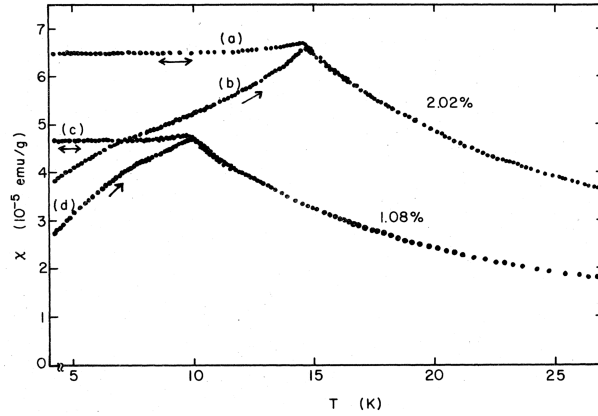


Figure 1.2: Magnetic susceptibility χ of $\text{Cu}_{100-x}\text{Mn}_x$ ($x=1$ and 2) alloys as a function of temperature [21]. A clear difference appears below T_f . χ decreases with decreasing temperature for the ZFC process, while it is constant for the FC process.

1.1.1 Randomness and frustration in spin glasses

In canonical spin glasses, the interaction between localized moments is mediated by conduction electron spins, which is referred to as the Ruderman-Kittel-Kasuya-Yosida (RKKY) interaction:

$$J_{ij} \propto \frac{\cos(2k_F \mathbf{r}_{ij})}{r^3} \quad (1.1)$$

where r is the distance between localized moments (i -th and j -th moments) and k_F is the Fermi wave number. Depending on r , the exchange coupling is either ferromagnetic ($J_{ij} > 0$) or antiferromagnetic ($J_{ij} < 0$). Due to the random distribution of localized moments in spin glasses, ferromagnetic and antiferromagnetic components coexist and thus the ground state is multiply degenerate (Fig. 1.3).

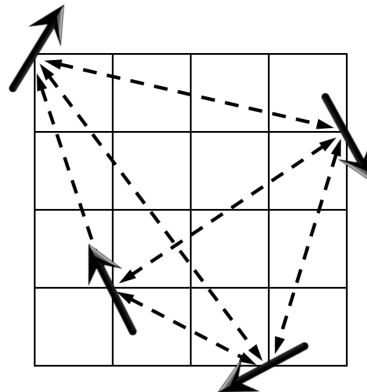


Figure 1.3: Schematic image of canonical spin glasses. The solid arrows indicate localized moments of magnetic impurities. The broken arrows indicate the RKKY interaction between localized moments.

1.1.2 Mean field theory of spin glasses

The mean field theory is a standard theory to explain ferromagnetism and antiferromagnetism in macro spin systems. In 1975, Edward and Anderson (EA) first adopted the mean field theory for the spin-glass transition [25]. By replacing site-randomness by randomness in the exchange coupling J , the Hamiltonian of spin glass can be written as

$$\mathcal{H}_{\text{EA}} = - \sum_{\langle i,j \rangle} J_{ij} S_i S_j - \sum_i h_i S_i \quad (1.2)$$

where J_{ij} is the interaction between the i -th and j -th spins, and h is an external field. J_{ij} is a random variable and its probability is expressed by

$$P(J_{ij}) = \left(\frac{z}{2\pi J^2} \right)^{1/2} \exp \left[-\frac{z}{2J^2} \left(J_{ij} - \frac{J_0}{z} \right)^2 \right]. \quad (1.3)$$

z is the number of J_{ij} acting on each spin. EA proposed that with decreasing temperature, thermal fluctuations of spins are additionally suppressed by the spin-spin interaction. The spins start to be randomly frozen just below a transition temperature. As a result, the spin-glass phase appears. In general, the order parameter of general magnetic system is magnetization ($m_q \equiv 1/N \sum_{t=1}^N \langle S_i \rangle e^{iq \cdot \mathbf{R}_i}$). However, the order parameter of spin glasses should not be the same as general magnetic systems because $m_q = 0$ at $T = 0$. To explain the spin-glass properties, EA used the following order parameters:

$$q_{\text{EA}} \equiv \lim_{t \rightarrow \infty} \frac{1}{N} \sum_{t=1}^N \langle S_i(0) S_i(t) \rangle \quad (1.4)$$

$$\bar{q} \equiv \lim_{N \rightarrow \infty} \frac{1}{N} \sum_{t=1}^N \langle S_i \rangle^2 \quad (1.5)$$

where q_{EA} is the order parameter of the ZFC process, and \bar{q} is that of the FC process.

The EA model includes random variables. Thus, it is not easy to calculate Eq. (1.2) directly. Sherrington and Kirkpatrick (SK) extended the EA model to an infinite range [26]. The SK Hamiltonian is written as:

$$\mathcal{H}_{\text{SK}} = - \sum_{i>j} J_{ij} S_i S_j - \sum_i h_i S_i. \quad (1.6)$$

There are roughly two methods for solving the SK model. The first one is a method using a mathematical trick called the replica method. The second one is a method evaluating a solution without using the replica method. In this subsection, we discuss these two methods in Ising spin glasses.

Replica spin method

In actual spin glasses, the magnetic impurity site is fixed and its probability distribution does not change with time. This fact indicates that experimentally obtained physical quantities originates from one probability distribution J_{ij} . Thus, it is necessary to specify each J_{ij} value concretely in order to compare the experimental physical quantities with thermodynamic quantities such as a magnetic susceptibility calculated from the SK Hamiltonian. However, the thermodynamic quantities depend not on details of the probability distribution, but on the averaged macroscopic quantities. In this case, we are able to compare the free energy obtained from experiments with that calculated from the SK Hamiltonian. However, the difficulty in treating random systems lies in calculating the averaged value after taking the logarithm. EA replaced a logarithmic component in the distribution function by the following factor:

$$\ln x = \lim_{n \rightarrow 0} \frac{1}{n} (x^n - 1). \quad (1.7)$$

When an external magnetic field is zero, the free energy and the distribution function of the SK model can be represented as

$$\beta F = -[\log(Z_J)]_J = -\lim_{n \rightarrow 0} \frac{1}{n} (|Z_J^n|_J - 1) \quad (1.8)$$

$$\begin{aligned} |Z_J^n|_J &= \left[\text{Tr}(S_i^a) \exp \left(\beta \sum_{a=1}^n \sum_{i,j} J_{ij} S_i^a S_j^a \right) \right]_J \\ &= \text{Tr}(S_i^a) \exp \left(\sum_{a,b=1}^n \sum_{\langle i,j \rangle} \frac{\beta^2 J^2}{2N} (S_i^a S_i^b) (S_j^a S_j^b) + \sum_{a=1}^n \sum_{\langle i,j \rangle} \frac{\beta J_0}{N} S_i^a S_j^a \right) \end{aligned} \quad (1.9)$$

where $\beta = 1/k_B T$, and $[\dots]_J$ is a sample averaging process. The key of this calculation is the sample averaging process on the second equation of Eq. (1.8). The first term of Eq. (1.9) expresses a replica-spin interaction characterized by J^2 . The second term represents an energy due to a ferromagnetic (or an antiferromagnetic) interaction and its value is proportional to an averaged value of distribution (J_0). Due to this mathematical technique, the virtual degree of freedom which is called ‘‘replica spin’’ as well as the interaction between replica spins are defined.

The free energy (f) for one spin obtained with the SK Hamiltonian is expressed as

$$f \equiv \lim_{N \rightarrow \infty} \frac{F}{N} = \lim_{n \rightarrow 0} \frac{1}{n} \min (f_n \{Q_{ab}, M_a\}) \quad (1.10)$$

$$\begin{aligned} \beta f_n \{Q_{ab}, M_a\} &= -\frac{\beta^2 J^2}{4} n + \frac{\beta J_0}{2} \sum_a M_a^2 + \frac{\beta^2 J^2}{2} \sum_{ab} Q_{ab}^2 \\ &\quad - \ln (\text{Tr}(S^a) \exp (\beta \mathcal{H}_{\text{eff}})) \end{aligned} \quad (1.11)$$

$$\mathcal{H}_{\text{eff}} = -\beta J^2 \sum_{ab} Q_{ab} S^a S^b + \sum_a (J_0 M_a + h) S^a. \quad (1.12)$$

Equation (1.12) is an effective Hamiltonian for n replica spins. The saddle point conditions of Eq. (1.10) can be obtained with the following self-consistent equations:

$$Q_{ab} = \langle S^a S^b \rangle_{\text{eff}}, \quad M_a = \langle S^a \rangle_{\text{eff}} \quad (1.13)$$

where $\langle \dots \rangle_{\text{eff}}$ is the thermal average in the effective Hamiltonian Eq. (1.12). By using the solution Q_{ab} , an order parameter \bar{q} and an uniform magnetization m can be written as follows:

$$\bar{q} = \lim_{n \rightarrow 0} \frac{2}{n(n-1)} \sum_{a,b} Q_{ab}, \quad m = \lim_{n \rightarrow 0} \frac{1}{n} \sum_a M_a. \quad (1.14)$$

Since the effective Hamiltonian Eq. (1.12) is symmetric with respect to an exchange of replica indices (a and b), the SK solution also has a replica symmetry as follows:

$$Q_{ab} = \bar{q} \equiv q_{\text{SK}}, \quad M_a = m. \quad (1.15)$$

The SK model clearly explained critical phenomena in spin glasses such as a spin-glass transition, divergence of nonlinear magnetic susceptibility, and the temperature dependence of the specific heat. However, it had a fatal defect that the entropy became negative at low temperatures. Parisi pointed out that the full description of the spin-glass order in the SK model needed an order-parameter function [27, 28] instead of a single order parameter. Parisi introduced Replica Symmetry Breaking (RSB) solution whose structure is shown in Fig. 1.4.

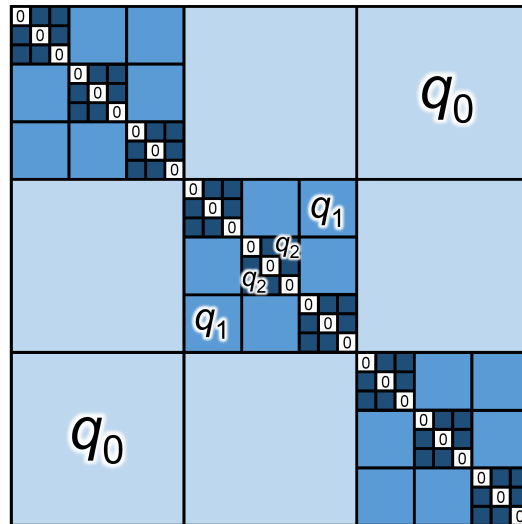


Figure 1.4: A Q_{ab} structure in Parisi solution.

Parisi proposed the following nested solution. The original $n \times n$ (n : integer > 1) matrix Q_{ab} is divided into $m_1 \times m_1$ ($n < m_1$) sub-matrices. Elements of sub-matrices at

the off-diagonal positions are all set as q_0 . Next, $m_1 \times m_1$ sub-matrices at the diagonal positions are further divided into $m_2 \times m_2$ ($m_2 < m_1$), where elements of subsub-matrices at the off-diagonal positions are all set as q_1 . By repeating this operation until the elements of the group become one replica ($Q_{aa} = 0$), the Parisi solution can be obtained. The Parisi solution satisfies the physical requirements for a correct solution, such as the stability in the spin-glass phase and magnetic phase diagrams. Therefore, the spin-glass phase has been considered as a thermodynamic phase to be described by an infinite number of order parameters for each “replica pair” ($a \neq b$). On the other hand, whether the replica method can describe all the magnetic properties in the real spin glasses is not a trivial issue.

Theoretical model without replica spin

To investigate the validity of the Parisi solution, it is necessary to compare the replica spin with the spin in real space. Thouless, Anderson and Palmer (TAP) developed a method to find the solution in the real spin space without introducing replica spins in 1977 [29]. In the TAP method, the first step is to examine the thermodynamic behavior of the spins in each sample determined by one set of J_{ij} , and then to treat the statistical process. The argument by TAP is based on an equation that determines the thermal mean value m_i of each magnetization in one sample,

$$m_i = \tanh \beta \left[h_i + \sum_j J_{ij} m_j - \beta m_i \sum_j J_{ij}^2 (1 - m_j)^2 \right]. \quad (1.16)$$

The TAP free energy is then given by the following equation:

$$F_{\text{TAP}}\{m_i\} = \frac{1}{2\beta} \sum_i \left[(1 + m_i) \ln \left(\frac{1 + m_i}{2} \right) + (1 - m_i) \ln \left(\frac{1 - m_i}{2} \right) \right] \\ - \sum_{\langle ij \rangle} J_{ij} m_i m_j - \frac{\beta}{2} \sum_{\langle ij \rangle} J_{ij}^2 (1 - m_i^2)(1 - m_j^2) - \sum_i h_i m_i. \quad (1.17)$$

The second term on the right hand corresponds to the ordinary mean-field term, and the third term is called Onsager’s half jump field which is the additional magnetization produced by m_i to the ordinary mean-field. One can directly calculate the freezing direction of spins because m_i obtained from the equation represents the thermal equilibrium state. Although it is not easy to solve this equation, it is possible to evaluate the number of solutions analytically. An important message obtained from the TAP solution is that the solution m_i is a multiple solution. This fact means that there are a large number of thermodynamic states separated by energy barriers as shown in Fig. 1.5.

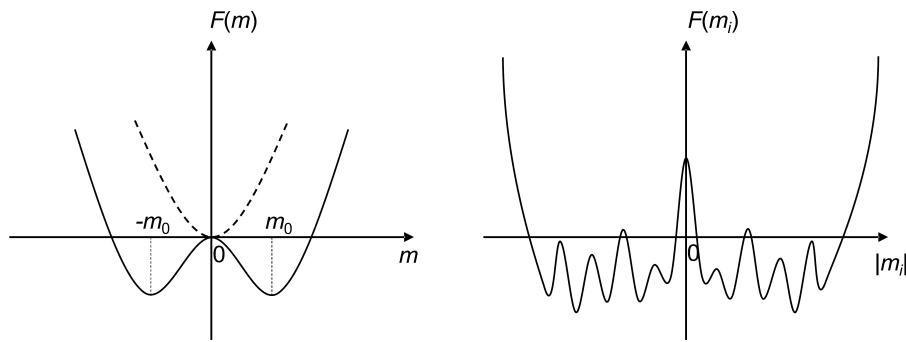


Figure 1.5: Free energy of ferromagnets (left) and spin glasses (right). In ferromagnets, there are only two pure states $\pm m$ connected by the Hamiltonian's trivial symmetry.

The spin glass phase described by the TAP solution can only exist in one region with a many-valley structure of free energy and a finely divided phase space. This means non-ergodic and indicates a completely new type of phase transition, that is, the transition from the high temperature ergodic phase to the low temperature non-ergodic phase. By combining this TAP solution with the Parisi solution, replica spins can be associated with real space spins, and thus the mean field theory of spin glasses is completed.

1.2 Determination of T_f

In this section, we review how to determine T_f from an experimental point of view. Especially, this issue is closely related to one of the motivations of the present work *i.e.*, how to evaluate T_f for a spin-glass nanowire.

T_f is one of the important factors to characterize the spin-glass system. In the mean field theory of spin glasses, this temperature corresponds to the energy scale of the depth of many-valleys structure.

Experimentally, T_f is usually determined by magnetization measurements. In case of *dc* magnetization measurements, T_f is defined as the temperature at which a *dc* magnetization starts to take a different value between the FC and ZFC processes. On the other hand, in case of *ac* magnetization measurements, T_f is defined as the cusp temperature because such a difference does not appear. However, because of the intrinsic nature of spin glasses, T_f is not uniquely determined even by those magnetization measurements. For example, in case of *dc* magnetization measurements, to obtain the clear signal, an initially applied magnetic field should be large. However, with increasing this initial magnetic field, it is known that the cusp structure becomes broader. Especially, in a strong anisotropic system such as AuMn, T_f shifts to a lower temperature side with increasing the applying initial magnetic field [30]. Even in *ac* magnetization measurements, such a broadening effect is also observed. When a high frequency magnetic field is applied, localized moments of spin glasses cannot follow the vibration of magnetic field due to the slow dynamics of spin glasses. As a result, the observed T_f becomes higher than the actual T_f . These features can be observed not only in spin glasses but also in a super-paramagnet which has localized magnetic clusters. Therefore, it has been argued whether spin-glass is a phase transition or not since 1980s.

To estimate the accurate spin-glass temperature, a non-linear susceptibility measurement is usually performed. The nonlinear susceptibility χ_n exhibits a clearer divergent behavior at T_f . One of the evidences that the spin-glass transition is a phase transition is a divergence of the nonlinear susceptibility at T_f . The linear and the nonlinear susceptibilities χ_0 and χ_2 are defined by the following relation,

$$\frac{M}{H} = \chi_0 + \chi_2 H^2 + \chi_4 H^4 + \dots, \quad (1.18)$$

where M is the magnetization and H is the applied magnetic field. Figure 1.6 is the demonstration of a nonlinear susceptibility measurement of spin-glass $\text{Au}_{98.5}\text{Fe}_{1.5}$ [24]. A clear singular divergence in χ_2 was observed at the temperature where χ_0 has a cusp.

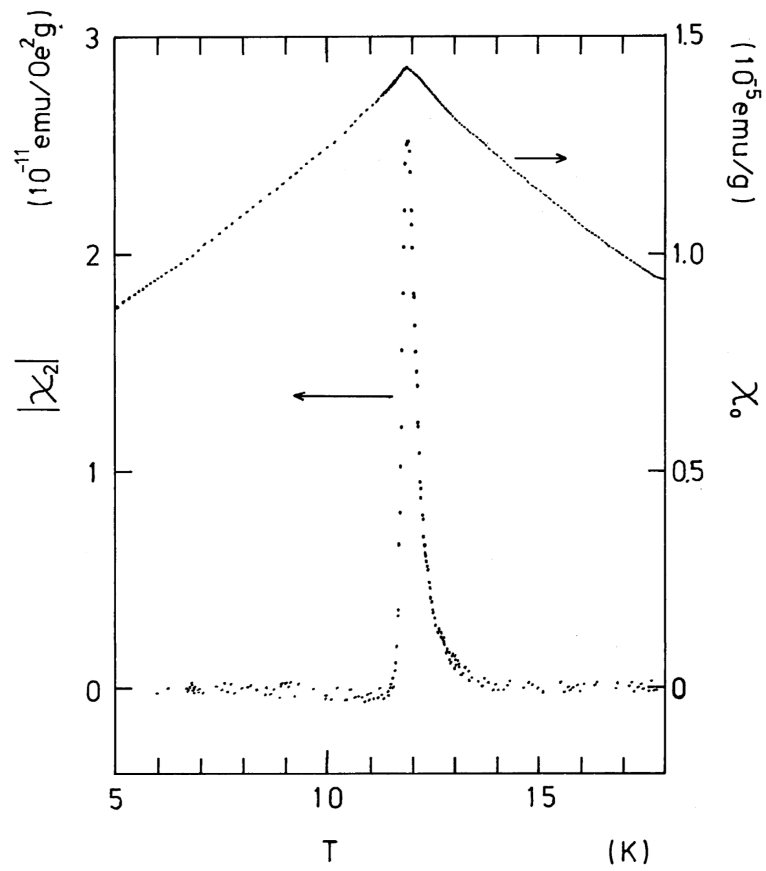


Figure 1.6: Linear susceptibility χ_0 and nonlinear susceptibility χ_2 measurements of $\text{Au}_{98.5}\text{Fe}_{1.5}$. Reproduced with permission from Ref. [24]. ©(1983) The Physical Society of Japan.

A dynamical magnetization measurement is also an effective method to determine T_f . By investigating T_f as a function of the frequency of magnetic field, the slow dynamics of spin glasses can be suppressed. In fact, such a frequency (ν) dependence has been studied in a variety of spin-glass materials. Hence, it is not a trivial matter to determine whether the experimentally observed “spin-glass transition” is really a thermodynamic second-order transition persisting in the $\nu \rightarrow 0$ limit.

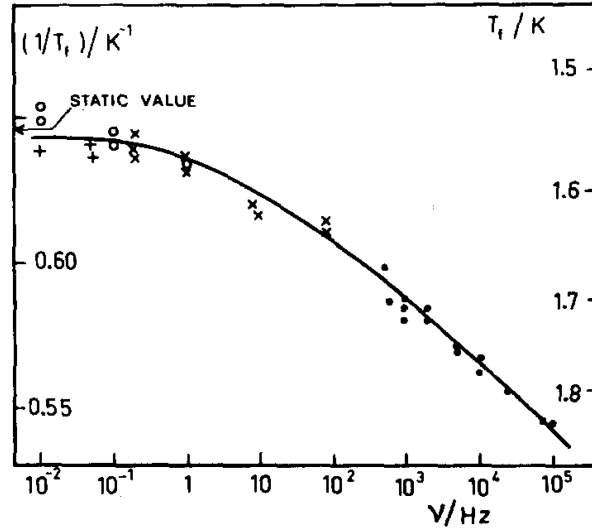


Figure 1.7: The frequency ν dependence of the $1/T_f$. Reproduced from Ref. [31], with the permission of AIP Publishing.

Ferré *et al.* tried such an extrapolation by performing the *ac* susceptibility measurement on nonmetallic spin glasses $\text{Eu}_{40}\text{Sr}_{60}\text{S}$ [31]. Figure 1.7 shows the frequency ν dependence of the inverse cusp temperature $1/T_f$. This is a clear experimental method to determine of *equilibrium* spin-glass temperature.

The cusp anomaly is also observed in specific heat measurements [32]. In canonical spin glasses, however, it is difficult to estimate a magnetic specific heat quantitatively because specific heat capacities of electrons and lattices in a host noble metal are larger than those of magnetic impurities.

Neutron scattering, NMR and μSR measurements have been performed to investigate local spin dynamics in spin glasses. However, these methods are not so suitable to determine T_f by the following reasons. (1) These techniques involve intrinsic measurement time constants. When the relaxation of localized moments is slower than these time constants, it is indistinguishable from a real static contribution.² (2) Spin glasses are easy to have local magnetic clusters and thus short-range-order effects occur in these alloys. However, we emphasize that these methods are invaluable tools to investigate a magnetic ordering state above T_f and below T_f .

²The relaxation times of neutrons and muons are $\sim 10^{-9}$ s and 10^{-6} s, respectively. The Mössbauer spectroscopy can be used only if the relaxation time is within $\sim 10^{-7}$.

1.3 Electrical conductivity in spin glasses

Canonical spin glasses have an electrical conductivity because those are based on noble metals. Some groups investigated the effect of magnetic impurities on electrical conductivity and the “impurity resistivity” ($\Delta\rho(T) \equiv \rho_{\text{alloy}}(T) - \rho_{\text{purehost}}(T)$) varies roughly linearly with temperature near T_f and has a broad maximum at a temperature much higher than T_f [3]. Campbell *et al.* showed that $\Delta\rho(T)$ of four canonical spin glasses follows a $T^{3/2}$ law at low temperatures, a T -linear law near T_f , and a slower temperature variation above T_f [33]. The initial $T^{3/2}$ dependence is well-explained by the theory reported by River and Adkins based on an elementary excitation in spin glasses [34]. However, their interpretation includes many assumptions in the theory of spin glasses. Campbell *et al.* calculated $\Delta\rho(T)$ based on the numerical simulation of specific heat performed by Walker and Walstedt [35–37] and compared with experimental data [33]. They obtained a good agreement between the resistivity data and a model using the Walker-Walstedt excitation description. They derived a local spin-relaxation rate from the resistivity data, which is consistent with that estimated with other techniques.

Taniguchi *et al.* measured the Hall effect and magnetization in AuFe simultaneously, and showed that a cusp appeared both in the Hall effect and in the magnetization [38].

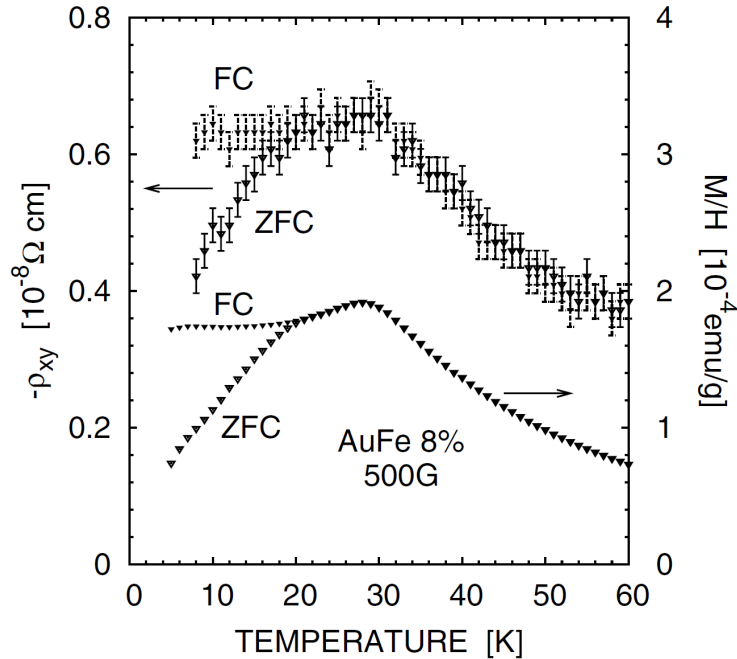


Figure 1.8: The simultaneous measurements of the Hall effect and the magnetization [38].

The similar results were reported by Fabris *et al.* [39]. These experimental facts indicate that electrical conductivity measurements can be a useful probe to detect the information of spin-glass transition.

With the recent development of microfabrication technology, it has become possible to investigate submicrometer-size spin-glass samples where a characteristic length scale such as the distance between two magnetic impurities is comparable.

Weissman *et al.* fabricated CuMn mesoscopic devices and measured the $1/f$ noise of electrical resistance [40]. They discovered that the $1/f$ noise of CuMn increases rapidly at T_f as shown in Fig. 1.9.

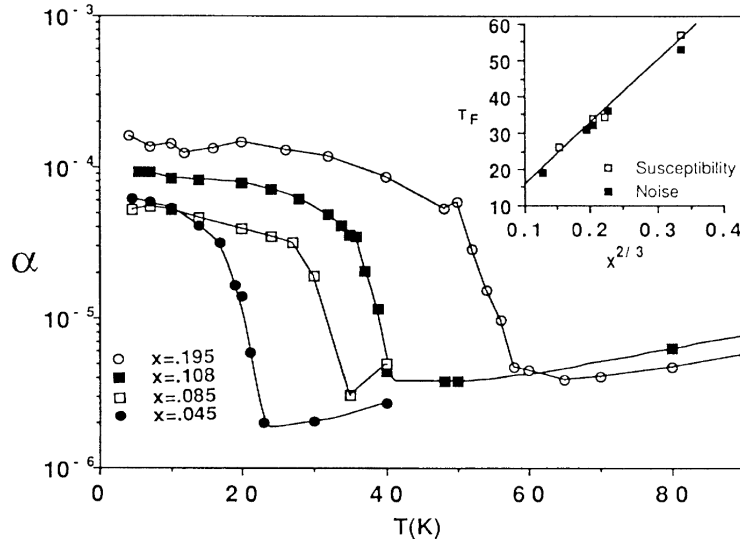


Figure 1.9: The first report of the $1/f$ measurement in spin glasses [40]. The vertical axis corresponds to a normalized $1/f$ noise magnitude. The inset shows the relation between T_f estimated by the noise measurements and T_f by the magnetization measurements.

The vertical axis α in Fig. 1.9 is a Hoge parameter that expresses the amplitude of a spectral density. This noise originates from thermal fluctuations of Mn spins, reflecting the transition between valleys of the free energy multi-valley structure in the mean field theory. It is important to be able to directly detect the microscopic picture of spin glasses by reducing the device size.

In 2013, Capron *et al.* reported universal conductance fluctuations (UCFs) in AgMn nanowire (Fig. 1.10(a)) [41]. They investigated the quantum coherence in the AgMn nanowire near T_f .

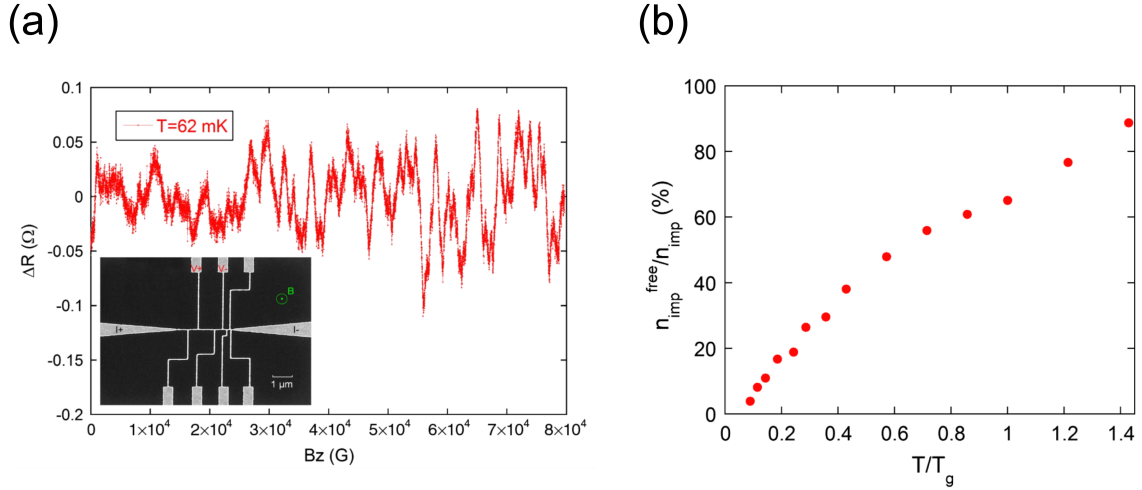


Figure 1.10: The quantum coherence measurements reported by Capron *et al.* [41]. (a) A typical result of UCFs. The inset is the SEM image of the device. (b) The temperature dependence of the fraction of free spins.

With decreasing temperature, the fraction of free spins monotonically decreases. Surprisingly, however, the reduction of the number of free spins continues even below T_f . This result indicates that spin fluctuations certainly exist even below T_f and it is not intuitively consistent with a conventional mean field theory of spin glasses. We also note that T_f of these experiments is determined by the film of AgMn, which could be different from that of the nanowire.

As mentioned above, recent electrical conductivity measurements in nanoscale spin glasses can directly detect the microscopic picture of spin glasses experimentally. This fact indicates that the electrical measurement in nanoscale spin glasses would be a strong method to elucidate the spin-glass dynamics.

Chapter 2

Triangular antiferromagnet

In this chapter, we briefly review another frustrated magnetic system, *i.e.*, triangular antiferromagnet, and detail our target material Ag_2CrO_2 .

2.1 Frustration on triangular antiferromagnet

Triangular antiferromagnet is one of the prototypes for studying the magnetic frustration effect in materials. We consider a two-dimensional (2D) lattice in which classical spins are arranged in an equilateral triangular lattice (Fig. 2.1(a)). When the antiferromagnetic interaction works between the two adjacent Ising spins, the opposite spin directions should be realized as the lowest energy state. However, the direction of the third spin is not uniquely determined because the spin configuration does not satisfy all antiferromagnetic interactions.

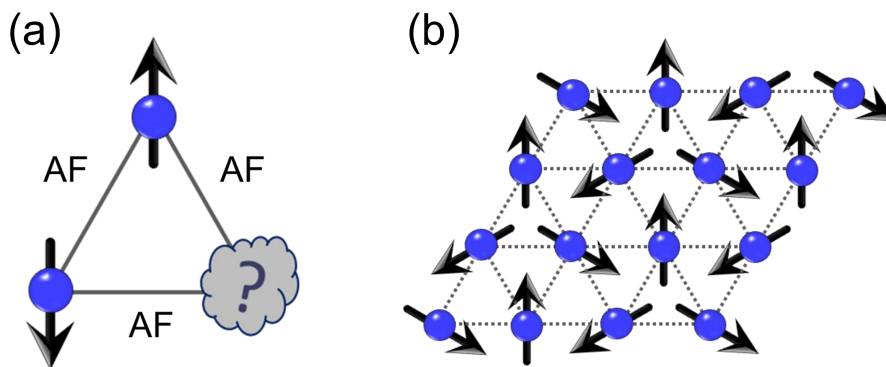


Figure 2.1: Schematic images of (a) geometrical frustrations in the Ising triangular antiferromagnet, and (b) the 120° spin structure.

Triangular antiferromagnets have been studied for a long time as a prototype of frustrated spin systems. Although it is the simple model, unique thermodynamic states appear depending on the symmetry of the spins. For example, in the Ising antiferromagnetic spin system, there is no long-range order even in the ground state and its

residual entropy is 49 % out of the total entropy of the system [42]. But when there is a small anisotropy in a crystal symmetry, the spin configuration becomes non-collinear due to competition between the small anisotropy and the frustration [43, 44]. In a triangular lattice with continuous degrees of freedom such as the XY model and Heisenberg model, the ground state is the 120° spin structure as shown in Fig. 2.1(b).

However, the triangular lattice has another degree of freedom, *i.e.*, vector spin chirality (Fig. 2.2(a)). It is known that this can induce a topological phase transition. The spiral spin structure is not able to be deformed continuously from an uniform antiferromagnetic spin structure (Fig. 2.2(b)). Therefore, it can be regarded as a topological defect in the antiferromagnetic state, and vortices with opposite directions can be considered as defects with topological charges. This topological phase transition is called the Berezinskii-Kosterlitz-Thouless (BKT) transition [45–47] which occurs at a finite temperature even in the 2D spin system. In a Heisenberg spin system, since the spin can rotate freely in the three-dimensional space, the chirality vector also has continuous degrees of freedom. Therefore, no phase transition should appear in the XY model. However, it is theoretically predicted that the topological transition related to the generation of the vortex of chirality vector (Z_2 vortex) similar to the BKT transition appears at a finite temperature, and it has been confirmed by numerical calculations [48]. Nevertheless, such thermodynamic states and a phase transition have never been observed in real materials.

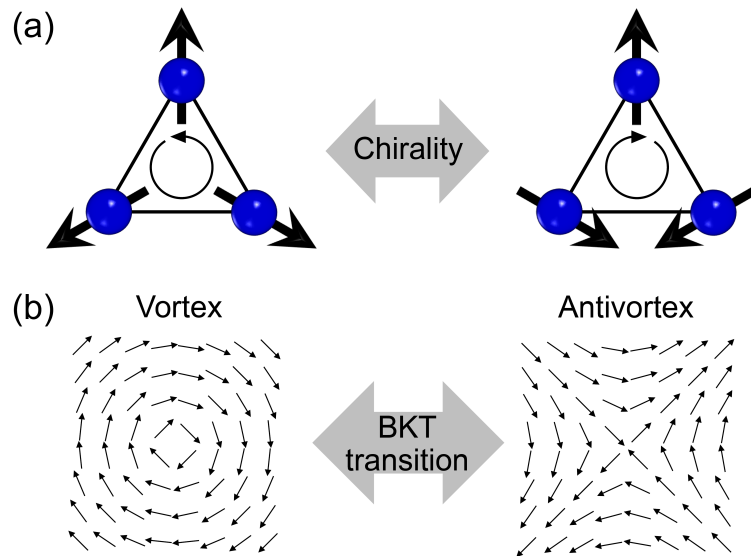


Figure 2.2: Schematic images of (a) the chirality originated from the spin configuration and (b) the BKT transition.

2.2 Ising triangular antiferromagnet

Here, we focus on the Ising triangular antiferromagnetic model because our experiment is related to the Ising triangular antiferromagnet. There are so many Ising triangular model materials such as hexagonal ABX_3 type compounds. Therefore, there have been actively studied both from the theoretical and experimental aspects. As a theoretical study of this triangular lattice Ising spin model, we introduce the simulation by molecular field approximation by Mekata [43]. Mekata considered the triangular Ising model with the antiferromagnetic nearest neighbor interaction J (< 0) and the antiferromagnetic next-nearest neighbor interaction J' (> 0). In this case, the triangular lattice is divided into three sublattices as shown in Fig. 2.3(a).

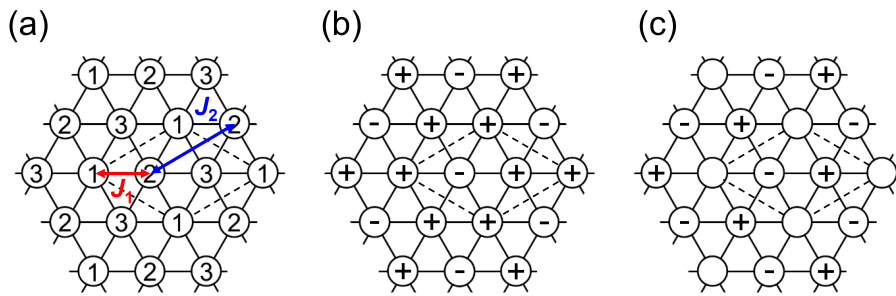


Figure 2.3: Schematic images of (a) the sublattice in the 2D triangular Ising lattice, (b) the ferrimagnetic structure and (c) the partially disordered antiferromagnetic structure. Broken lines indicate a magnetic unit cell. The red arrow and blue arrow indicate the nearest neighbor interaction and the second nearest neighbor interaction, respectively.

The Hamiltonian for the l -th sublattice can be written as:

$$\mathcal{H} = -6J(\langle S_m \rangle + \langle S_n \rangle) \sum_i S_l^i - 12J' \langle S_l \rangle \sum_i S_l^i - g\mu_B H \sum_i S_l^i \quad (2.1)$$

where the subscripts l , m , and n are used to specify the sublattices and i is the number of unit cell. By substituting S_l by $S\sigma_l$, the relative magnetization $\langle \sigma_l \rangle$ can be obtained in the following equation:

$$\langle \sigma_l \rangle = \tanh \{ \beta (\alpha \langle \sigma_l \rangle + \langle \sigma_m \rangle + \langle \sigma_n \rangle + \gamma) \} \quad (2.2)$$

where $\alpha = 2J'/J$, $\beta = 6S^2J/kT$ and $\gamma = g\mu_B H/6SJ$ (g : g-factor, μ_B : Bohr magnetron). Equation (2.2) can be solved numerically as a function of α , β , and γ . He discovered two magnetic transition temperatures when $0.8 > |J'/J| > 0$. The lowest energy state is the ferrimagnetic state as shown in Fig. 2.3(b). On the other hand, an antiferromagnetic state in which one of the three sublattices is completely disordered appears at the middle temperature region (Fig. 2.3(c)). This state is called ‘‘Partially Disordered (PD) state’’.

In 1995, Takagi and Mekata considered the two-dimensional Ising model with the third neighbor interaction in addition to Eq. (2.1) in the 2D Ising model (Fig. 2.4) [49].

The Hamiltonian can be written as:

$$\mathcal{H} = -J_1 \sum_{1\text{st } n} \sigma_i \sigma_j - J_2 \sum_{2\text{nd } n} \sigma_i \sigma_j - J_3 \sum_{3\text{rd } n} \sigma_i \sigma_j \quad (2.3)$$

where σ_i is ± 1 and J_1 , J_2 and J_3 are the 1st, the 2nd and the 3rd neighbor interaction parameters, respectively.

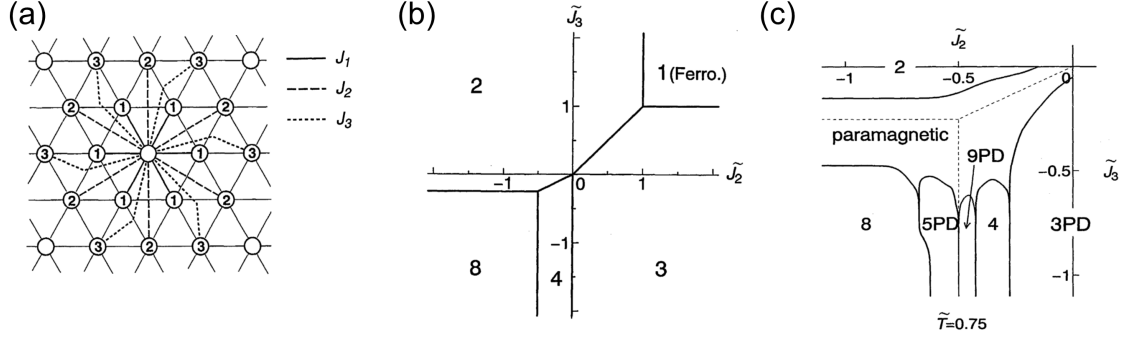


Figure 2.4: Numerical calculations performed by Takagi and Mekata reproduced with permission from Ref. [49]. ©(1995) The Physical Society of Japan. (a) Schematic image of 1st, 2nd and 3rd neighbor interactions, J_1 , J_2 and J_3 in the triangular Ising lattice. The solid lines, broken lines and bent dotted lines indicate J_1 , J_2 and J_3 interaction bonds for the quoted sites, respectively. (b) Phase diagram of the ground state. Each phase is labeled by the sublattice number n . (c) Phase diagram at $\tilde{T} = 0.75$. Each phase is labeled by the sublattice number n .

To evaluate Eq. (2.3), J_2 , J_3 and the temperature are normalized with $|J_1|$ as follows:

$$\tilde{J}_2 = \frac{J_2}{|J_1|}, \quad \tilde{J}_3 = \frac{J_3}{|J_1|} \quad \text{and} \quad \tilde{T} = \frac{k_B T}{|J_1|}. \quad (2.4)$$

Figure 2.4(b) shows the phase diagram of the ground state ($\tilde{T} = 0$) obtained with the Monte Carlo simulation. When \tilde{J}_2 and \tilde{J}_3 are larger than 1, the ferromagnetic state is the ground state. On the other hand, the PD states with 2-, 3-, 4- and 8- sublattices can be the lowest energy states when \tilde{J}_2 and \tilde{J}_3 are smaller than 1. Figure 2.4(c) shows the phase diagram when \tilde{J}_2 , the \tilde{J}_3 are negative and $\tilde{T} = 0.75$. The three PD phases with 4-, 5- and 9- sublattices are located in between the more stable 3PD and 8PD states. Therefore, the magnetic structure of the system depends on the type and magnitude of the effective neighbor interaction and the temperature range.

Experimentally, some candidate materials with the PD state has been reported in quasi-1D Ising chains which can be considered to have the same magnetic properties as the 2D triangular lattice, for example, $A\text{CoX}_3$ compounds ($A = \text{Cs}, \text{Rb}, X = \text{Cl}, \text{Br}$) [50], the multiferroic material (CuFeO_2) [51–53], alloys (SmPt_2Si_2 and GdInCu_4) [54,55], and strong correlation f -electron systems (CeSb and UNi_4Be) [56,57]. The PD phase realized in the above materials has been confirmed by directly evaluating the magnetic structure using neutron scattering, or by detecting the local magnetization using NMR, μSR , and Mössbauer spectroscopy measurements.

2.3 Basic properties of Ag_2CrO_2

In this section, we explain basic properties of Ag_2CrO_2 , which is a triangular Ising antiferromagnetic system with electrical conductivity and also studied in the present thesis as we detail later on.

2.3.1 Crystal structure

The polycrystalline Ag_2CrO_2 sample was firstly fabricated by Yoshida *et al.* in 2011 [14]. It was obtained by encapsulating a mixture of Ag, Ag_2O , and Cr_2O_3 powders in a gold cell, and by baking them at 1200 °C for 1 hour under a pressure of 6 GPa. The crystal structure is shown in Fig. 2.5. The CrO_2 triangular antiferromagnetic layer and the Ag_2 conductive layer are alternatively stacked. Since Cr^{3+} (t_{2g}^3) has the high-spin electron configuration, no orbital degrees of freedom exist and the regular triangular lattice is expected. According to the X-ray diffraction [14] and the neutron powder diffraction [15], Ag_2CrO_2 has a trigonal structure ($P\bar{3}m1$) with $a = 2.9298 \text{ \AA}$ and $c = 8.6637 \text{ \AA}$ at 200 K (Fig. 2.5(b)) and a monoclinic structure ($C2/m$) at low temperatures (Fig. 2.5(c)).

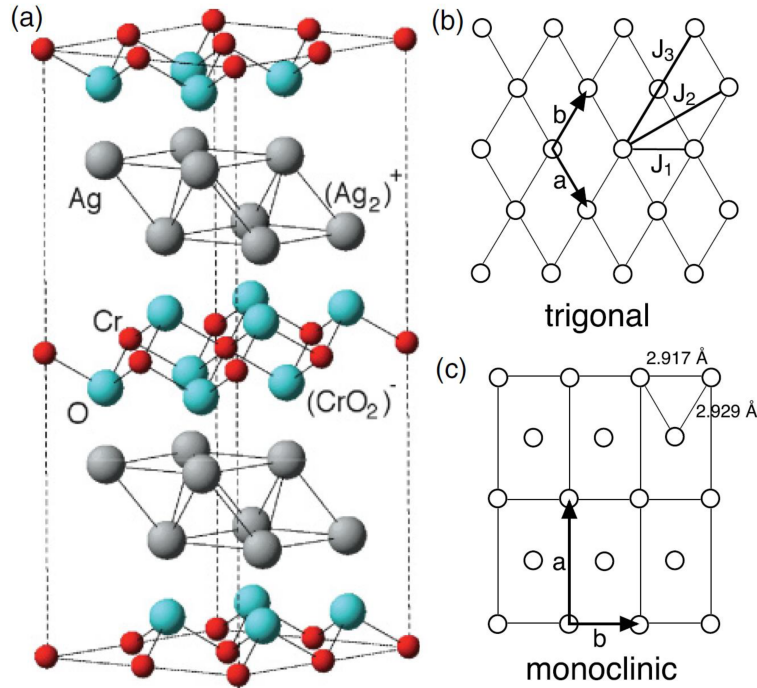


Figure 2.5: The crystal structure of Ag_2CrO_2 [15]. (a) $2 \times 2 \times 2$ unit cell of the trigonal phase above T_N . (b), (c) Schematic structures of the triangular Cr^{3+} spin lattice (b) at $T > T_N$ (trigonal phase) and (c) at $T < T_N$ (monoclinic phase). The magnetic interactions J_1 , J_2 and J_3 are shown in (b).

2.3.2 Magnetization measurement

Figure 2.6(a) shows the magnetization measurement of Ag_2CrO_2 powder [14]. The susceptibility (M/H) obeys the Curie-Weiss law at high temperatures. The inset of Fig. 2.6(a) shows the line fitting to the χ^{-1} data between 200 and 350 K, from which the effective moment p_{eff} and the Weiss temperature θ_{W} are estimated to be 3.55 and $\theta_{\text{W}} = -97$ K, respectively. This p_{eff} value is close to the high-spin state of Cr^{3+} , $S = 3/2$ ($p_{\text{eff}} = 3.87$). On the other hand, at low temperatures, the magnetic susceptibility abruptly increases at $T_{\text{N}} = 24$ K and exhibits a small temperature hysteresis between the ZFC and FC data below T_{N} (Fig. 2.6(a)). Figure 2.6(b) shows the M - H curves of Ag_2CrO_2 at 2 K ($< T_{\text{N}}$) and 50 K ($> T_{\text{N}}$). In contrast with the linear magnetization at 50 K, the data at 2 K show a clear hysteresis loop with a spontaneous magnetization whose value is 8.5% out of the full magnetic moment. Even at 7 T, the magnetization is approximately only 12% of $3\mu_{\text{B}}$. These results indicate that the ground state of Ag_2CrO_2 has an antiferromagnetic order with weak ferromagnetic moments.

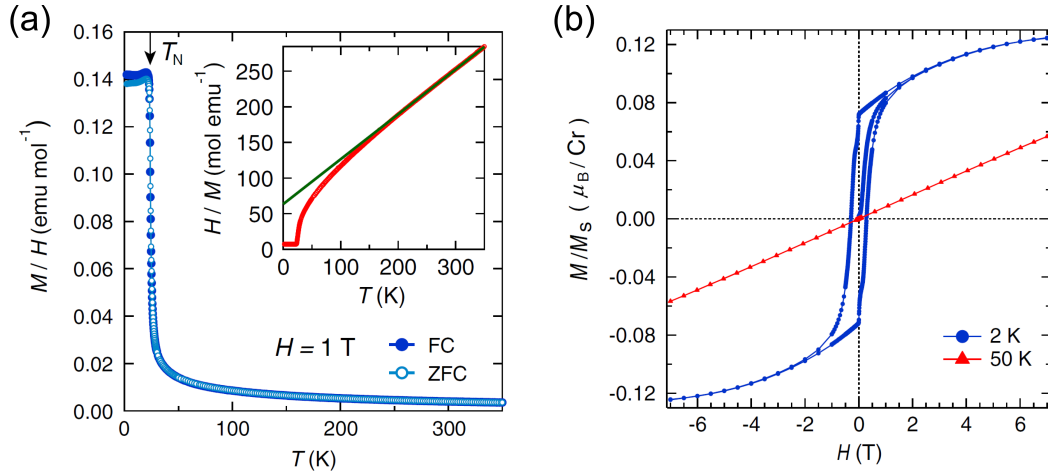


Figure 2.6: The magnetic susceptibility of Ag_2CrO_2 [14]. Reproduced with permission from Ref. [14]. ©(2011) The Physical Society of Japan. (a) Temperature dependence of the magnetic susceptibility. The solid and open circles correspond to FC with $H = 1$ T and ZFC data, respectively. The inset shows the inverse magnetic susceptibility and the solid line indicates the Curie-Weiss fitting. (b) Magnetization divided by full-saturation moment $3\mu_{\text{B}}$ versus H curves at $T = 2$ and 50 K.

2.3.3 Specific heat measurement

The specific heat has a sharp peak at $T = 24$ K as shown in Fig. 2.7. This peak temperature corresponds to the magnetic transition temperature and this temperature was determined as T_N . The inset of Fig. 2.7 shows the relation between C/T and T^2 . Below 10 K, the specific heat obeys the conventional specific-heat formula: $C/T = \gamma + \beta T^2$, where γ is the Sommerfeld constant and β is the lattice specific-heat constant. The γ value of Ag_2CrO_2 ($9.74 \text{ mJ mol}^{-1} \text{K}^{-2}$) is relatively large and this value is consistent with the γ of the other Ag_2MO_2 ($M = \text{Mn}, \text{Ni}$) [58,59]. The large γ indicates the large effective mass of conduction electrons. Such a large effective mass in Ag_2CrO_2 would originate from the strong hybridization of the Ag $5s$ and the Cr $3d$ orbital bands at the Fermi level.

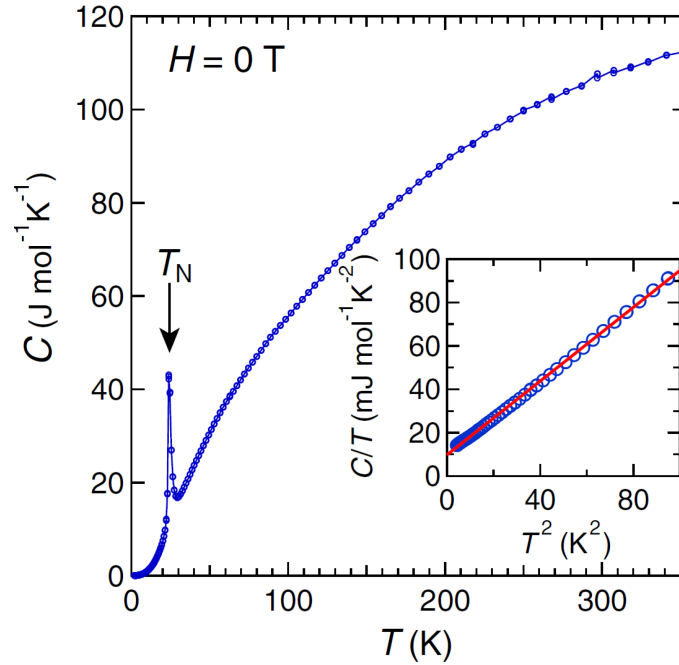


Figure 2.7: The specific-heat measurement of Ag_2CrO_2 [14]. Reproduced with permission from Ref. [14]. ©(2011) The Physical Society of Japan. The sharp peak appears at T_N . The inset shows C/T as a function of T^2 . The red line indicates the fitting result with the conventional specific-heat formula.

2.3.4 Electrical conductivity

Figure 2.8 shows the resistivity of Ag_2CrO_2 as a function of temperature under $H = 0$ and 9 T [14]. It has a metallic conductivity due to the itinerant electrons in the quarter-filled Ag 5s band. The most interesting characteristic of Ag_2CrO_2 is the large resistivity reduction at T_N . This reduction corresponds to approximately 60 % of the resistivity just above T_N . The similar reduction has been observed in Ag_2MO_2 ($M=\text{Mn}, \text{Ni}$) [58, 59], but the reduction in Ag_2CrO_2 is much larger than other Ag_2MO_2 . These facts indicate that the antiferromagnetic CrO_2 layer and the conductive Ag₂ layer are strongly coupled.

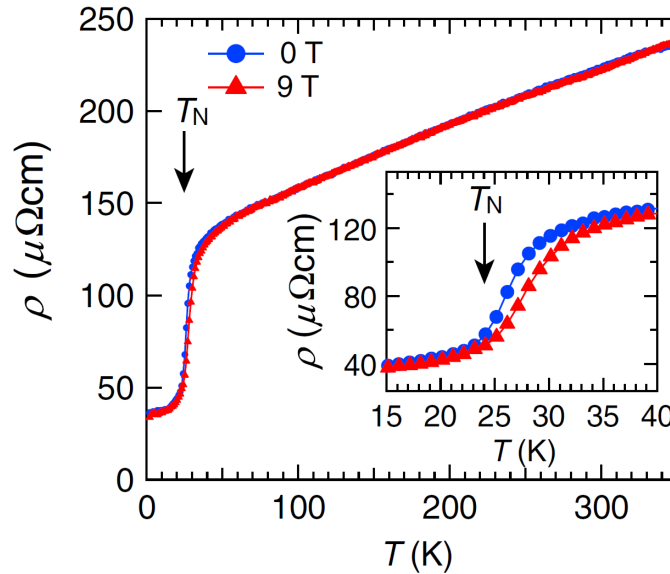


Figure 2.8: The temperature dependence of the resistivity in Ag_2CrO_2 under $H = 0$ T (circles) and 9 T (triangles) [14]. The arrow indicates T_N determined from the specific-heat measurement under $H = 0$ T. The inset shows a closeup of the resistivity near T_N . Reproduced with permission from Ref. [14]. ©(2011) The Physical Society of Japan.

In 2015, Kida *et al.* measured the electrical conductivity of polycrystalline Ag_2CrO_2 [60]. Figure 2.9 shows the magnetoresistance (MR: $(\rho(H) - \rho(0))/\rho(0)$) of Ag_2CrO_2 at several temperatures. Below T_N , the MR curves are positive and almost linear with respect to the magnetic field. With increasing temperature, the MR changes the sign at around T_N and becomes smaller above T_N .

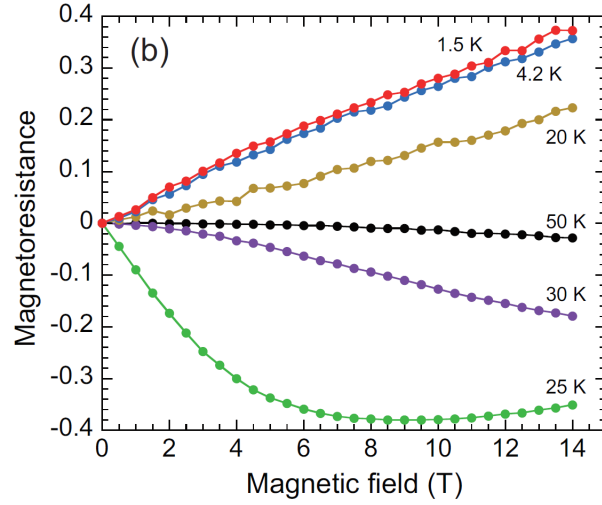


Figure 2.9: MR of polycrystalline Ag_2CrO_2 at several different temperatures [60].

Figure 2.10(a) shows the Hall resistivity $\rho_H(H)$ curves of Ag_2CrO_2 at several temperatures. $\rho_H(H)$ has a nonlinear behavior with H , and its magnitude increases with increasing temperature. When the total Hall resistivity can be expressed as $\rho_H = R_0\mu_0H + R_sM$ (R_0 : ordinary Hall coefficient, μ_0 : vacuum permeability, R_s : anomalous Hall coefficient and M : magnetization), the relation between $\rho_H(H)$ and $M(H)$ is shown in Fig. 2.10(b) by assuming that R_0 is very small due to the large carrier concentration. Above T_N , ρ_H follows the conventional anomalous Hall effect ($T = 30, 50$ K). In contrast, ρ_H deviates from the linear law below T_N ($T = 20, 25$ K). From these results, the unconventional magnetotransport may originate from the spin fluctuations related to the spin structure of Ag_2CrO_2 .

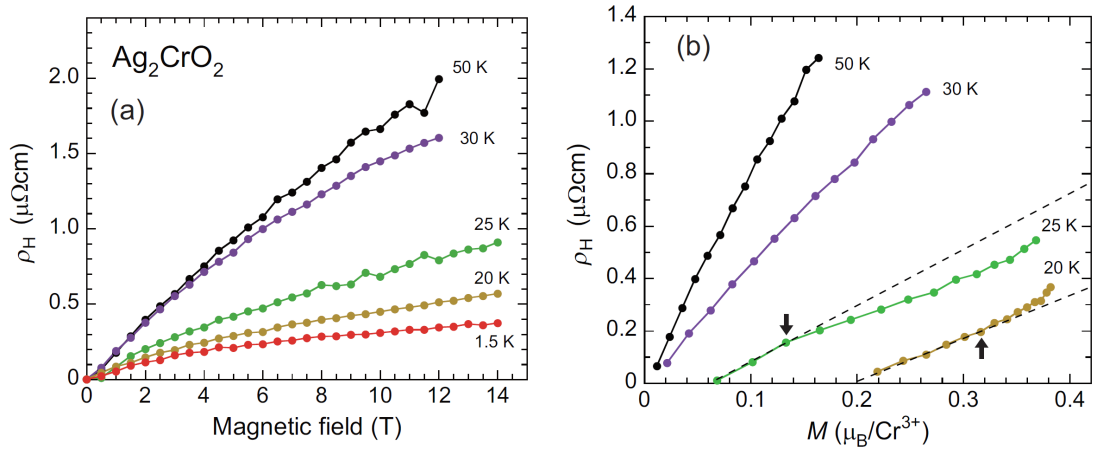


Figure 2.10: The Hall measurement in polycrystalline Ag_2CrO_2 [60]. (a) Hall resistivity as a function of magnetic field at several temperatures. (b) ρ_H vs M curves at several temperatures. The arrows indicate the point where the Hall resistivity deviates from the linearity.

2.3.5 Neutron scattering measurement

The magnetic Bragg reflections obtained with the neutron scattering experiment [15] are shown in Fig. 2.11(a).

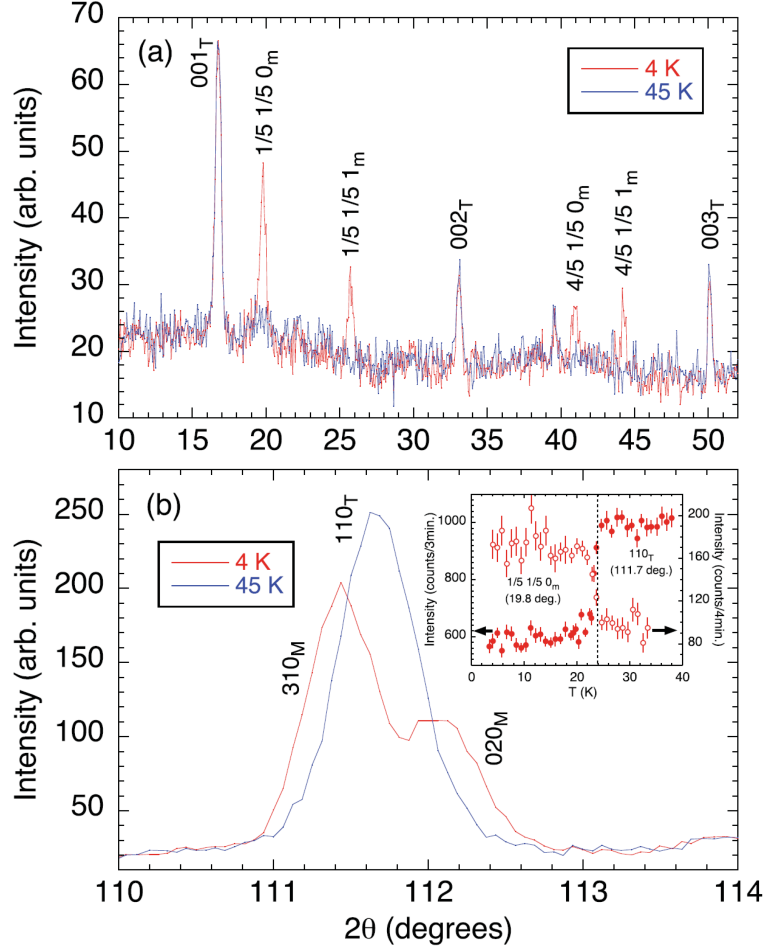


Figure 2.11: Neutron powder diffraction patterns in Ag_2CrO_2 at 4 and 45 K [15]. The data at low scattering angles show that some magnetic Bragg peaks develop below T_N (a), and those at high scattering angles show that a nuclear Bragg peak splits below T_N (b). The inset shows the temperature dependence of the magnetic intensity at 19.8° and nuclear intensity at 117.9° measured with increasing temperature.

The magnetic reflections with $\frac{1}{5} \frac{1}{5} L$ ($L = 0$) and $\frac{4}{5} \frac{1}{5} L$ ($L = 1$), were observed. This fact indicates that the magnetic structure has a 5 sublattice structure in the triangular plane, and the unit cell along the c -axis is the same as the chemical unit. Thus, Cr^{3+} has an Ising anisotropy along the c -axis. The inset of Fig. 2.11(b) shows the temperature dependence of the reflection intensity. The open and closed circles show the magnetic and nuclear intensity, respectively. The magnetic intensity abruptly increases below T_N , whereas the nuclear intensity drops at T_N . It indicates that the magnetic and structural phase transitions occur simultaneously at T_N . From the neutron scattering

results, as the stable state of Ag_2CrO_2 at finite temperature, a partially disordered magnetic structure with 5 sublattices can be assumed (Fig. 2.12).

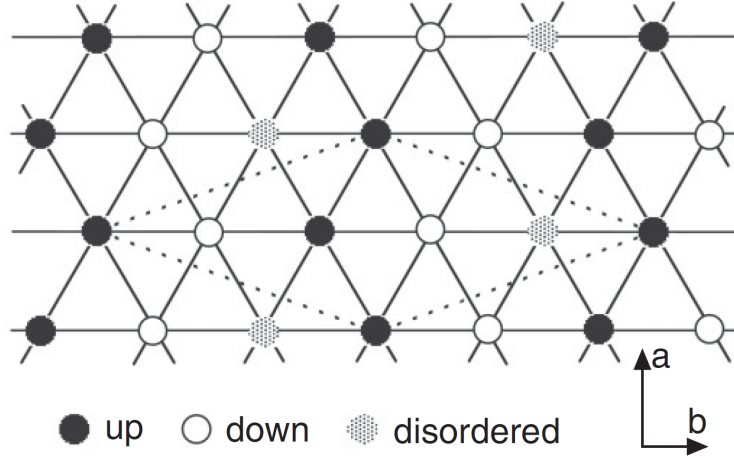


Figure 2.12: Schematic spin structure of the PD state with 5 sublattices [15]. The orientation of ordered spins is perpendicular to the triangular plane. The broken line indicates the magnetic unit cell.

Based on the neutron scattering experiment, the spin arrangement can be expected to be up-down-up-down-disordered... along the b -axis, as shown in Fig. 2.12. This would originate from the small ferromagnetic moments at the disordered spins although the detailed magnetic structure is not still unveiled. The validity of the PD model has also been confirmed by μSR measurements performed by Sugiyama *et al.* [16]. They studied the local internal magnetic field of Ag_2CrO_2 in detail, and revealed that this antiferromagnetic transition is induced by the first-order structural phase transition at T_N .

To summarize these experiments, typical properties of Ag_2CrO_2 are listed as below:

1. Antiferromagnetic triangular lattice with $S = 3/2$ with strong Ising anisotropy along the c -axis.
2. Magnetic transition appears at $T_N = 24$ K accompanied with the structural transition.
3. Conduction electrons and localized moments are strongly coupled in Ag_2CrO_2 .

On the other hands, since the single crystal has not been synthesized yet, the following problems has not been clarified.

1. The origin of the residual magnetization at low temperatures
2. Ag ion valence
3. The origin of the structural transition below T_N

Part II

Spin transport measurement

Chapter 3

Spintronics

In this chapter, we briefly explain the concept of spintronics. Especially, we introduce what kind of physical quantities can be discussed from results of spin transport measurements.

3.1 History of spintronics

Here, we review the history of spintronics. The first topic is the giant magnetoresistance (GMR) and tunnel magnetoresistance (TMR). These are the most successful parts in spintronics. The second topic is nonlocal spin valve (NLSV) which is closely related with the present studies.

3.1.1 Giant magnetoresistance

Spintronics is one of the central fields in modern condensed matter physics. The aim of spintronics is to explore new spin-related phenomena and to create spintronic devices by controlling the spin degree of freedom. Spintronics has been developed since 2000, but it is based on the electrical properties in magnetic materials that have a long history. For example, researches on the electrical conductivity in ferromagnets have been investigated for a long time, and a phenomenon that the electrical conductivity depends on the direction of magnetization is known as the anisotropic magnetoresistance (AMR) [61], where the resistance changes depending on the angle between a current direction and an orientation of the magnetization. The origin of the AMR is the spin-dependent scattering in the material. Mott discovered that in ferromagnets, electrons with majority spin and those with minority spin do not mix and the total conductivity can be expressed as a sum of each spin channel when the temperature is low enough so that magnon scattering is negligible [62]. Such a two-current model is based on recent spintronics studies. In 1880, Hall discovered an anomalous Hall effect (AHE) in ferromagnetic materials (Fe, Co, Ni) even at zero magnetic field [63]. The AHE is proportional to the magnetization of ferromagnetic material. In 1954, Karplus and Luttinger first explained the AHE theoretically using the electron band structure [64].

The GMR effect was discovered in 1988 by two independent groups [65, 66]. They fabricated several tens multilayers, composed of a few nanometer thick Fe and Cr, where the adjacent Fe layers are antiferromagnetically coupled via the Cr layer. When the in-plane magnetic field is applied, the Fe layers align in parallel, and the MR shows dramatically large values (Fig. 3.1). The MR ratio, which is defined as the ratio between the resistances at zero field and at high magnetic field $\frac{R(H)-R(0)}{R(0)}$, is a few orders of magnitude larger than the conventional AMR ratio ($\sim 1\%$). These GMR experiments are a clear evidence of spin-polarized transport. Thus, the discovery of the GMR effect stimulated intensive studies to enhance the MR ratio.

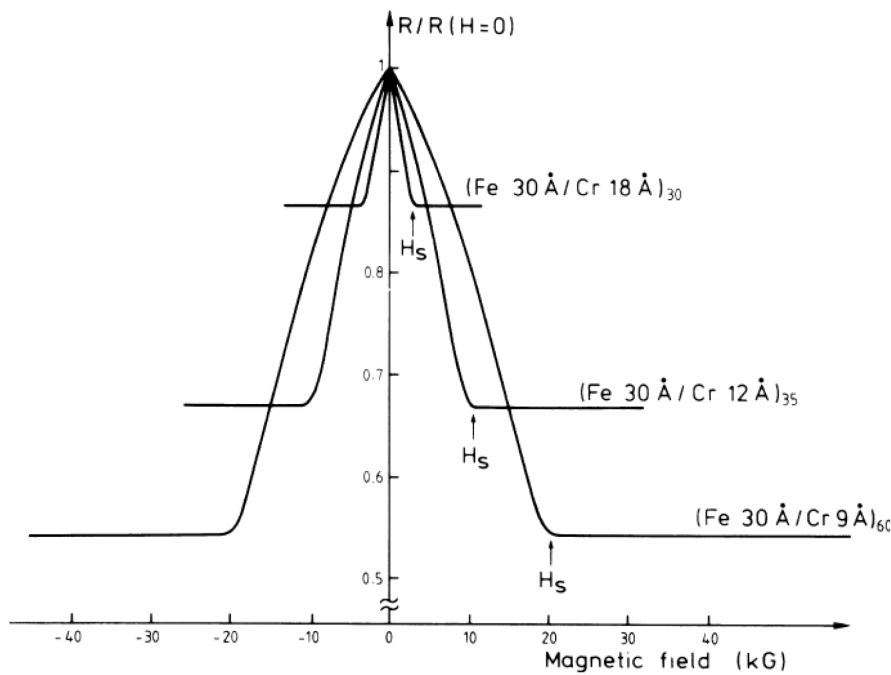


Figure 3.1: The first report of the GMR effect by Baibich *et al.* [65].

The TMR effect was discovered by replacing the Cr layer by a thin insulating layer [67, 68].

In an early stage of the TMR experiments, amorphous AlO_x was used and the MR ratio stayed at $\sim 50\%$. The next breakthrough is the use of MgO layer. The lattice of MgO used as an insulating layer fits well with Fe and also allows only up-spin channel to tunnel in the barrier. As a result, the MR ratio has increased dramatically, reaching several hundred percent by the middle of 2000 [69, 70]. The TMR ratio is summarized in Fig. 3.2 [71]. Thanks to the large TMR ratio, TMR devices are currently used as HDD magnetic heads, Magnetoresistive Random Access Memories (MRAMs) [72, 73], and magnetocardiography [74].

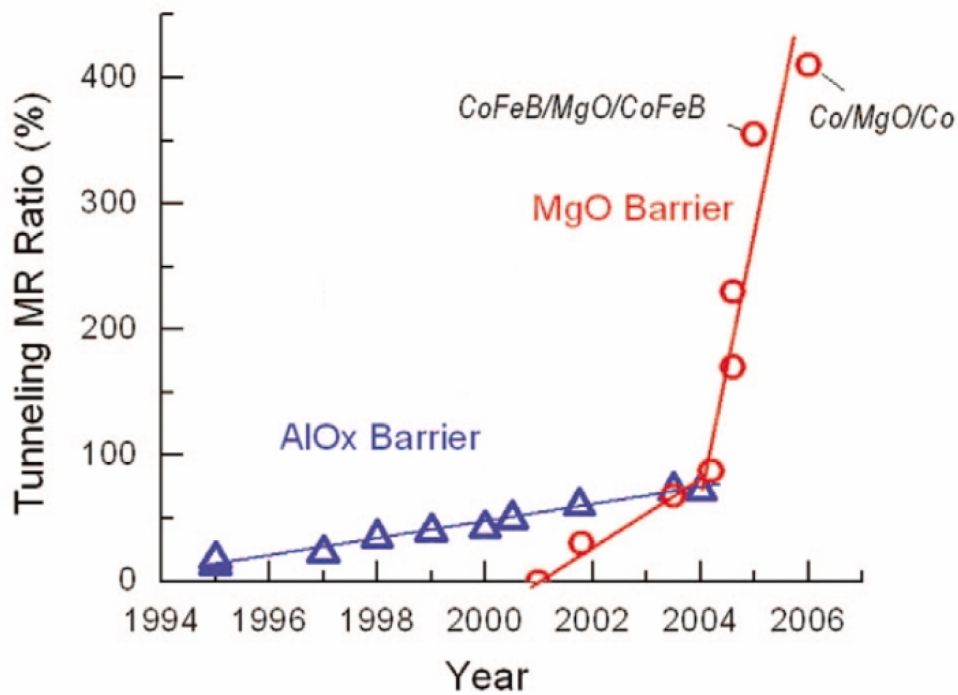


Figure 3.2: The history of the TMR ratio [71].

3.1.2 Nonlocal spin valve

On the other hands, several years before the discovery of the GMR effect, Johnson and Silsbee fabricated a lateral spin valve structure as shown in Fig. 3.3(a) and detected the voltage signal related to spin accumulation in the lateral spin valve structure [75]. There are two types of spin valves. One is a vertical spin valve and the other is a lateral spin valve. The vertical spin valve has a stacked structure along the film-thickness direction like a GMR device. On the other hand, in the lateral spin valve device, two small ferromagnetic NiFe (Py: Permalloy) pads were placed on an aluminum foil, as shown in Fig. 3.3(a). These two pads work as a spin injector and detector. Using this device, they detected a voltage difference related to the magnetization configuration (parallel/antiparallel) of the two ferromagnets.

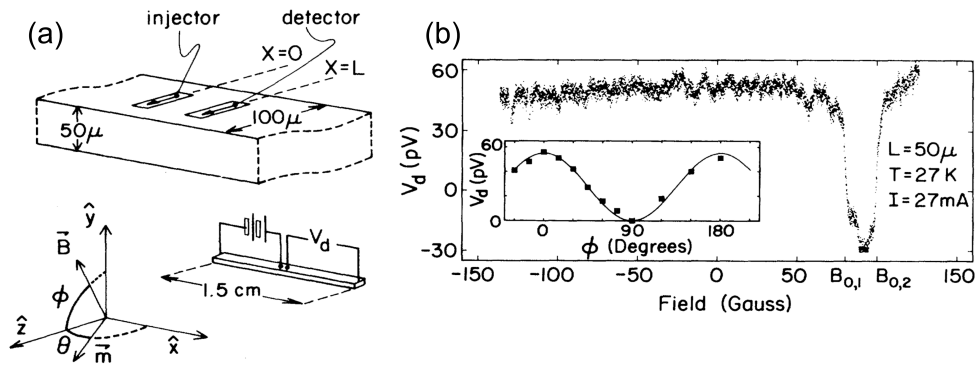


Figure 3.3: The demonstration of pure spin current injection and detection by Johnson and Silsbee [75]. (a) The schematic image of the device structure. An electric current flowed from the injector to one end of the foil and a nonlocal voltage was detected between the detector and the other end of the foil. (b) A typical result of the detected voltage. The inset shows the magnetic angle dependence of the nonlocal voltage.

The voltage signal in this study is small compared to the GMR effect, but the importance of this work is that it was the first demonstration of the generation and detection of “pure spin current” which is a flow of spin angular momentum without any charge flow (Fig. 3.4).

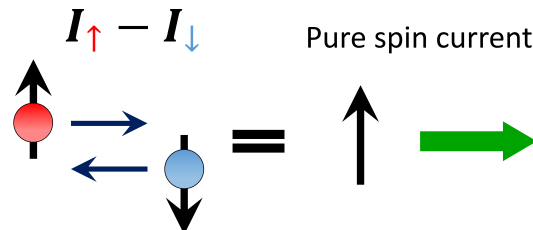


Figure 3.4: The schematic image of pure spin current. When up-spin electrons and down-spin electrons flow in opposite directions, a flow of only the spin angular momentum is generated.

As shown in the previous subsection, the thickness of multilayer structures in GMR and TMR devices is of the order of nanometers. The biggest difference between a charge current and a spin current is that the spin angular momentum is not a conserved quantity, and the pure spin current decays within a characteristic scale (spin diffusion length: SDL or spin relaxation time). Therefore, to perform the spin transport measurement, we have to fabricate the device structure within the SDL (in metals, the SDL ranges from a few nm to a few μm). The spin accumulation signal measured by Johnson and Silsbee was small because the SDL of Al is ~ 500 nm and it was much shorter than their device. Compared to the layered structure for the GMR effect, it is more difficult to fabricate a nano-scale lateral spin valve structure because the fabrication process is restricted by the resolution of nano-technology, *i.e.*, an electron beam lithography method. Therefore, experiments of the lateral spin valve have been developed with the progress of the microfabrication technology.

About fifteen years after the first demonstration of the nonlocal spin injection by Johnson and Silsbee, a controlled experiment on nonlocal spin injection and detection was reported by Jedema *et al.* (Fig. 3.5) [76].

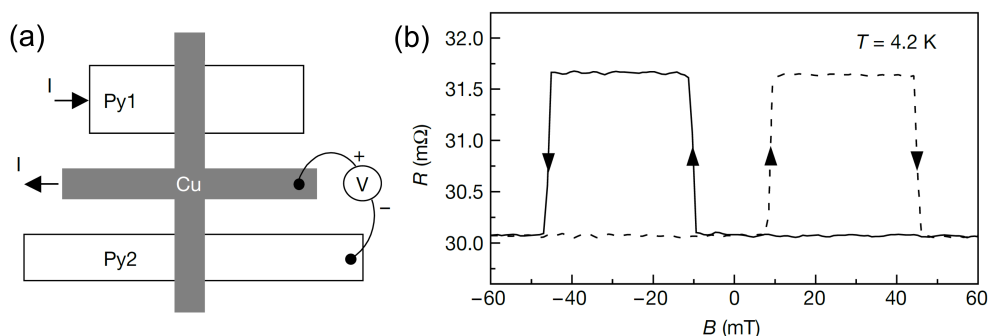


Figure 3.5: Nonlocal spin injection and detection reported by Jedema *et al.* [76]. (a) A schematic image of the device. The charge current flows between the Py wire and one of the arms in the Cu cross, and the voltage is detected between the other arm of the Cu wire and the other Py wire. (b) Nonlocal spin signal at 4.2 K.

They prepared nanometer-scale lateral spin valves and generated spin currents by passing a charge current from a ferromagnet to a nonmagnet. In their experiments, a much larger spin signal compared with that measured by Johnson and Silsbee was observed because of progress in the nanofabrication technique which enabled them to make the distance between the two voltage probes less than the SDL of Al.

We note that this kind of lateral spin valve is one of the most powerful tools to produce spin currents from charge currents. Inspired by the work by Jedema *et al.*, many studies have been carried out to investigate spin transport properties for different kinds of materials and to find good materials for an efficient spin current generation, transport and detection.

In 2007, Kimura and Vila *et al.* fabricated a NLSV device an insertion of a Pt wire [77–79] in between two Py wires and put a Cu bridge on the three wires as depicted in Fig. 3.6(a). This method is called as the spin absorption method which can be measured not only the SDL of Pt but also the spin Hall effect (SHE). The detail of the SHE is described in the next section.

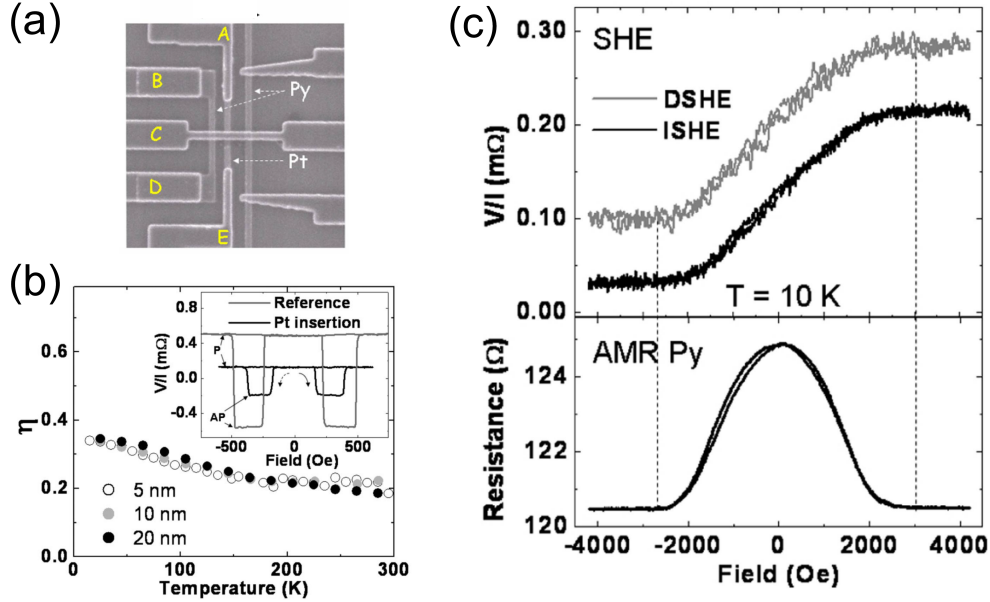


Figure 3.6: The demonstration of the spin absorption method reported by Vila *et al.* [79]. (a) Scanning electron microscope (SEM) image of a typical device for SHE measurements. (b) The temperature dependence of the spin absorption rate η . The inset shows NLSV signals measured at 5 K using the lateral spin valves with and without the Pt wire, clearly indicating parallel (P) and antiparallel (AP) states. (c) Direct spin Hall effect (DSHE) and inverse spin Hall effect (ISHE) measured at $T = 10$ K, together with the AMR of the Py wire measured with the same condition.

They estimated η that is the ratio between the nonlocal spin signals with and without the Pt wire. From η , the SDL λ can be estimated to be ~ 7 nm. This method is called the spin absorption method [6]. As detailed in the next subsection, the spin Hall effect can be measured using the same device (Fig. 3.6(c)). Therefore, the spin absorption method is recognized as one of the ways to investigate spin transport properties in strong spin-orbit (SO) materials.

3.2 Spin Hall effect

In addition to the lateral spin valve structure described above, there is another way to generate a pure spin current from a charge current, that is the SHE (Fig. 3.7).

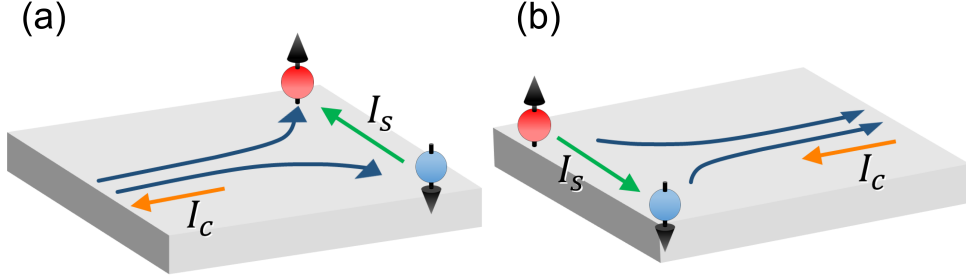


Figure 3.7: Schematic images of (a) SHE and (b) ISHE.

Between a charge current I_C and a pure spin current I_S , the following relation holds:

$$I_S = \alpha_H^{\text{SHE}} I_C, \quad I_C = \alpha_H^{\text{ISHE}} I_S \quad (3.1)$$

where α_H^{SHE} and α_H^{ISHE} indicates a conversion efficiency called “spin Hall angle (SH angle)”. Generally, α_H^{SHE} is equal to α_H^{ISHE} using the Onsager reciprocal relation. The SHE has attracted much attention since the 21st century, but it was originally predicted in 1971. D’yakonov and Perel proposed that when a charge current flows in a semiconductor, spins with opposite angular momenta are spatially separated by the spin-orbit interaction (SOI), and spin accumulation may take place at the edges of semiconductor [7]. However, this study was not so attracted at that time because there was no experimental way to detect the pure spin current.

About 30 years later, how to measure the SHE was re-proposed by Hirsch in 1999 [8]. This mechanism was based on the SOI derived from the electron band structure, and was equivalent to the intrinsic mechanism of the AHE in ferromagnets [64].

After that, Kato *et al.* observed spin accumulation at both edges of a semiconductor GaAs thin wire using the optical Kerr effect. It was the first direct demonstration of the SHE (Fig. 3.8) [9].

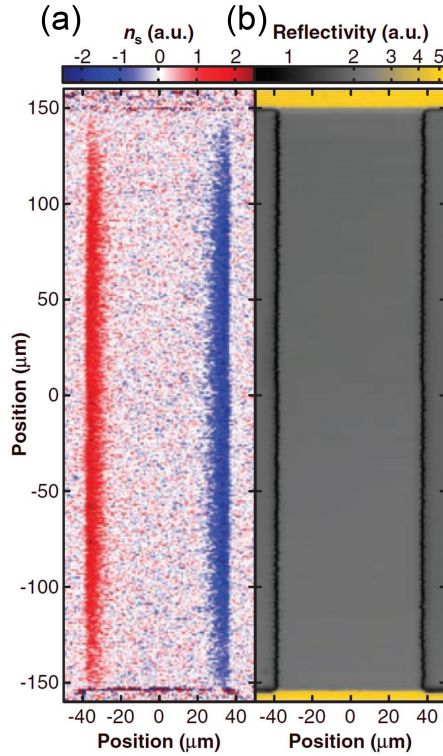


Figure 3.8: The first observation of the SHE by Kato *et al.* [9]. Two-dimensional mappings of (a) spin density n_s and (b) reflectivity R for the unstrained GaAs sample measured at $T = 30$ K and $E = 10$ mV μm^{-1} .

In semiconductors, however, the SH angle was so small that this result was not directly connected to spintronic application. The next breakthrough was the detection of the SHE and its inverse in metal-based devices in 2006. Saitoh *et al.* fabricated a Pt/Py ($\text{Ni}_{81}\text{Fe}_{19}$) bilayer film. By applying a microwave to the film, a ferromagnetic resonance occurs and the pure spin current injected into Pt via the damping process of ferromagnetic resonance. The injected pure spin current is converted into a charge current through the ISHE and detected as a charge accumulation. This method is known as the spin pumping method. They found a large ISHE in Pt [10]. At the same time, Valenzuela and Tinkham measured the ISHE in Al, but the spin Hall angle was relatively small (3×10^{-4}) [11]. Since the discovery of the large ISHE in Pt, there have been many reports to realize large SH angles because it is closely related to device applications.

In 2008, Tanaka *et al.* theoretically studied the SH conductivity based on the intrinsic mechanism [80]. They calculated electrical band structures of $4d$ and $5d$ transition metals by using the multi-orbital tight-binding model and obtained the SH conductivity by using a linear-response theory. They revealed that the SH conductivity strongly depends on the electron number $n = n_s + n_d$, where n_s is the number of electrons in the s -orbit and n_d is the number of electrons in the d -orbit, respectively, regardless of the detailed crystal structures. They also predicted that large positive SH conductivities should be obtained in Pt($5d^96s^1$) and Pd ($4d^{10}5s^0$), whereas large negative SH conductivities in Ta($5d^36s^2$) and W($5d^46s^2$). These predictions were experimentally confirmed in the SH measurement in $4d$ and $5d$ transition metals using the spin absorption method (Fig. 3.9) [81].

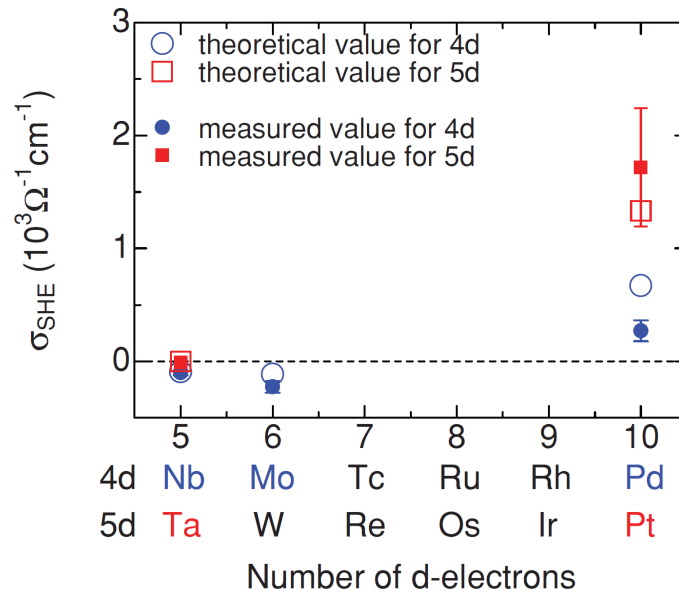


Figure 3.9: SH conductivities of $4d$ and $5d$ transition metals obtained with the spin absorption technique by Morota *et al.* [81]. The closed and open symbols show the experimentally and theoretically obtained SH conductivities of experimental (closed symbols) theoretical (open symbols) as a function of d electrons for $4d$ (circle) and $5d$ (square) transition metals.

A similar tendency has been observed even in $3d$ transition metals. Du *et al.* observed the SH angles of $3d$ transition metals as a function of the number of $3d$ -electrons by means of the ferromagnetic resonance (FMR) (Fig. 3.10) [82]. They revealed that the d -orbital filling rather than the atomic number Z plays a dominant role in the SHE in $3d$ transition metals, reminiscent of the behavior in $4d$ and $5d$ transition metals.

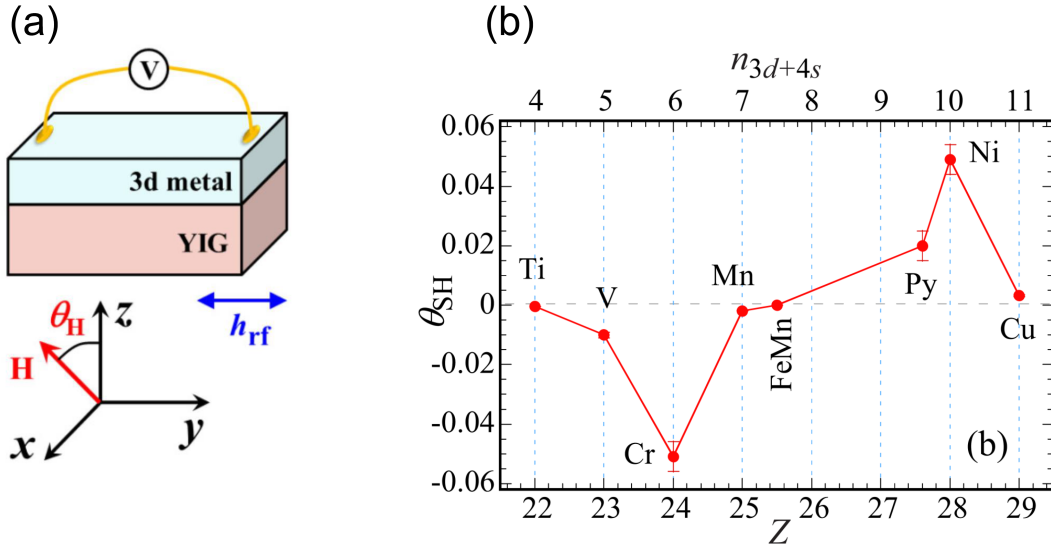


Figure 3.10: (a) Measurement setup for the ISHE using the FMR technique by Du *et al.* [82]. (b) The SH angle θ_{SH} as a function of the number of the atomic number Z .

As mentioned above, the SHEs in single elements have been experimentally investigated by many groups [11, 79, 81–83]. However, the reported SH angle, for example of a typical SH material Pt, is widely distributed from 0.003 to 0.2. The origin of this distribution has been revealed recently. Segasta *et al.* studied the impurity effect on the SHE in Pt, and claimed that the SHE strongly depends on the purity of material [83].

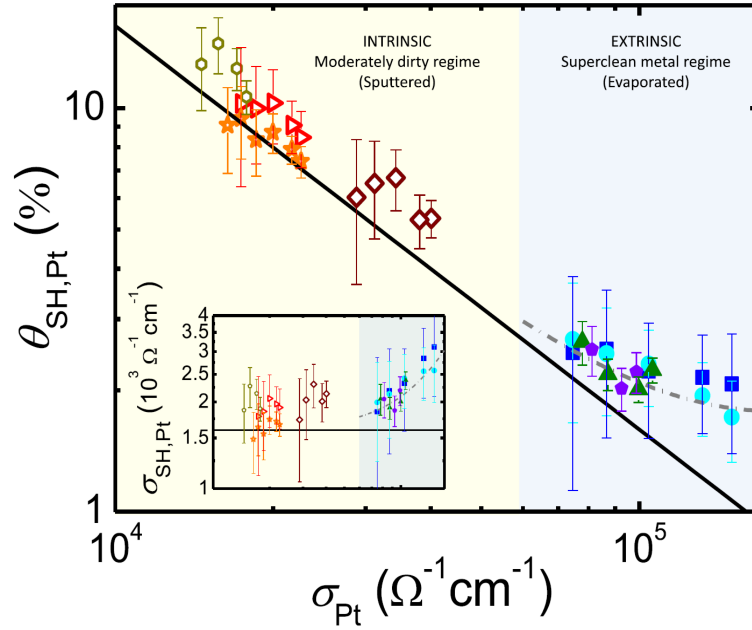


Figure 3.11: The scaling plot of the SH angle of Pt reported by Segasta *et al.* [83].

As shown in Fig. 3.11, the SH angle θ_{SH} increases with decreasing the longitudinal conductivity. This fact indicates that the scattering at impurities or grain boundaries is essential to the SHE in Pt. On the other hand, some binary alloys also show large SH angles [84–87]. For instance, by adding a small amount of strong spin-orbit impurities such as Ir or Bi, into a host weak spin-orbit metal Cu, these alloys show huge SHEs compared to the single element alone [85, 86]. Especially, the SH angle of CuBi is -24% [86]. This is much higher than those of $4d$ and $5d$ transition metals. The origin of the large SHE is different from the SHE in transition metals. We will describe the mechanism of the SHE in the next chapter.

3.2.1 Spin Hall effect in magnetic materials

It has been commonly believed that the SHE and its inverse occur only in non-magnetic material with strong SOI. But recently, these effects even occur in magnetic materials. In this subsection we introduce some examples of spin transport measurements in magnetic materials.

In 2013, Miao *et al.* reported the ISHE of Py by using the spin Seebeck effect [88]. The device was composed of a thin Py film on a polycrystalline $\text{Y}_3\text{Fe}_5\text{O}_{12}$ (YIG) substrate (Fig. 3.12(a)). They applied a thermal gradient perpendicular to the YIG substrate and detected the transverse voltage at the two ends of the of Py film.

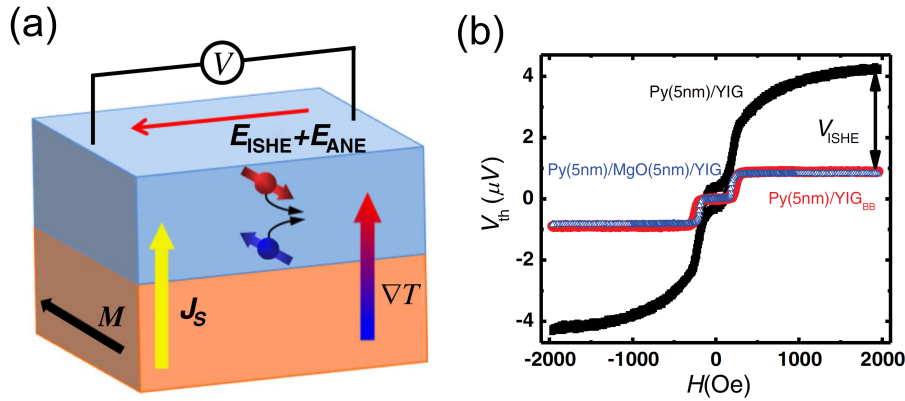


Figure 3.12: The first demonstration of ISHE in Py reported by Miao *et al.* [88]. (a) The schematic image of the device. (b) The spin Seebeck effect of Py/YIG device, Py/MgO/YIG and Py/surface-etched YIG, respectively.

The measured voltage is shown in Fig. 3.12(b). They estimated the SH angle α_H of Py is about $\sim 0.5\%$. They claimed that this observation paved the way to exploit ferromagnetic metals as superior pure spin current detectors. The ISHE was even observed in CoFeB [89] and Co [90].

Tian *et al.* reported the relation between the SHE and the magnetization orientation of ferromagnets [90]. They fabricated Co/Cu/YIG devices and controlled the magnetization directions of Co and YIG by applying a magnetic field. By using the spin Seebeck effect, the ISHE of Co was evaluated. They found that the ISHE of Co is independent of the magnetization direction of Co. The result indicates that the SHE in ferromagnets are uniquely determined by its band structure independent of the its magnetization direction which is known as the intrinsic mechanism of the AHE [64]. On the other hand, Das *et al.* studied the relation between the ISHE and the magnetization direction of Py [91]. They discovered the magnetization-dependent SHE (Anomalous spin Hall effect: ASHE) for Py. According to their report, the ASHE originates from a lower magnetization of Py than that of Co. The ASHE was also observed in FeGd/CoFeB bilayer devices [92]

Very recently, the magnetic spin Hall effect was also observed in Mn_3Sn which is known as one of the triangular antiferromagnetic material [93].

3.2.2 Spin Hall effect near the magnetic transition

Just before the discovery of the ISHE in Py, Wei *et al.* reported the ISHE in PdNi by using the spin absorption method [12]. PdNi is known as a weak ferromagnet and its T_C can be controlled by the Ni concentration. They prepared the Pd_{100-x}Ni_x ($x = 7, 8,$ and 9) alloys by implanting Ni ions into Pd. T_C was determined from AHE measurements. Far above and below T_C , a standard ISHE signal was detected. However, an anomaly in the ISHE signal appeared only in the vicinity of T_C ; the ISHE signal was suppressed and enhanced below and above T_C respectively, as shown in Fig. 3.13(a).

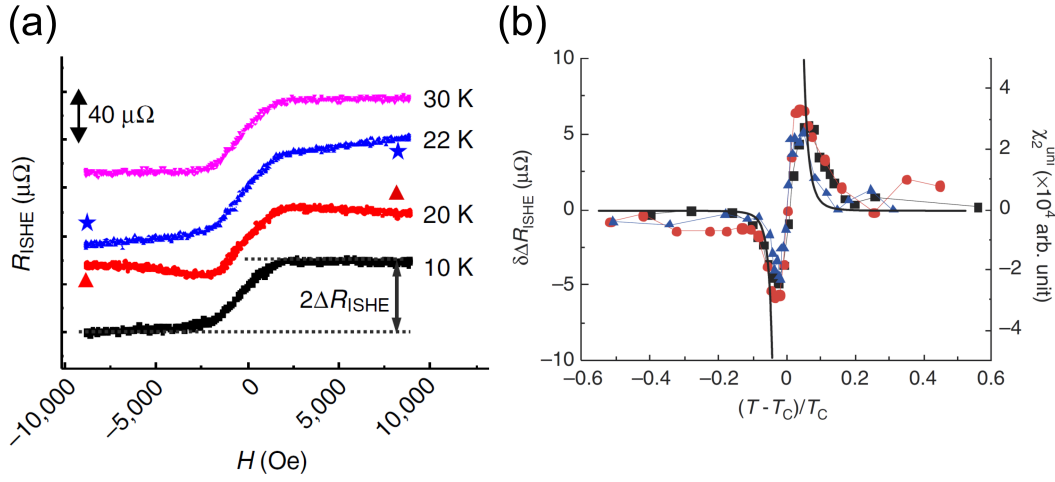


Figure 3.13: The ISHE of PdNi reported Wei *et al.* [12]. (a) The ISHE signals of Pd₉₂Ni₈ at $T = 10, 20, 22, 30$ K. (b) The anomalous component ΔR_{ISHE} for Pd_{100-x}Ni_x as a function of the reduced temperature $(T - T_C)/T_C$. The black square, red circle and blue triangle indicate the ΔR_{ISHE} for $x = 7, x = 8$ and $x = 9$, respectively. The solid line shows the uniform second-order nonlinear susceptibility χ_2 .

To focus on the anomaly near T_C , they subtracted the normal ISHE component and plotted only the anomaly part as a function of the reduced temperature $(T - T_C)/T_C$ (Fig. 3.13(b)). A universal curve (see the solid curve in Fig. 3.13(b)) independent of the Ni concentration has been observed. This behavior can be explained qualitatively by higher-order magnetic susceptibility. In 1962, Kondo calculated the AHE in a ferromagnet including the second perturbation of the s - d Hamiltonian and revealed that the anomaly of ρ_H in the AHE appears from the third-order magnetic fluctuation of localized moments $\chi_1 \sim \sum \langle (M - \langle M \rangle)^3 \rangle$ [94]. In the case of the AHE, up-spin and down-spin conduction electrons are scattered to opposite directions and the anomaly of ρ_H is proportional to the difference of scattering amplitudes between up-spin and down-spin electrons, that is, χ_1 . On the other hand, in the ISHE, both up-spin and down-spin electrons are scattered to the same side. Thus, the obtained R_{ISHE} is proportional to the sum of scattering amplitudes between up-spin and down-spin electrons, that is, $\chi_2 = \chi_2 \sim \sum \langle (M - \langle M \rangle)^4 \rangle$ [12, 95].

Followed by the result that the SHE reflects the nonlinear magnetic susceptibility, Niimi *et al.* measured the SHE in ternary alloy spin glasses: $\text{Cu}_{99.5-x}\text{Mn}_x\text{Bi}_{0.5}$ ($x = 0.5, 1.0, \text{ and } 1.5$) by means of the spin absorption method in the lateral spin valve structure (see Fig 3.14) [13]. According to the previous result on the SHE in ferromagnetic material [12], an anomaly in the SHE can be expected at the spin glass temperature T_f because χ_2 diverges at T_f .

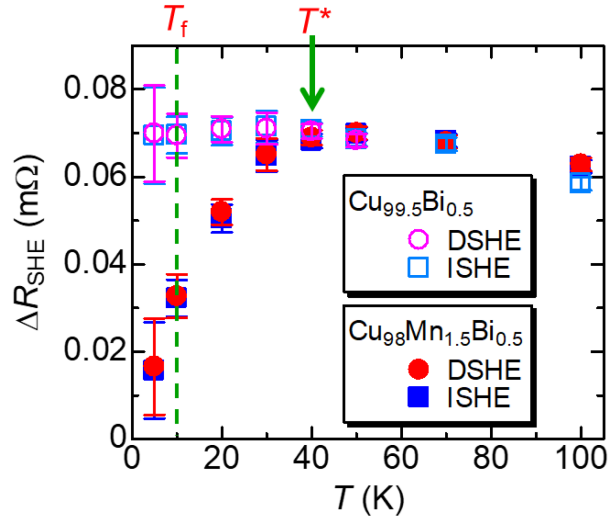


Figure 3.14: DSHE and ISHE in $\text{Cu}_{98}\text{Mn}_{1.5}\text{Bi}_{0.5}$ [13].

However, the expected anomaly was not observed at T_f estimated from the magnetization measurement of the thin film as shown in Fig. 3.14. Instead, the SHE in ternary alloys starts to decrease at about 4 times higher temperature than T_f and continues to decrease even below T_f . This behavior is qualitatively different from the previous SHE in magnetic materials. The generated current I_C via the SHE can be expressed as $\vec{I}_C \propto \vec{I}_S \times \vec{s}$ where \vec{s} is the spin polarization of conduction electrons. Therefore, the decrease of ISHE indicates the reduction of \vec{I}_S or the reduction of \vec{s} . According to their results of the spin absorption rate, which allows to evaluate the absolute value of \vec{I}_S quantitatively, $|\vec{I}_S|$ does not strongly depend on temperature. Thus, the origin of the reduction of SHE is due to the reduction of the spin polarization. In order to understand the reduction of ISHE theoretically, they performed a numerical calculation based on an extended Kubo-Toyabe model [96] and quantitatively reproduced the experimental results. However, the relation between T^* at which the SHE starts to decrease and T_f has not been elucidated yet.

The ISHE was also measured in an antiferromagnetic material IrMn near the magnetic transition temperature. Frangou *et al.* performed the spin pumping measurement around the magnetic transition temperature of IrMn [97]. They fabricated the NiFe/Cu/IrMn trilayer device (inset of Fig. 3.15(a)), and estimated the magnetic damping factor of NiFe as a function of temperature with various IrMn thicknesses (Fig. 3.15(b)).

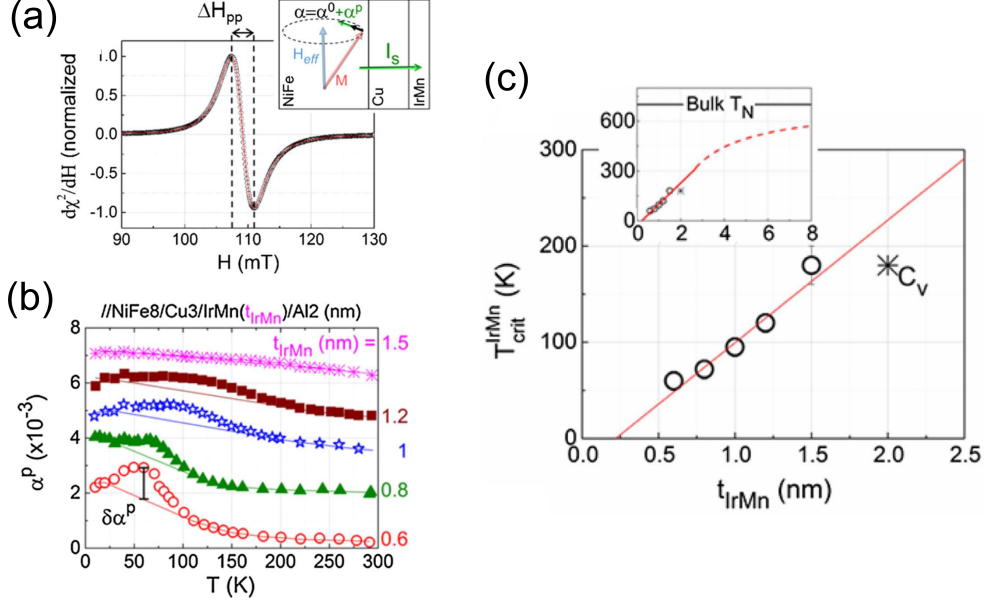


Figure 3.15: Spin pumping in NiFe/Cu/IrMn trilayer devices with various IrMn thicknesses [97]. (a) Typical differential absorption spectrum at the resonance field. The inset is a diagram of the spin pumping experiment. (b) Temperature dependence of the effective damping factor α^p . (c) Thickness dependence of the critical temperature of IrMn. The red line shows a fitting based on a formula shown by Zhang *et al.* [98] and C_v is taken from a paper by Petti *et al.* [99]. The inset is a wider scale of the critical temperatures as a function of IrMn thickness.

The effective damping factor ($\alpha^p(T) = \alpha(T) - \alpha^0(T)$) has a peak at low temperatures (T_{crit}). With decreasing the thickness of the IrMn layer, the peak amplitude becomes larger and the width becomes narrower. According to a recent theory, the peak height $\delta\alpha^p$ (see the definition in Fig. 3.15(b)) is proportional to the interfacial spin conductance which depends on the dynamic transverse spin susceptibility [100]. Therefore, the peak of $\delta\alpha^p$ indicates that the dynamic spin susceptibility of IrMn has a peak at low temperatures. Figure 3.15(c) shows that T_{crit} of the IrMn layer deduced from Fig. 3.15(b) has a linear relation to the thickness. This behavior is consistent with theoretical calculations where the finite size effect of Néel temperature is taken into account [98]. However, it has been an open question whether T_{crit} is equivalent to T_N . Similar results were also observed in YIG/NiO/CoO/Pt trilayers [101]. These results indicate that the spin transport measurements can be used for the further investigation of nontrivial magnetic orders, such as antiferromagnetism, with no net magnetic moment.

3.3 Theory of anomalous Hall effect

It is widely recognized that the SHE and the AHE share the same origin. Since the AHE has a much longer history and is well-studied, we start with the theoretical descriptions of the AHE.

The Hall effect is the transverse voltage generation by the electric field under a finite magnetic field. In such a situation, the Hall current is generated due to the Lorentz force, and the Hall conductivity is represented as $\sigma_{xy} = j_y^C / E_x$ where j_y^C is a transverse current and E_x is an applied electric field. Since the conductivity tensor σ and resistivity tensor ρ are connected with their inverse matrices, the following relation can be derived:

$$\rho_{xx} = \frac{\sigma_{xx}}{\sigma_{xx}^2 + \sigma_{xy}^2}, \quad \rho_{yx} = \frac{\sigma_{xy}}{\sigma_{xx}^2 + \sigma_{xy}^2}. \quad (3.2)$$

The AHE is one of the most fundamental and important electrical transport properties in magnetic materials. The first report of the AHE is 1880 [63]. Further systematic examinations of the AHE were performed by Kundt. He measured Hall resistance in Fe, Co and Ni and found that the saturation magnetization was roughly proportional to the magnetization M_z [102]. Pugh has proposed the following relationship:

$$\rho_{yx} = R_0 H_z + R_s M_z, \quad (3.3)$$

where ρ_{yx} is the Hall resistance, H_z is the external field, and M_z is the magnetization [103]. The first term of the right side is the ordinary Hall effect which is inversely proportional to the carrier density. The second term is the AHE which is proportional to the spontaneous magnetization of magnetic materials. There are many researches about the origin of the AHE. In the following, we discuss an intrinsic mechanism and an extrinsic mechanism [104].

3.3.1 Intrinsic mechanism

The first argument of anomalous Hall (AH) coefficient R_s in Eq. (3.3) was reported by Karplus and Luttinger (KL) [64]. In a ferromagnetic material, conduction electrons are coupled to the magnetization through a SOI. When an external electric field E is applied to the material, the whole Hamiltonian \mathcal{H}_T can be written as follows:

$$\mathcal{H}_T = \mathcal{H}_0 + \mathcal{H}_{\text{SOI}} + \mathcal{H}_E. \quad (3.4)$$

The first term is $\mathcal{H}_0 = \frac{p^2}{2m} + V(r)$, where p is the momentum of the electron, m is the mass of the electron, and $V(r)$ is a periodic potential energy of crystal. The second term is the SOI term and $\mathcal{H}_{\text{SOI}} = [\sigma \times \nabla V(r)] \cdot \frac{\mathbf{p}}{4m^2 c^2}$ where c is the speed of light. The third term is the perturbation term under the electrical field and $\mathcal{H}_E = -\mathbf{E} \cdot \mathbf{r}$ where \mathbf{r} is the position of the electron. KL computed the effect of the spin-orbit coupling (SOC) on the transverse conductivity of material. They showed that when an external electrical field is applied to a ferromagnetic material, electrons obtain an additional contribution to the group velocity. This KL's anomalous velocity perpendicular to the electrical field could explain the Hall voltage.

The longitudinal electrical conductivity and ordinary Hall conductivity can be characterized by an electrical relaxation time τ because electrons in each band are accelerated by an applied electrical field. On the other hand, the KL intrinsic mechanism originates from interband scatterings. Thus, the AH conductivity does not depend on τ but on the band energy difference. This indicates that the KL AH conductivity is uniquely determined by an intrinsic value independent of crystal disorder and impurities. In other words, it is possible to determine the AH conductivity by the band structure of material through the first principle calculation.

However, the KL's theory had not been attracted for a long time because of its intuitive difficulty. The perturbation term of σ_{xy} in terms of the SOI energy $E_{SO} \sim \xi M$, where ξ is the SOC and M is the magnetization, is usually much smaller than the bandwidth. Therefore, it had been thought that KL theory cannot capture topological nature involved in the intrinsic AHE. However, recent reports revealed that the KL's general expression for the intrinsic band contribution actually corresponds to the topological properties of its band structure, *i.e.*, Thouless-Kohmoto-Nightingale-den Nijs (TKNN) formula [105], and showed that each band contains a finite Chern number [106, 107].

Berry curvature in anomalous Hall effect

Recently, the intrinsic mechanism has attracted renewed interest from the viewpoint of Berry curvature. Before discussing the relation between the intrinsic mechanism in the AHE and topological nature, we mention the topological property in the Hall effect. The quantum Hall effect is the first trigger for introducing topological nature into the Hall effect. The quantum Hall effect was first discovered using semiconductor heterostructure devices, where the two-dimensional electron gas is formed, under a strong magnetic field [108]. In a perfect crystal, the Hall conductivity can be written as

$$\sigma_{ij}^{\text{TKNN}} = \left(\frac{e^2}{h} \right) N_{\text{Ch}} \quad (3.5)$$

$$N_{\text{Ch}} = \frac{1}{2\pi} \int d^2k [\nabla_{\mathbf{k}} \times \mathbf{a}(\mathbf{k})]_z, \quad (3.6)$$

where N_{Ch} is called the Chern number and $\mathbf{a}(\mathbf{k}) = i\langle n, \mathbf{k} | \nabla_{\mathbf{k}} | n, \mathbf{k} \rangle$ is the Berry phase connection of the occupied band. The sum of N_{Ch} over the occupied bands determines the integer ν for the quantization of the Hall conductivity $\sigma_{xy} = \nu e^2/h$. It is noted that the quantized Hall conductivity depends not on impurities in materials but on the topological feature of a band structure. The intrinsic contribution to the Hall conductivity depends only on the perfect crystalline band structure. Therefore, it can be calculated directly from the simple Kubo formula, given the eigenstates $|n, \mathbf{k}\rangle$ and eigenvalues $\epsilon_n(\mathbf{k})$ of the Bloch Hamiltonian \mathcal{H}_0 in Eq. (3.4),

$$\begin{aligned} \sigma_{ij}^{\text{AH-int}} &= e^2 \hbar \sum_{n \neq n'} \int \frac{d\mathbf{k}}{(2\pi)^d} [f(\epsilon_n(\mathbf{k})) - f(\epsilon_{n'}(\mathbf{k}))] \\ &\times \text{Im} \frac{\langle n, \mathbf{k} | v_i(\mathbf{k}) | n', \mathbf{k} \rangle \langle n', \mathbf{k} | v_j(\mathbf{k}) | n, \mathbf{k} \rangle}{[\epsilon_n(\mathbf{k}) - \epsilon_{n'}(\mathbf{k})]^2}. \end{aligned} \quad (3.7)$$

The velocity operator $\mathbf{v}(\mathbf{k})$ is defined by using the \mathbf{k} -dependent Hamiltonian H for the periodic part of the Bloch functions:

$$\mathbf{v}(\mathbf{k}) = \frac{1}{i\hbar}[\mathbf{r}, H(\mathbf{k})] = \frac{1}{\hbar}\nabla_{\mathbf{k}}H(\mathbf{k}). \quad (3.8)$$

What makes this contribution quite unique is that it is directly linked to the topological properties of the Bloch states like the quantum Hall effect. It is proportional to the integration over the Fermi sea of the Berry curvature of each occupied band or equivalently to the integral of the Berry phases over cuts of the Fermi-surface segments. By using the above expression, one obtains:

$$\langle n, \mathbf{k} | \nabla_{\mathbf{k}} | n', \mathbf{k} \rangle = \frac{\langle n, \mathbf{k} | \nabla_{\mathbf{k}} H(\mathbf{k}) | n', \mathbf{k} \rangle}{\epsilon_{n'}(\mathbf{k}) - \epsilon_n(\mathbf{k})}. \quad (3.9)$$

Equation (3.7) can be represented as

$$\sigma_{ij}^{\text{AH-int}} = -\epsilon_{ijl} \frac{e^2}{\hbar} \sum_n \int \frac{d\mathbf{k}}{(2\pi)^d} f(\epsilon_n(\mathbf{k})) b_n^l(\mathbf{k}), \quad (3.10)$$

where ϵ_{ijl} is the antisymmetric tensor and $\mathbf{b}_n(\mathbf{k}) = \nabla \times \mathbf{a}_n(\mathbf{k})$ is the Berry curvature for the $|n, \mathbf{k}\rangle$ state. This result corresponds to the TKNN formula given in Eqs. (3.5) and (3.6).

3.3.2 Extrinsic mechanism

As mentioned in the previous subsection, the intrinsic mechanism proposed by KL had been forgotten for a while. On the other hand, to explain the AHE in ferromagnets, some extrinsic mechanisms due to impurity scattering processes were proposed in the middle of the 20th century. Here we review the extrinsic mechanisms in the AHE.

Skew scattering mechanism

Contrary to the intrinsic mechanism proposed by KL, Smit considered the effects of impurities and phonons on the AHE [109]. Within the framework of the linear response theory, the steady-state current is balanced by the acceleration of electrons due to the electric field E and the relaxation of momentum due to scattering by impurities and phonons. Smit pointed out that there is no argument in the KL theory for maintaining this equilibrium, and showed the disappearance of the KL term by the following procedure [109].

The acceleration $\dot{k} \equiv dk/dt$ should be averaged and disappear in the steady state because the force from the electrical field is canceled by that from the impurity potential. In addition, this \dot{k} is proportional to an anomalous velocity \bar{v}_a , which was thought to be negligibly small. Therefore, there should be no AHE according to the KL theory. On the other hand, Smit argued that the skew scattering mechanism was responsible for the AHE. ‘‘Skew scattering’’ means that conduction electrons are scattered by the potential of impurities in the system and bent to the opposite transverse direction, depending on the spin direction. The matrix element of the impurity scattering potential used in the skew scattering mechanism can be written as follows:

$$\langle \mathbf{k}'s' | V | \mathbf{k}s \rangle = \tilde{V}_{\mathbf{k},\mathbf{k}'} \left(\delta_{s,s'} + \frac{i\hbar^2}{4m^2c^2} (\langle s' | \boldsymbol{\sigma} | s \rangle \times \mathbf{k}') \cdot \mathbf{k} \right). \quad (3.11)$$

The microscopic equilibrium condition is that a transition probability $W_{n \rightarrow m}$ from n -th state to m -th state is equal to the inverse transition $W_{m \rightarrow n}$. This equilibrium is guaranteed by the Fermi’s golden rule:

$$W_{n \rightarrow m} = \frac{2\pi}{\hbar} |\langle n | V | m \rangle|^2 \delta(E_n - E_m), \quad (3.12)$$

where V is a perturbation including the transition n to m . However, such a microscopic equilibrium state is not so universal. For example, in the calculation within the second-order Born approximation using the third-order term of V , the equilibrium is broken. Considering a simple model in which electrons are scattered once at an impurity site, a skew scattering can be described by the asymmetric part of the transition probability:

$$W'_{\mathbf{k}\mathbf{k}}{}^A = -\tau_A^{-1} \mathbf{k} \times \mathbf{k}' \cdot \mathbf{M}_s, \quad (3.13)$$

τ^A is a relaxation time of the asymmetric part. When such an asymmetric scattering process is included, the scattering probability $W_{\mathbf{k} \rightarrow \mathbf{k}'}$ takes a different value from $W_{\mathbf{k}' \rightarrow \mathbf{k}}$. The electron scattering from impurities produces a momentum whose direction is perpendicular to the incident momentum k and the magnetization M . This is the

origin of the transverse current proportional to the longitudinal current induced by the electric field E . Therefore, the Hall conductivity σ_H is proportional to the longitudinal conductivity σ and thus the elastic scattering time τ . Furthermore, by assuming that $\sigma_H \ll \sigma$, it turns out that the Hall resistivity ρ_H is also proportional to the resistivity ρ . This extrinsic mechanism described fairly well the experimental result of Hall effect in a diluted magnetic alloy. Diluted magnetic alloys can be produced by dissolving small amounts (\approx several ppm) of magnetic impurities such as Fe, Mn, and Cr in a host metal such as Au and Cu. In diluted magnetic alloys, magnetic impurities have an isolated local moment in the temperature range higher than the Kondo temperature T_K . Thus, the magnetic susceptibility simply follows the Curie law. Hurd *et al.* measured the magnetic field dependence of Hall resistivity ρ_H in the temperature range higher than T_K [110]. The Hall coefficient R_H is represented as:

$$R_H = R_0 + \frac{A}{T}, \quad (3.14)$$

where R_0 is the ordinary Hall coefficient and A is a constant. The second term of the right-hand indicates the Curie law $\chi(T) \propto 1/T$ in the magnetic susceptibility of the localized moment. After the Hund's work, the magnetic impurity concentration dependence was investigated (see Fig. 3.16) [110–115]. It turned out that that ρ_H strongly depends on the concentration of magnetic impurities. These experiments suggest that the Hall conductivity of diluted magnetic alloys can be well-described by the skew scattering theory. Thus, the skew scattering mechanism has been recognized as a typical theory for the AHE [104].

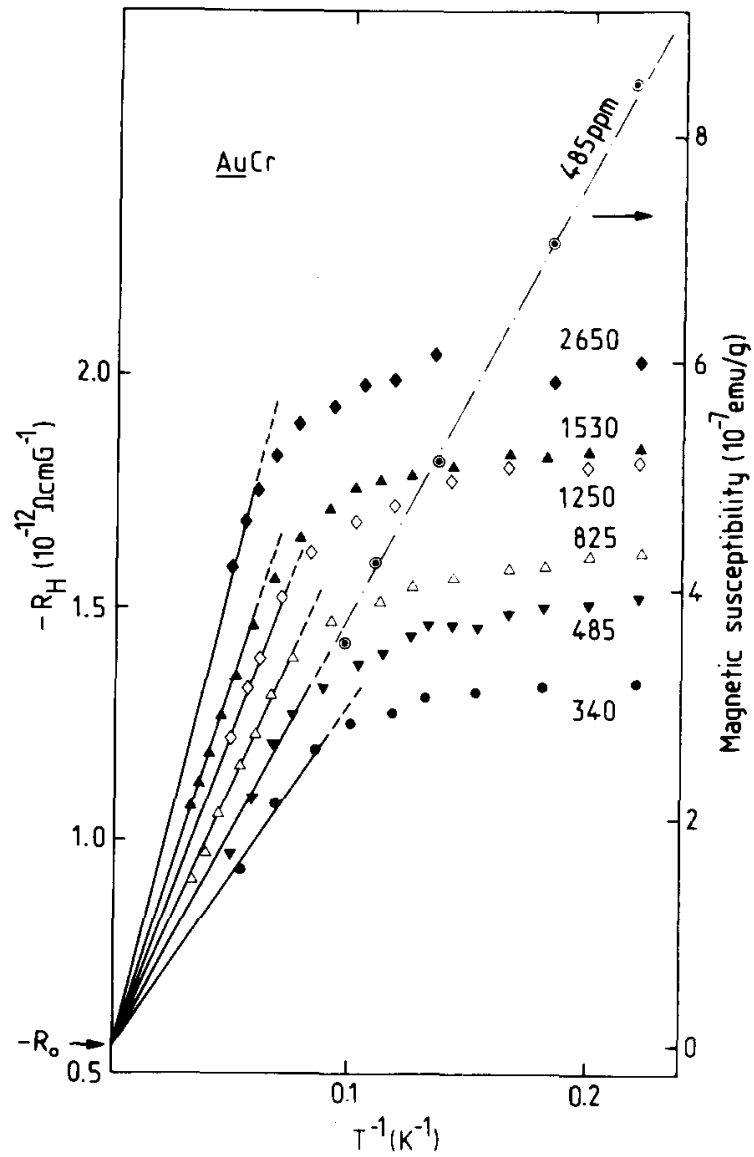


Figure 3.16: Initial Hall coefficient (left axis) and magnetic susceptibility (right axis) as a function of T^{-1} reported by Tholence and Tournier [114].

Hall conductivity in CuMnX dilute alloy

The Hall conductivity of diluted magnetic alloy was studied in detail by Fert *et al.* in 1981 [115]. They fabricated Cu-host alloys with several ppm Mn and transition metal (X). Here, the Mn impurity works as a spin polarizer to produce a spin polarized current and the X impurity works as a spin scatterer due to its strong spin-orbit interaction. In the CuMnX ternary alloys, as described in the skew scattering mechanism, the Hall resistance R_H behaves as shown in Eq. (3.14). The origin of this Hall effect is that a spin polarized current produced at the Mn site is scattered at the X site and the scattering angle depends on the direction of spin. Fert *et al.* further investigated the relation among the anomalous term A , and the species and concentrations of X (see Fig. 3.17).

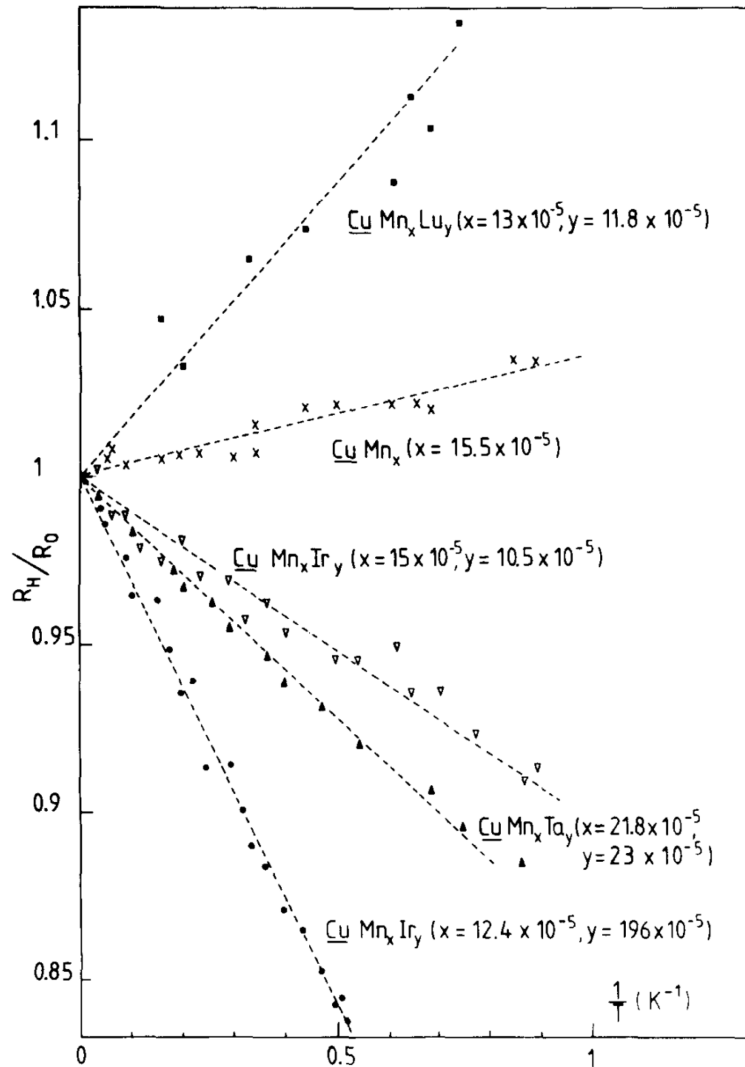


Figure 3.17: Anomalous term of Hall effect in CuMnX reported by Fert *et al.* [115].

They found that the amplitude of A depends on the species of X, and its sign is changed in case of X = Lu. Here, we consider the two-current model where up-spin ($\sigma = +$) and down-spin ($\sigma = -$) electrons have different current densities, *i.e.*, j^+ and j^- [13]. The electric field E can be written as follows:

$$\begin{pmatrix} E_x^\sigma \\ E_y^\sigma \end{pmatrix} = \begin{pmatrix} \rho_{xx} & -\rho_{yx} \\ \rho_{yx} & \rho_{yy} \end{pmatrix} \begin{pmatrix} j_x \\ j_y \end{pmatrix}, \quad (3.15)$$

where ρ is the resistivity and j is the current density. Since there is no current flow in the y direction, $j_y^+ + j_y^- = 0$. By combining with other two conditions, $E_x^+ = E_x^- = E_x$ and $E_y^+ = E_y^- = E_y$, one obtains

$$\rho_{yx}^{\text{AHE}} \equiv \frac{E_y}{j_x^+ + j_x^-} = \left(\frac{\rho_{xx}^-}{\rho_{xx}^+ + \rho_{xx}^-} \right)^2 \rho_{yx}^+ + \left(\frac{\rho_{xx}^+}{\rho_{xx}^+ + \rho_{xx}^-} \right)^2 \rho_{yx}^-. \quad (3.16)$$

When the concentration of Mn is small enough to ignore the interaction between the Mn spins, the contribution of up-spin and down-spin is equivalent and $\rho_{yx}^+ = -\rho_{yx}^- \equiv \rho_{yx}$. By substituting this condition into Eq. (3.16), the following expression can be obtained:

$$\rho_{yx}^{\text{AHE}} = \frac{\rho_{xx}^- - \rho_{xx}^+}{\rho_{xx}^+ + \rho_{xx}^-} \rho_{yx}^+ = p \rho_{yx} \quad (3.17)$$

where p is the spin polarization due to the Mn impurities. To obtain the Hall conductivity, we calculated a scattering process by using Born approximation. The s - d Hamiltonian can be written as

$$\mathcal{H} = (V_{\text{Mn}} - J_{sd} \boldsymbol{\sigma} \cdot \mathbf{S}) \sum_i^{\text{Mn}} \delta(\mathbf{r} - \mathbf{r}'), \quad (3.18)$$

where V_{Mn} is the Mn impurity potential, J_{sd} is the s - d interaction, and \mathbf{S} and \mathbf{r}_i are the Mn spin and its position, respectively. In this case, the matrix element can be expressed as:

$$\langle \mathbf{k}, \sigma | \mathcal{H} | \mathbf{k}', \sigma' \rangle = V_{\text{Mn}} \left(\delta_{\sigma, \sigma'} - \frac{J_{sd}}{V_{\text{Mn}}} \boldsymbol{\sigma}_{\sigma, \sigma'} \cdot \mathbf{S} \right) \sum_i^{\text{Mn}} e^{i(\mathbf{k}' - \mathbf{k}) \cdot \mathbf{r}_i}. \quad (3.19)$$

When the Mn concentration is small enough and $J_{sd}/V_{\text{Mn}} \ll 1$, the resistivity can be written as follows:

$$\rho_{xx}^\pm \approx \rho_{\text{Mn}}^* \left[1 \mp 2 \frac{J_{sd}}{V_{\text{Mn}}} \langle S_z \rangle \right]. \quad (3.20)$$

By adding the resistivity induced by the nonmagnetic impurity X, the total resistivity can be written as

$$\rho_{xx}^\pm \approx \rho_{\text{Mn}}^* \left[1 \mp 2 \frac{J_{sd}}{V_{\text{Mn}}} \langle S_z \rangle \right] + \rho_{\text{X}}^*, \quad (3.21)$$

where ρ_{Mn}^* and ρ_X^* are not actual resistivities and we have to convert them by using $\rho_{xx}^* = \frac{\rho_{xx}^+ \rho_{xx}^-}{(\rho_{xx}^+ + \rho_{xx}^-)}$ [118]. By substituting them into Eq. (3.21), one obtains:

$$p_{yx}^{\text{AHE}} = \left[2 \left(\frac{\rho_{\text{Mn}}}{\rho_{\text{Mn}} + \rho_X} \right) \frac{J_{\text{sd}}}{V_{\text{Mn}}} \langle S_z \rangle \right] \rho_{yx}. \quad (3.22)$$

When $\mu_B \ll k_B T$, $\langle S_z \rangle = \frac{g\mu_B S(S+1)H}{3k_B T}$ (g : g-factor, μ_B : Bohr magneton, and S : the magnitude of the Mn spin) [115], ρ_{yx}^{AHE} is proportional to $1/T$, which corresponds to Eq. (3.14). By comparing Eq. (3.22) with Eq. (3.17), p can also be estimated by using the relation $J_{\text{sd}}/V_{\text{Mn}} = 0.133$ [115]. Furthermore, ρ_{yx} corresponds to the SH resistivity due to the skew scattering. In 1981, the SHE was not established, but in fact the SH resistivity was already measured in the diluted alloy systems. This has been confirmed by Niimi *et al.* recently [85].

Side jump mechanism

The side jump mechanism is one of the extrinsic mechanisms which is different from the skew scattering, as detailed below [116,117]. Smit discovered this effect when investigating the skew scattering mechanism, but he regarded it as a relatively small effect. Berger first provided the physical meaning to the side jump mechanism [117]. In the skew scattering mechanism, the trajectory of electron wave packet is bent due to the impurity potential with strong SOI and the bent angle depends on the spin direction as depicted in Fig. 3.18(a). In the side jump mechanism, on the other hand, the trajectory of electron wave packet splits into two transverse directions at the impurity center, as shown in Fig. 3.18(b). The skew scattering is an inelastic process. In other words, the momentum is not conserved in the scattering process: $k \neq k'$. On the other hand, the side jump is an elastic process where $k = k'$ is kept in the scattering process. Furthermore, the Hall conductivity obtained by this mechanism does not depend on the elastic scattering time τ unlike the skew scattering mechanism. Since there are some similarities to the intrinsic mechanism, it is difficult to experimentally distinguish between these two mechanisms, and that is the reason why the intrinsic mechanism has not been recognized for a long time.

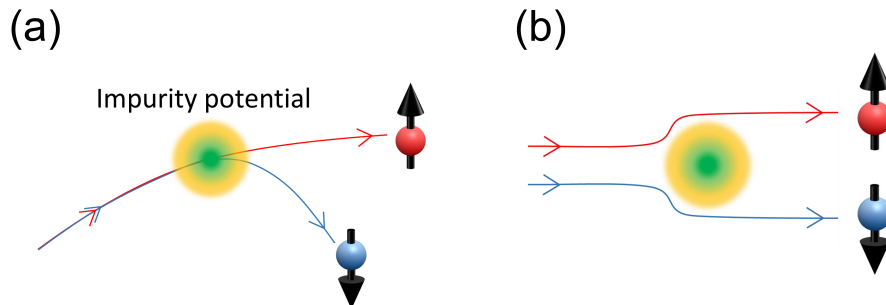


Figure 3.18: Schematic images of (a) the skew scattering mechanism and (b) the side jump mechanism.

The mechanisms of the AHE can be categorized into three contributions: the intrinsic mechanism, the extrinsic skew scattering mechanism and the extrinsic side jump mechanism. Using the resistivity language, the AHE is formulated as follows:

$$\rho_{xy}^{\text{AH}} = \rho_{xy}^{\text{AH-int}} + \rho_{xy}^{\text{AH-skew}} + \rho_{xy}^{\text{AH-sj}}, \quad (3.23)$$

where $\rho_{xy}^{\text{AH-int}} \propto \rho^2$ is the intrinsic component which can be obtained for a bulk crystal using the first principle calculations, $\rho_{xy}^{\text{AH-skew}} \propto \rho$ is the skew scattering component coming from an inelastic scattering due to impurities with strong SOI. $\rho_{xy}^{\text{AH-sj}} \propto \rho^2$ is the side jump mechanism, coming from an elastic impurity scattering. The longitudinal resistivity dependence of ρ_{xy}^{AHE} is quite similar for the intrinsic and side-jump contributions, but we note that for the extrinsic mechanisms, ρ_{yx}^{AHE} depends on the residual resistivity ρ_0 , instead of the total resistivity ρ . In other words, $\rho_{xy}^{\text{AH-skew}} \propto \rho_0$ and $\rho_{xy}^{\text{AH-sj}} \propto \rho_0^2$ [119].

3.3.3 Scaling relation

As mentioned in the previous section, the AHE can be distinguished into the intrinsic and extrinsic components. The key factor to characterize the AHE is the number of impurities and the longitudinal resistivity dependency. Onoda, Sugimoto and Nagaosa investigated the effect of impurities on the AHE and found the crossover region between the intrinsic and extrinsic mechanisms [120]. They performed numerical calculations of σ_{xy} based on the Keldysh formalism using the self-consistent T -matrix approximation. The results of theoretical curves and experimental data are shown in Fig. (3.19). In particular, there is a crossover from the predominant skew-scattering region, named “superclean limit” ($\sigma_{xy} \propto \sigma_{xx}$), to the intrinsic-dominated metallic region ($\sigma_{xy} \sim \text{const}$), named “moderately dirty metals”. The calculations also suggest another crossover to a regime, which is referred to as the incoherent regime [121], where σ_{xy} decays with the disorder following the scaling relation $\sigma_{xy} \propto \sigma_{xx}^{1.6}$. However, the physical meaning of this scaling is still controversial.

This scaling relation is universal even in the dirty limit, but some localization effects such as the Anderson localization and the weak localization are not considered in the above scaling law. If there are the localization effects, electrons can pick up additional Berry curvatures and thus the scaling does not hold.

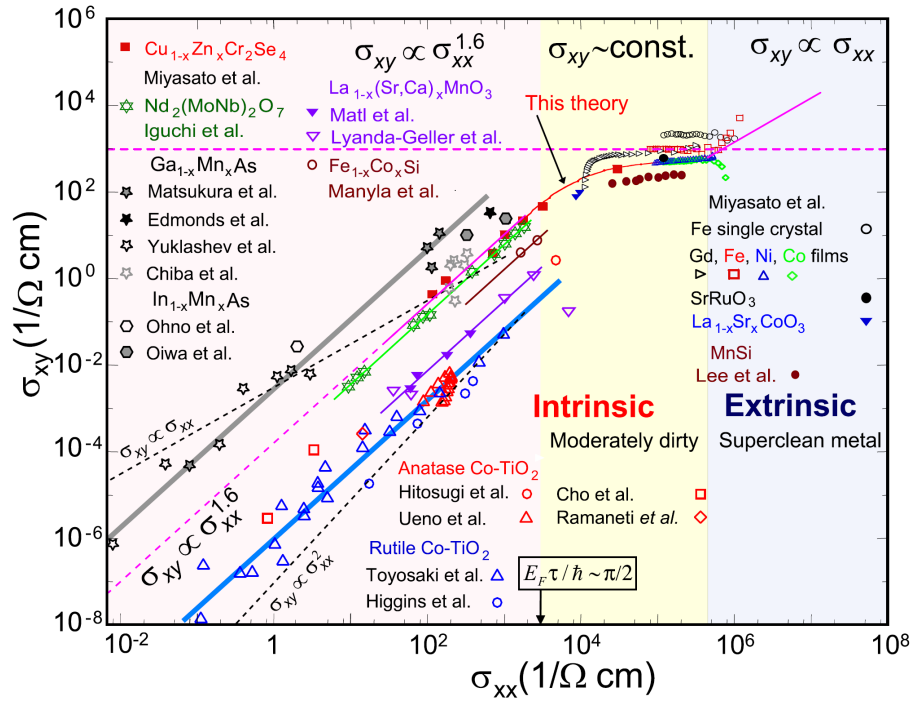


Figure 3.19: The scaling relation between σ_{xy} and σ_{xx} . Both experimental and theoretical results are superimposed on the same graph [121].

3.3.4 Relation between anomalous Hall effect and spin Hall effect

As mentioned in the previous section, the AHE originates from three distinct microscopic mechanisms: the skew scattering, the side jump, and the intrinsic mechanisms. The SHE can also be explained by these three mechanisms. However, the difference between the SHE and the AHE is that a pure spin current is not a conserved quantity, unlike the case of charge current. Therefore, in order to formulate the SHE, it is necessary to introduce a decoherence of the pure spin current [5].

For the intrinsic mechanism, a qualitative interpretation of the difference between the AHE and the SHE in a ferromagnet was reported by Zhang *et al.* [122]. They considered a double-exchange term which described itinerant s electrons interacting with local d magnetic moments. In the absence of SOC, the spins can be rotated independently of the lattice because the symmetry of the magnetic systems is higher than that contained in the magnetic space groups. In this case, the Hamiltonian is written as:

$$H = t \sum_{\langle ij \rangle \alpha} c_{i\alpha}^\dagger c_{j\alpha} - J \sum_{i\alpha\beta} (\boldsymbol{\sigma} \cdot \mathbf{n}_i)_{\alpha\beta} c_{i\alpha}^\dagger c_{i\beta}, \quad (3.24)$$

where α and β express an up-spin and a down-spin, respectively. The first term is the nearest neighbor hopping term with $\langle ij \rangle$ denoting electron numbers on nearest neighbor lattice sites. In the second term, J is the Hund's coupling strength between the conduction electron and the spin moment, $\boldsymbol{\sigma}$ is the vector of Pauli matrices, and \mathbf{n}_i is the magnetic moment on site i . Here a spin current operator $\hat{J}_\alpha^\gamma = \frac{1}{2} \{ \hat{v}_\alpha, \hat{s}_\gamma \}$ is introduced to take into account the decoherency. \hat{v}_α and \hat{s}_γ are the velocity operator and the spin operator, respectively. Thus, the SH conductivity $\sigma_{\alpha\beta}^\gamma$ and the Berry curvature $b_{n,\alpha\beta}^\gamma(\mathbf{k})$ can be calculated as:

$$\sigma_{\alpha\beta}^\gamma = \frac{e}{\hbar} \sum_n \int_{\text{BZ}} \frac{d^3\mathbf{k}}{(2\pi)^3} f_n(\mathbf{k}) b_{n,\alpha\beta}^\gamma(\mathbf{k}), \quad (3.25)$$

$$b_{n,\alpha\beta}^\gamma(\mathbf{k}) = 2i\hbar^2 \sum_{m \neq n} \frac{\langle n\mathbf{k} | \hat{J}_\alpha^\gamma | m\mathbf{k} \rangle \langle m\mathbf{k} | \hat{v}_\beta | n\mathbf{k} \rangle}{(E_{n\mathbf{k}} - E_{m\mathbf{k}})^2}, \quad (3.26)$$

where n and m are band indices, $|n\mathbf{k}\rangle$ and $E_{n\mathbf{k}}$ denote the Bloch wave functions and eigenvalues, \hat{v} is the velocity operator, and $f_n(\mathbf{k})$ is the temperature dependent Fermi-Dirac distribution. The AHE's Berry curvature $b^{\text{AHE}}(\mathbf{k})$ can be calculated by replacing the spin current operator with the velocity operator. In the following, we explain whether the AHE and the SHE become zero or remain finite, based on Fig. 3.20.

(i) AHE without SOC

In the absence of SOC, the time reversal symmetry of the system is maintained, and $\hat{v}_{\alpha\beta}$ becomes $-\hat{v}_{\alpha\beta}^\dagger$ for the time reversal operation T . Thus, the Berry curvature for the AHE becomes $b^{\text{AHE}}(\mathbf{k}) = -b^{\text{AHE}}(-\mathbf{k})$ and $\sigma_{\alpha\beta}^\gamma = 0$. In a magnetic material without SOC, the time reversal symmetry is broken by its magnetic order, but the combination

of time reversal symmetry and spin rotation symmetry (S) is maintained. The AHE does not occur in collinear magnetic materials and even in a coplanar system because the coplanar configuration has a TS symmetry. On the other hand, in a non-coplanar magnetic material, the TS symmetry is broken and the AHE appears.

(ii) SHE without SOC

In the case of the SHE, it is necessary to consider the time reversal symmetry of \hat{J}_α^γ . When there is no SOC, not only $\hat{v}_{\alpha\beta}$ but also \hat{J}_α^γ has the time reversal symmetry. For collinear magnetic materials, the SHE does not take place because an extra S symmetry exists along the z direction (see Fig. 3.20), but it appears in coplanar and non-coplanar magnetic materials even without the SOC [124,125] because the TS symmetry is naturally broken and a finite Berry curvature remains.

(iii) AHE and SHE with SOC

In case of a finite SOC, we must consider the symmetry of the spin operator in \hat{J}_α^γ . If S is a rotation around the z axis, the system has a TS symmetry for the xy plane, but the symmetry is broken along the z direction because of the SOC, and thus a Berry curvature is kept finite. Therefore, the SHE appears both in coplanar and non-coplanar magnetic configurations. This is also true for the AHE: the AHE can exist in magnetic systems which are not symmetric under time reversal combined with translational reversal (*e.g.*, conventional collinear antiferromagnet).

| | | Collinear FM | Collinear AFM | Coplanar | Noncoplanar |
|-------------|-----|--------------|---------------|----------|-------------|
| Without SOC | AHE | × | × | × | ○ |
| | SHE | × | × | ○ | ○ |
| With SOC | AHE | ○ | × | ○ | ○ |
| | SHE | ○ | ○ | ○ | ○ |

Figure 3.20: The AHE and the SHE in collinear ferromagnet, collinear antiferromagnet, coplanar, and non-coplanar magnetic lattices with and without SOC [122]. ○ and × indicate the existence and the absence of the AHE/SHE, respectively.

In the case of the extrinsic mechanism, the results of the semi-classical Boltzmann equation with the decoherence of pure spin current explain fairly well the scaling relation of the SHE [126]: $\rho_{\text{SH}} = a\rho + b\rho^2$ where the first term is the contribution of the skew scattering mechanism and the second term is that of the side jump mechanism. The scaling behavior in the SHE was experimentally confirmed by Segasta *et al.* [83]. They investigated the impurity concentration dependence of the spin Hall angle of Pt, and experimentally observed the crossover from the moderately dirty regime to the superclean regime. This fact guarantees the similarity between the SHE and the AHE.

3.4 One-dimensional Spin diffusion model

In this section, we will explain the spin injection and detection with NLSV device. As already mentioned before, the spin current is not a conserved quantity. Thus, to treat the spin current quantitatively, some well-investigated structure is needed and the NLSV device is suitable for the quantification [127].

3.4.1 Nonlocal spin valve

The NLSV device based on the lateral spin valve structure consists of two ferromagnetic wires and a nonmagnetic wire, as shown in Fig. 3.21(a). The non-magnetic wire N is connected with a ferromagnetic injector F1 and a ferromagnetic detector F2. In order to formulate spin-dependent transport in the NLSV device, we define the origin at the junction between F1 and N, and take the x - and y -axes along the N and F1 wires, respectively. The z -axis is perpendicular to the x - y plane. Figure 3.21(b) shows the three-dimensional image of a NLSV device. When a charge current is injected from F1 to N, the spin accumulation is generated between F1 and N. This spin accumulation results in a pure spin current only the right side of the N strip. Figure 3.21(c) shows the electrochemical potential in the N channel. For $0 < x < L$, j_N^\uparrow flows the $+x$ direction and j_N^\downarrow flows along the $-x$ direction. As a result, a pure spin current $j_S \equiv j^\uparrow - j^\downarrow$ flows along the $+x$ direction. The dimension (thickness t_F and width w_F) of F1 and F2 is the same and the distance between F1 and F2 is L . In general, the electric charge follows the Ohm's law, *i.e.*, $j_\sigma = \sigma_\sigma E$ where j_σ and σ_σ are the current density and the electrical conductivity for spin σ , respectively, and E is the electric field. In addition to the Ohm's law, there is an additional term, *i.e.*, a drift current which is expressed as $eD_\sigma \nabla \delta n_\sigma$. δn_σ is a deviation from the equilibrium state of charge density and D_σ is the diffusion constant. Thus, the total current is written as $j_\sigma = \sigma_\sigma E - eD_\sigma \nabla \delta n_\sigma$.

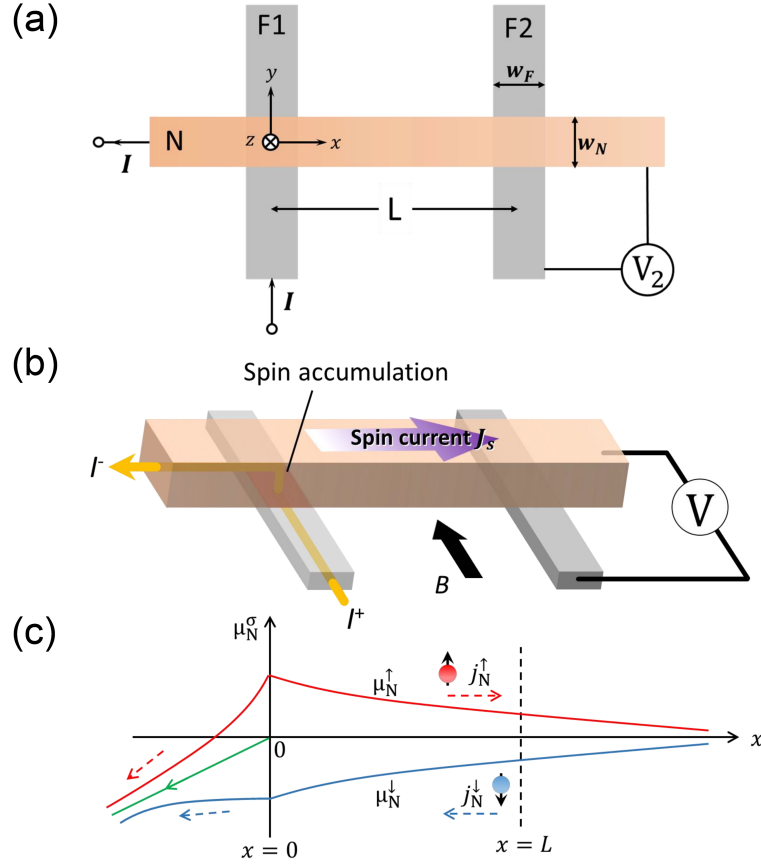


Figure 3.21: Schematic image of the NLSV device. (a) Top view, (b) the 3D illustration, and (c) the electrochemical potential distribution in the N channel. The up-spin electron flows along the $+x$ direction, while the down-spin one does along $-x$ direction. As a result, there is no charge flow but the pure spin current $j_N^\uparrow - j_N^\downarrow$ flows in the region of $x > 0$.

Here we introduce an electrochemical potential $\mu_\sigma = \epsilon_\sigma + e\phi$. By using the two equations, *i.e.*, $\delta n_\sigma = N_\sigma \delta \epsilon_\sigma$ and $\sigma_\sigma = e^2 N_\sigma D_\sigma$ (N_σ : the density of state for spin σ and $\delta \epsilon_\sigma$: an energy deviation from the Fermi energy), the total current density j_σ can be represented as $j_\sigma = -(\frac{\sigma_\sigma}{e} \nabla \mu_\sigma)$. Thus, the continuous equations for charge and spin currents in a steady state can be written as:

$$\nabla \cdot (\mathbf{j}_\uparrow + \mathbf{j}_\downarrow) = 0 \quad (3.27)$$

$$\nabla \cdot (\mathbf{j}_\uparrow - \mathbf{j}_\downarrow) = -\frac{e\delta n_\uparrow}{\tau_{\uparrow\downarrow}} + \frac{e\delta n_\downarrow}{\tau_{\downarrow\uparrow}} \quad (3.28)$$

where $\tau_{\sigma\sigma'}$ is the spin scattering time from σ to σ' . By using Eqs. (3.27) and (3.28) as well as detailed balancing $\frac{N_\uparrow}{\tau_{\uparrow\downarrow}} = \frac{N_\downarrow}{\tau_{\downarrow\uparrow}}$, the following differential equations can be obtained:

$$\nabla^2(\sigma_\uparrow \mu_\uparrow + \sigma_\downarrow \mu_\downarrow) = 0 \quad (3.29)$$

$$\nabla^2(\mu_{\uparrow} - \mu_{\downarrow}) = \lambda^{-2}(\mu_{\uparrow} - \mu_{\downarrow}) \quad (3.30)$$

where the SDL λ is derived from $\lambda = \sqrt{D\tau_{\text{sf}}}$, $\tau_{\text{sf}}^{-1} = \frac{1}{2}(\tau_{\uparrow\downarrow}^{-1} + \tau_{\downarrow\uparrow}^{-1})$, and $D^{-1} = \frac{N_{\uparrow}D_{\downarrow}^{-1} + N_{\downarrow}D_{\uparrow}^{-1}}{N_{\uparrow} + N_{\downarrow}}$.

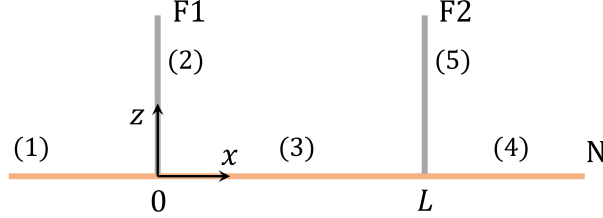


Figure 3.22: 5 different segments to calculate the electrochemical potential using the 1D spin diffusion model.

To calculate the electrochemical potentials and the current densities for up-spin and down-spin using Eqs. (3.29) and (3.30), we divide the NLSV device into 5 parts as shown in Fig. 3.22. By considering the boundary conditions at all the junctions, the spin accumulation between F2 and N can be obtained as follows: The spin accumulation is represented as:

$$\mathcal{R}_s \equiv \frac{V_2}{I} = \frac{2p_F^2 R_N e^{-\frac{L}{\lambda_N}}}{\left(\frac{R_N}{R_F} + 2\right)^2 - \left(\frac{R_N}{R_F}\right)^2 e^{-\frac{2L}{\lambda_N}}} \quad (3.31)$$

where p_F is the spin polarization and R_X ($X = N, F$) is the spin resistance defined as $R_X \equiv \frac{\lambda_X}{\sigma_X A_X}$ and A_X is the cross-section area. In an actual device, we measure the spin signal, that is $\Delta R \equiv \frac{2V_2}{I}$ as shown in Fig. 3.23

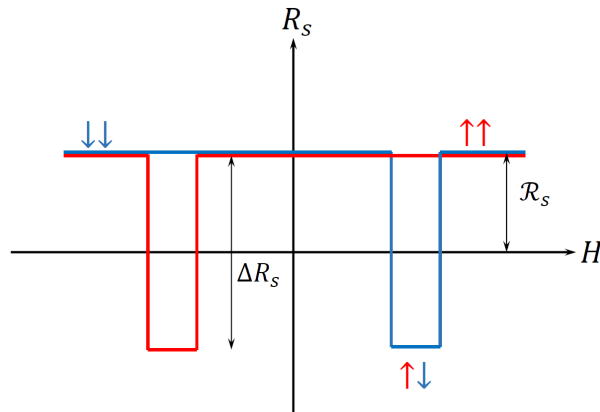


Figure 3.23: Spin signal ΔR expected in the NLSV device. The arrows in the figure indicate the magnetization directions of F1 and F2.

3.4.2 Nonlocal spin valve with a middle wire

In order to estimate the SDL and the SH angle of strong spin orbit material, the target strong SO material is placed between the F1 and F2 wires (see Fig. 3.24). As already discussed in the previous subsection, the pure spin current generated at the F1/N interface is absorbed perpendicularly to the M wire because of its stronger spin orbit interaction. By comparing NLSV signals with and without the M wire, we can estimate how much of the pure spin currents generated at the F1/N interface is absorbed into the M wire.

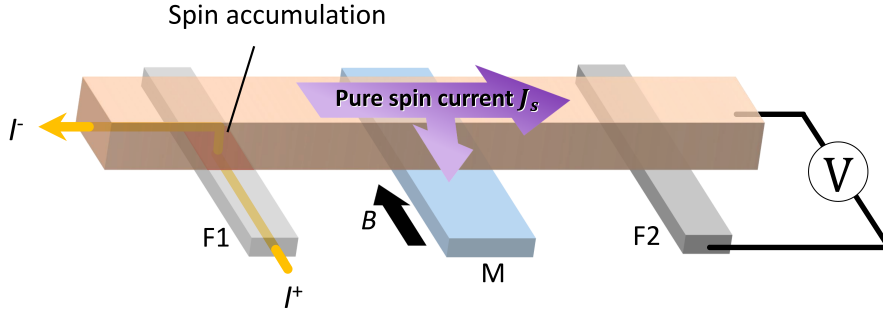


Figure 3.24: The NLSV device with a middle wire.

Although we omit the detailed calculation process, the following formula can be obtained by following the same calculation procedure as in the previous section.

$$\Delta\mathcal{R}_s^{\text{with}} = \frac{4p_F^2 Q_F^2 Q_M R_N}{\cosh\left(\frac{L}{\lambda_N}\right) - 1 + 2Q_M \sinh\left(\frac{L}{\lambda_N}\right) + 2Q_F \{e^{\frac{L}{\lambda_N}}(1 + Q_F)(1 + 2Q_M) - 1\}} \quad (3.32)$$

$$\eta \equiv \frac{\Delta\mathcal{R}_s^{\text{with}}}{\Delta\mathcal{R}_s^{\text{without}}} = \frac{2Q_M \left\{ \sinh\left(\frac{L}{\lambda_N}\right) + 2Q_F e^{\frac{L}{\lambda_N}} + 2Q_F^2 e^{\frac{L}{\lambda_N}} \right\}}{\cosh\left(\frac{L}{\lambda_N}\right) - 1 + 2Q_M \sinh\left(\frac{L}{\lambda_N}\right) + 2Q_F \{e^{\frac{L}{\lambda_N}}(1 + Q_F)(1 + 2Q_M) - 1\}} \quad (3.33)$$

where $Q_X = \frac{\mathcal{R}_S^X}{\mathcal{R}_S^N}$ ($X = M, F$). We note that Eq. (3.32) includes only one fitting parameter, *i.e.*, λ_M . It means that the spin diffusion length of M, λ_M can be estimated by measuring $\Delta\mathcal{R}_s^{\text{with}}$ and $\Delta\mathcal{R}_s^{\text{without}}$.

3.4.3 Spin Hall measurement using Spin Absorption Method

In case of the ordinary Hall effect, the Hall angle is determined by the Ohm's law:

$$\mathbf{E} = \rho \mathbf{j} = \begin{pmatrix} \rho_{xx} & -\rho_{yx} \\ \rho_{yx} & \rho_{yy} \end{pmatrix} \begin{pmatrix} j_x \\ j_y \end{pmatrix} = \begin{pmatrix} E_x \\ E_y \end{pmatrix}. \quad (3.34)$$

Thus, the Hall angle is defined as $\alpha_H \equiv \frac{E_y}{E_x} = \frac{\rho_{yx}}{\rho_{xx}}$ as an analogy of the Hall angle. Before discussion about the SH angle obtained in the spin absorption method, let us first consider the SH angle in the Hall cross device (Fig. 3.25).

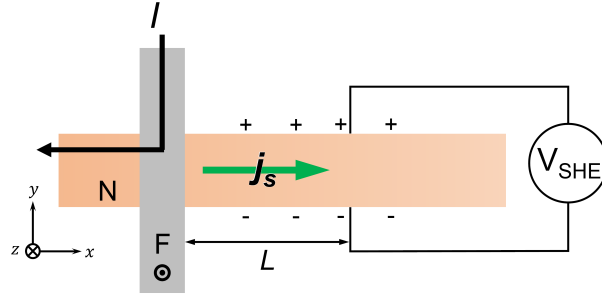


Figure 3.25: Schematic image of a typical Hall cross device.

The Hall cross device consists of a ferromagnetic wire F and a nonmagnetic wire N. When a charge current is injected from F to N, spin accumulation is generated between F and N. This spin accumulation induces a pure spin current only on the right side of the N strip. When the magnetization of F is along to the z -axis, the spin accumulation is generated at the edges of the N wire due to the SHE in the N wire. In case of the SHE, a transverse electrical field is $E_y = -\rho_{yx}j_s$ and $E_H = \rho_H j_s$ where $\rho_{yx} \equiv \rho_H$ (or ρ_{SHE}). According to the 1D spin diffusion model, \mathbf{j}_s and R_{SHE} can be written as

$$\mathbf{j}_s = \frac{\mathbf{I}_s}{w_N t_N} = \rho_H \frac{I Q_F p_F e^{-\frac{L}{\lambda_N}}}{w_N t_N (2Q_F + 1)} \quad (3.35)$$

$$R_{SHE} = \rho_H \frac{I Q_F p_F e^{-\frac{L}{\lambda_N}}}{t_N (2Q_F + 1)} \quad (3.36)$$

where w_N is the width of N wire and t_N is the thickness of N wire.

Next, we explain the ISHE in the spin absorption device. Figure 3.26(a) is the top image of the device. It consists of an F wire, a strong spin-orbit material M wire bridged by a N bridge. When the magnetic field is applied to along the x -axis, the absorbed pure spin current is converted to the charge current due to the ISHE. In case of the ISHE using the spin absorption method, the pure spin current must be treated as an average value along the thickness direction of the M wire because j_s exponentially decays (Fig. 3.26(b)).

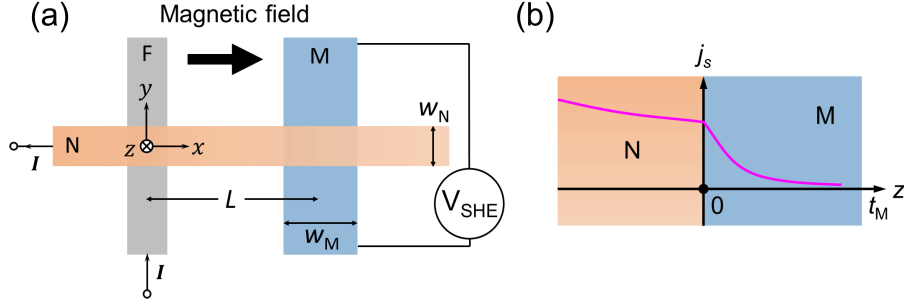


Figure 3.26: (a) The top view of the spin Hall device. (b) The cross-sectional image at the interface between N and M.

The averaged spin current density \bar{j}_s is expressed as $\bar{j}_s = \frac{1}{t_M} \int_0^{t_M} dz j_s$. Thus, the averaged spin current \bar{I}_s is obtained by multiplying \bar{j}_s by the sample dimension [85]:

$$\begin{aligned} \frac{\bar{I}_s}{I_C} &= \frac{\int_0^{t_M} dz j_s}{t_M} = \frac{\lambda_M (1 - e^{-\frac{t_M}{\lambda_N}})^2}{t_M (1 - e^{-\frac{2t_M}{\lambda_N}})} \times I_s(z=0) \\ &\approx \frac{\lambda_M (1 - e^{-\frac{t_M}{\lambda_N}})^2}{t_M (1 - e^{-\frac{2t_M}{\lambda_N}})} \\ &\times \frac{2p_F I_C Q_F \sinh(L/2\lambda_N) + Q_F \exp(L/2\lambda_N)}{\cosh(L/\lambda_N) - 1 + 2Q_M \sinh(L/\lambda_N) + 2Q_F \exp(L/\lambda_N)(1 + Q_F)(1 + 2Q_M) - 1}. \end{aligned} \quad (3.37)$$

By using the relation $V_{\text{SHE}} = w_N E_{yx}$, $E_{yx} = \rho_{\text{SHE}} \bar{j}_s = \rho_{\text{SHE}} \frac{\bar{I}_s}{w_N w_M}$, the SH angle can be written as:

$$\alpha_H \equiv \frac{w_M V_{\text{SHE}}}{\rho_M \bar{I}_s}. \quad (3.38)$$

In the actual device, it is necessary to correct the shunting effect when N is connected to the surface of the M wire (Fig. 3.27). This correction factor x was obtained from the additional experiment and found to be $x \approx 0.36$ for $t_M = 20$ nm [85]. It is an essential issue because this value is not negligible and also depends on the resistivities of N and M.

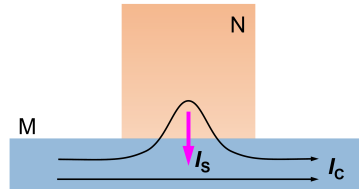


Figure 3.27: Schematic image of the interface between N and M. The pink arrow indicates the pure spin current, which is converted to the charge current due to the ISHE. The black arrows indicate the charge current pass.

Chapter 4

Purpose of this thesis

As described above, frustrated magnetic materials have attracted much attention because of their unique magnetic states and dynamics caused by spin frustrations, and have been studied intensively using magnetization, heat capacity, neutron scattering, NMR, ESR, and so on. However, since those are so complex, another experimental method is desirable to unveil the complex system.

Here we focus on spin transport measurements as detailed in Chapter 3. Especially, it has been revealed that the SH angle is strongly affected by magnetic fluctuations near the magnetic transition temperature of nanoscale magnets. This fact indicates that the spin transport measurements can be a useful method to elucidate the magnetic dynamics of nanoscale magnets.

In this work, we have aimed to study the magnetic dynamics of nanoscale frustrated magnet from the viewpoint of electric and spin conductivity. For this purpose, we chose two types of frustrated magnetic materials: ternary alloy spin glass CuMnBi and triangular lattice antiferromagnet Ag_2CrO_2 .

In spin glasses, according to the previous report of SHEs in spin-glass nanowires, little is known about the quantitative relation between spin-glass dynamics and the SHE. Furthermore, the physical picture of SHE in the spin-glass phase still has not been clear yet. In order to elucidate it, we have prepared CuMnBi alloys whose Mn concentrations are one order higher than the previous work and aimed to investigate the quantitative relation between spin glasses and the SHE.

In triangular antiferromagnet Ag_2CrO_2 , the PD cite should be treated as a paramagnetic spin as detailed in Chapter 2, but there is a finite magnetic moment. This mystery has not been solved yet because all the experiments mentioned in Chapter 2 were performed with polycrystalline samples. In this study, we have aimed to establish a nanofabrication technique to extract a single crystal thin film from the polycrystalline sample and to elucidate the physical properties of Ag_2CrO_2 from the viewpoint of electrical conductivity.

Part III

Experimental results

Chapter 5

Experimental setup

In this chapter, we explain the fabrication process of NLSV devices with a spin-glass middle wire and show some experimental results on reference devices, *i.e.*, NSLV devices without the middle wire. The fabrication process is relatively complicated and there are many notes with the fabrication procedures. Those are detailed in the following section.

5.1 Nanofabrication method

5.1.1 Lift off method

Originally, “lithography” means a method of printing. If limited to electronic devices, it is a method of fabricating patterns on various substrates and is an indispensable technology for today’s electronics based on semiconductor integrated circuits such as large-scale integrated circuits (LSI). In general lithography, a photosensitive organic material (resist) is uniformly put on a substrate and irradiated with ultraviolet rays or an electron beam. After that, the resist is denatured and treated with an appropriate solvent (developer) to produce a mask (protective film) and to design the pattern. We use different kinds of resists. For the photolithography, we use S1813G (SHIPLEY Co. Ltd.). For the electron beam (EB) lithography, we use polymethyl-methacrylate (PMMA, molecular weight 950A4, Microchem Co.Ltd.) or ZEP520A (ZEON Co. Ltd.). We use the two EB resists, depending on the evaporation method: the former is used for the EB evaporation or Joule heating evaporation, while the latter is used for the Ar sputtering. The typical parameters for fabricating nanoscale patterns are listed in Table 5.1.

Table 5.1: List of some parameters for different kinds of resists.

| Resist | Rotational speed (rpm) | Thickness | Dose |
|-----------|------------------------|-----------|--------------------------------|
| S1813G | 5000 | 1200 nm | Mercury lamp 30 sec. |
| PMMA | 3000 | 240 nm | 860 $\mu\text{C}/\text{cm}^2$ |
| PMMA/PMMA | 3000 | 480 nm | 1000 $\mu\text{C}/\text{cm}^2$ |
| ZEP/PMMA | 4000/5000 | 570 nm | 900 $\mu\text{C}/\text{cm}^2$ |
| ZEP | 4000 | 350 nm | 220 $\mu\text{C}/\text{cm}^2$ |

Note that while treating resists, we have to pay attention to the environment because the resists are easy to degrade by the humidity. Photolithography is used for large patterns with a single exposure, but is not suitable for patterns on nanometer scale. On the other hand, EB lithography is used for highly accurate patterns with a resolution of several 10 nm, but enormous time is required to draw a large area. Therefore, we need to choose a proper method, depending on the situation: for instance, the former is often used when a large area pattern is required, and the latter is often used when a precise pattern is required. In this thesis, we use the so-called lift-off method where (1) materials are deposited by EB evaporation, Joule heating evaporation, or Ar sputtering on the substrate with resist, (2) only desired patterns are left on the substrate and (3) any other unnecessary parts are removed after dipping the substrate in a proper solvent (Fig. 5.1).

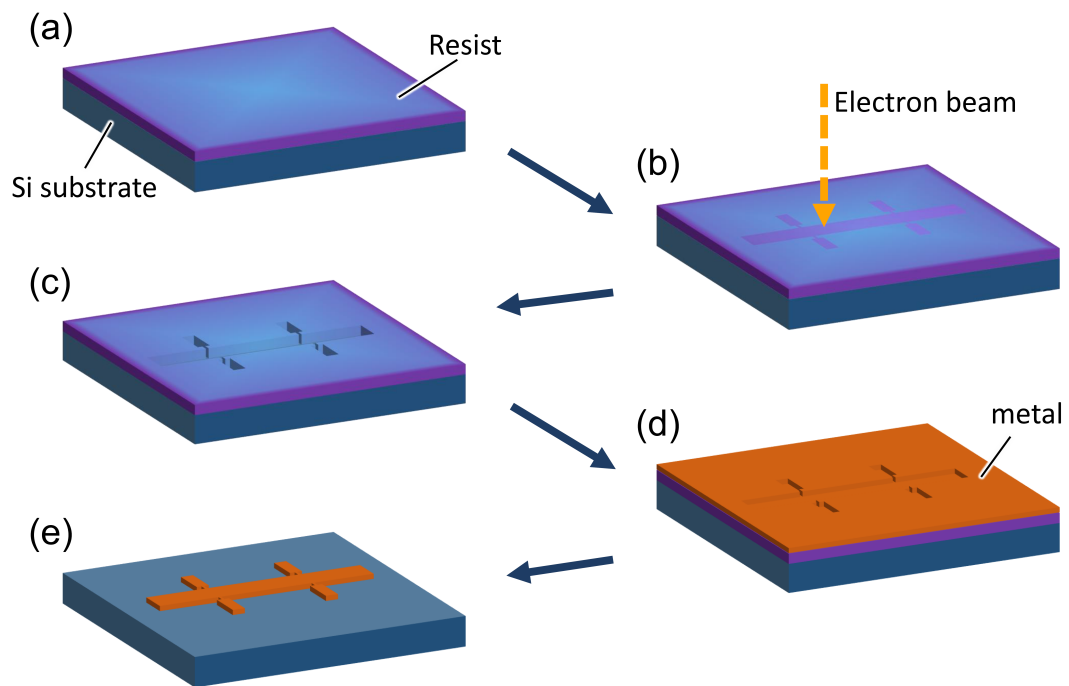


Figure 5.1: Schematic images of lift-off process. (a) Cover a resist on a Si substrate. (b) Exposure an electron beam (or an ultraviolet light) on the resist. (c) Remove the denatured resist by a developer. (d) Deposit a metal film. (e) Remove the extra metal by using a proper solvent.

5.1.2 Evaporation methods of thin films

In this subsection, we introduce different evaporation methods, depending on the situation.

Joule heating evaporation

The Joule heating evaporation is the easiest method to evaporate a target metal on a high melting temperature metal boat such as tungsten or molybdenum (Fig. 5.2(a)). The boat is heated up by passing a large current to the resistive boat (that is why this method is called “the Joule heating”). Since the melting temperature of the target material is much lower than that of the boat, the target material is melt and evaporated in a vacuum chamber. There is an advantage that any contaminations from the boat to the target are avoided. On the other hand, there are some disadvantages that (1) only low melting materials such as Au, Ag, Cu can be handled: it is difficult to handle high melting temperature materials such as Pt, Ta, W, (2) most of magnetic materials cannot be deposited by this method since those make alloys with the boat, (3) alloys cannot also be deposited by this method because the melting temperatures of composing elements are sometimes quite different and thus it is difficult to keep the same composition ratio as the original target.

Electron beam evaporation

The electron beam (EB) evaporation is a method to heat a target placed in a crucible by irradiating the EB to the target (Fig. 5.2(b)). To heat the target locally, the EB is focused on a small part of the target by applying a high voltage and a magnetic field, while the crucible is always kept cool by flowing water from the outside of the vacuum chamber. Contrary to the Joule heating evaporation, magnetic materials and also high melting temperature materials can be deposited by this method. On the other hand, even this technique, it is difficult to deposit alloys such as spin-glass materials, keeping the same composition ratio as the original one. As a crucible material, we use a copper or carbon hearth liner.

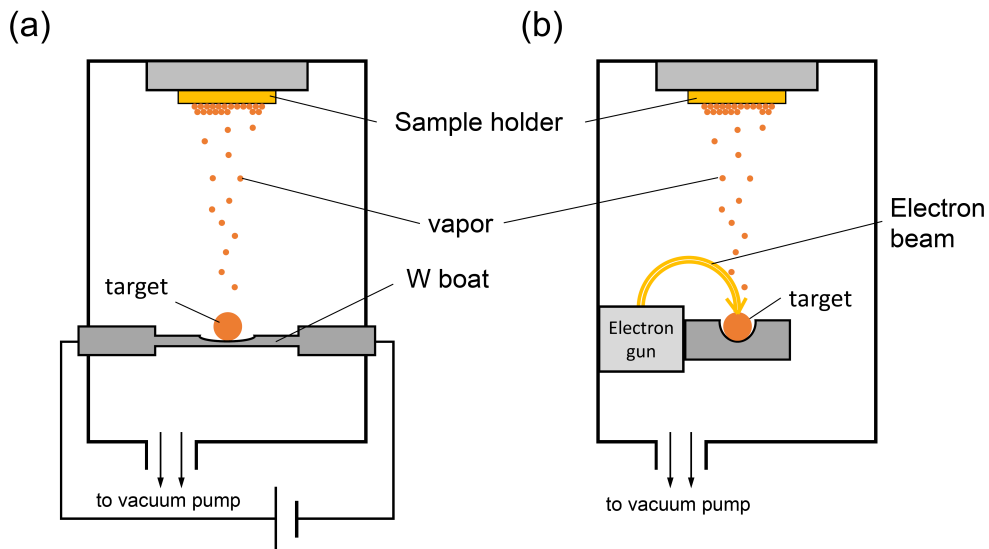


Figure 5.2: Schematic images of (a) Joule heating evaporation and (b) electron beam evaporation. The electron beam is emitted from the electron gun, bent by the magnetic field, and hits the target to avoid the contamination of the gun.

Ar sputtering method

To deposit insulating materials and also alloys, the Ar sputtering is a quite useful method. When an inert gas such as Ar is accelerated and bombarded to the surface of target material at high speed, the constituent atoms and molecules are flied away in vacuum and deposited on the substrate (Fig. 5.3(a)). Since the deposited atoms and molecules have a higher energy than those evaporated by the Joule heating and the EB methods, they have a stronger adhesion to the substrate. There is another advantage that the deposited composition ratio is almost the same as the original target. On the other hand, the purity of the deposited film is worth than that of the vapor deposition method.

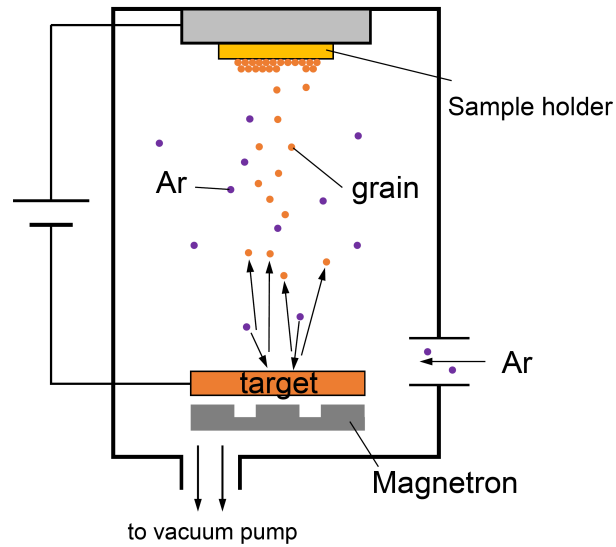


Figure 5.3: Schematic images of the magnetron sputtering system. The magnetron makes the plasma density increase.

5.1.3 Fabrication of nonlocal spin valve device

Our SH device is based on the LSV structure with a strong spin-orbit material in the middle, which allows us to inject a spin current into the middle wire, as shown in Fig. 5.4. In this section, we explain the fabrication procedure of our SH devices.

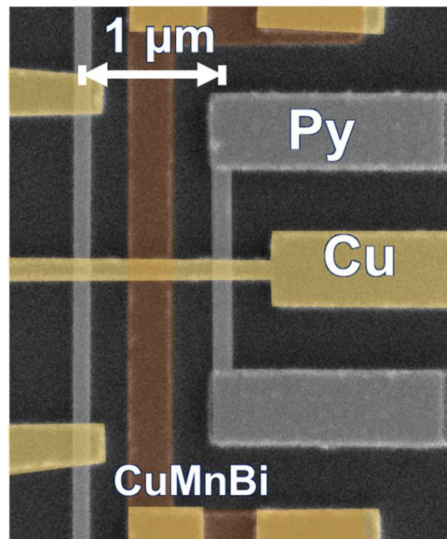


Figure 5.4: The scanning electron micrograph of a typical SH device.

Large electrodes

1. Cut a SiO₂/Si substrate into 30 mm square and clean it by a ultrasonic cleaner with acetone for 3 minutes.
2. Clean the substrate by using ozone ashing for 3 minutes at 90 °C with the oxygen flow rate of 0.5 l/min.
3. Turn on the yellow light in the experimental room to avoid the degradation of resist.
4. Put the Si substrate on a spin coater and coat the S1813G resist at a rotation speed of 1000 rpm for 5 seconds with a 5 second slope¹, and 4000 rpm for 40 seconds.
5. Bake the substrate on a hot plate at 120 °C for 10 minutes to remove moisture on the surface of the substrate.
6. Set a pattern mask on the mask aligner, and the Si substrate with the resist is exposed to a mercury lamp for 30 seconds.
7. Develop with MF319 for 30 seconds and rinse with pure water for 30 seconds to remove the residual developer.
8. Deposit Ti by 5 nm and Au by 100 nm using an EB evaporation.
9. Before the lift-off process, bake the substrate on a hot plate at 120 °C for 10 min.
10. After dipping it in acetone at 60 °C, the lift-off process is performed using a dropper.

Small electrodes

1. Coat the PMMA950A4 resist at a speed of 3000 rpm for 60 seconds with a 5-second slope.
2. Bake the substrate on a hot plate at 120 °C for 10 minutes.
3. Draw fine electrodes and cross marks using the EB lithography. This cross mark is used for further pattern drawings using the EB lithography.
4. Develop the patterns with a PMMA developer (isopropyl alcohol (IPA): methyl isobutyl ketone (MIBK) = 3: 1) for 30 seconds and rinse with IPA for 30 seconds.
5. Post-bake the substrate for 4 minutes on a hot plate at 100 °C to remove the developer and rinse solution remaining on the substrate.
6. Deposit Ti by 5 nm and Au by 100 nm using an EB evaporation.
7. After dipping it in acetone at 60 °C, the lift-off process is performed using a dropper.

¹The slope time affects the height of the resist peak formed at the edge of the substrate. With shorting the slope time, the height of edge peak becomes lower.

Middle wire

The EB evaporation and Joule heating evaporation are not suitable for multi-component alloys such as CuMnBi. We used a *dc* magnetron sputtering equipment for deposition of the alloys. However, the resist may be denatured by the argon plasma during sputtering. Therefore, one should choose a resist tolerant of Ar plasma. In this work, we used PMMA resist, ZEP resist or ZEP/PMMA bilayer resist².

PMMA

1. Coat the PMMA950A4 resist at a speed of 3000 rpm for 60 seconds with a 5-second slope.
2. Bake the substrate on a hot plate at 120 °C for 10 minutes.
3. Draw patterns by an electron beam lithography.
4. Develop the patterns with a PMMA developer for 30 seconds and rinse with IPA for 30 seconds.
5. Post-bake the substrate for 4 minutes on a hot plate at 100 °C.

ZEP

1. Coat the ZEP520A resist 4000 rpm for 60 seconds with a 5-seconds slope.
2. Place the substrate on a hot plate at room temperature and heat the hot plate up to 180 °C for 6 minutes.
3. Draw patterns by an electron beam lithography.
4. Develop the patterns with n-pentyl acetate for 30 seconds and rinse with ZEP rinse solution (IPA: 4M2P = 1: 9) for 30 seconds, and second rinse with IPA for 20 seconds.
5. Post-bake the substrate for 4 minutes on a hot plate at 140 °C.

ZEP/PMMA

1. Coat the PMMA950A4 resist at a speed of 5000 rpm for 60 seconds with a 5-second slope.
2. Bake the substrate on a hot plate at 120 °C for 10 minutes.
3. Coat the ZEP520A resist at a speed of 4000 rpm for 60 seconds with a 5-second slope.

²Since ZEP resist is particularly sensitive to the humidity, PMMA was used during the summer or on a raining day. The ZEP/PMMA bilayer resist may be useful when you deposit thick (~100 nm) electrodes by an Ar sputtering system.

4. Place the substrate on a hot plate at room temperature and heat the hot plate up to 180 °C for 6 minutes.
5. Draw patterns by an electron beam lithography.
6. Develop with n-pentyl acetate for 30 seconds, rinse with ZEP rinse solution for 30 seconds, and second with IPA for 20 seconds.
7. Post-bake the substrate for 4 minutes on a hot plate at 140 °C.

Hereafter, the above resist conditions are used unless noted. After fabricating resist patterns, deposit a multi-component alloys by Ar sputtering process. Next, we show the procedure to deposit the alloys and the lift-off process.

1. Before set the substrate on a sample holder, pre-deposit the alloys on the sample holder to avoid the contamination.
2. Deposit the alloy with Ar atmosphere (vacuum level is 0.70 Pa) and the sputtering power is 50 W³.
3. After dipping it in 1-methyl 2-pyrrolidone (1M2P) at 60 °C, the lift-off process is performed using a dropper.
4. Rinse with acetone at 60 °C for 30 seconds to remove the 1M2P.

Especially, when we use the PMMA resist, some burrs are formed at the edges of the patterns because of the Ar sputtering. To remove the burrs, we use an ultrasonic cleaner with 1M2P for a few seconds.

Py wire

1. Coat the PMMA950A4 resist at a speed of 5000 rpm for 60 seconds with a 5-second slope.
2. The fabricating pattern process is the same as the PMMA condition for middle wire.
3. Deposit a 30 nm thick Py by using the electron beam evaporation.
4. After dipping it in acetone at 60 °C for 10 min, the lift-off process is performed using a dropper.

³The deposition rate is proportional to the sputtering power.

Cu bridge

1. Coat the PMMA950A4 resist at a speed of 3000 rpm for 60 seconds with a 5-second slope.
2. The fabricating pattern process is the same as that for Py wire. Before the deposition of Cu, perform an Ar milling to remove the oxidized layers. The schematic image of the Ar milling is shown in Fig. 5.5. The Ar milling was performed under the Ar atmosphere with the Ar flow rate of 1.0 sccm⁴. The parameters of the milling process are Beam: 600 V, 12 mA, Accelerator: 400 V and the milling time is 55 seconds.

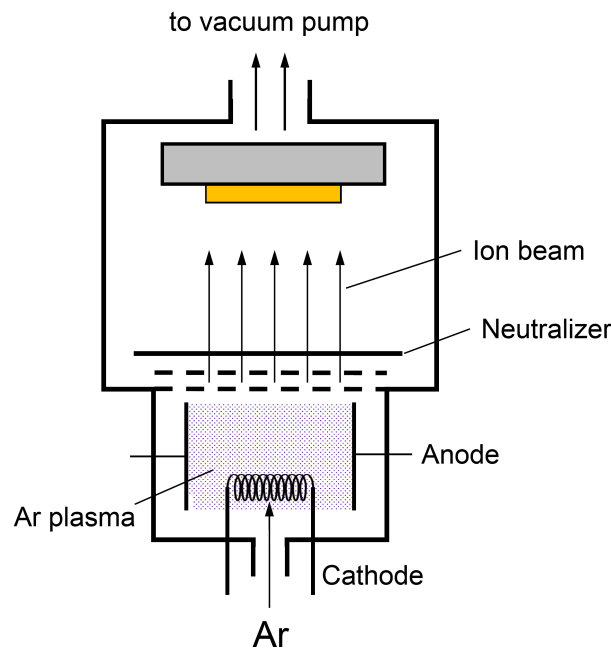


Figure 5.5: The schematic image of the Ar milling system. The cathode and anode at the bottom part generate an Ar plasma. The generated plasma is neutralized at the neutralizer and bombarded to the sample.

3. Deposit a thick 100 nm Cu by using a Joule heating evaporation. During the deposition of Cu, we use a liquid nitrogen trap to remove moisture in the chamber using liquid nitrogen.
4. After dipping it in acetone for a night, the lift-off process is performed using a dropper at 60 °C.

⁴Standard Cubic Centimeter per Minute

5.1.4 Measurement setup

To perform electrical and spin transport measurements in a wide temperature range, we use a ^4He flow cryostat with an electromagnet, as shown in Fig. 5.6(a). The prepared device is mounted on a chip carrier at the bottom of a dip stick. By pumping the He line with a rotary pump, cold He gas flows in the cryostat and thus the device is cooled down from room temperature to $T = 1.5$ K. The magnetic field can be applied to the device in the range of ± 1.2 T. The electrical measurements are performed by the standard lock-in technique as shown in Fig. 5.6(b).

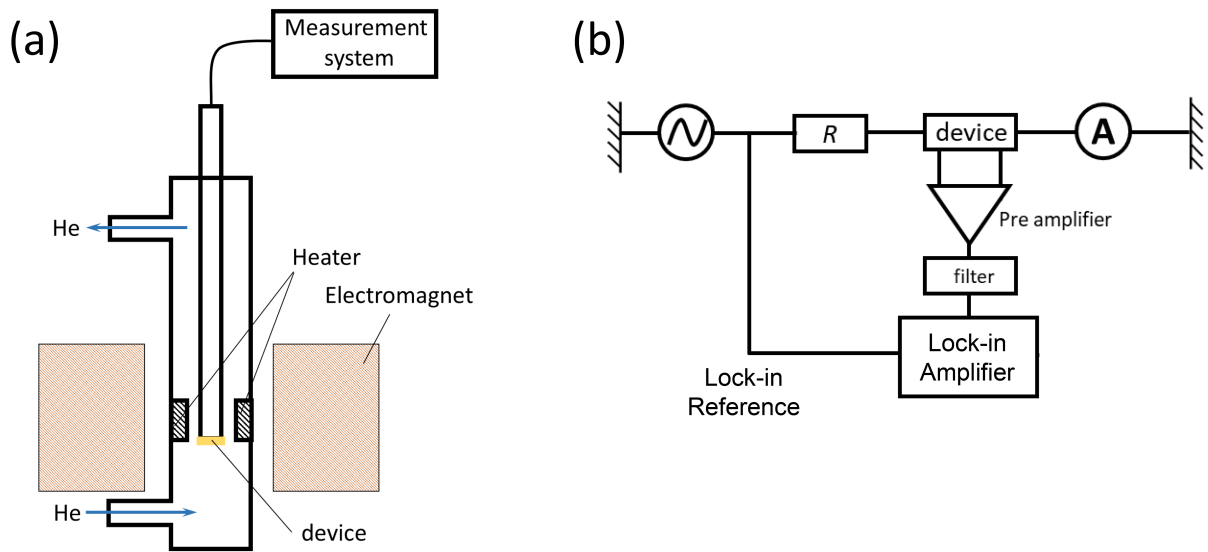


Figure 5.6: Schematic drawings of (a) our cryostat with an electromagnet and (b) the measurement circuit for the standard lock-in method.

5.2 Nonlocal spin valve measurements without middle wire

To characterize the SHE in a middle wire measured with the spin absorption method in the LSV structure, we need to obtain some important parameters about ferromagnets (F) and non-magnetic (N) wire bridge. For this purpose, we first measured NLSV without the middle wire. As mentioned in subsection 2.3.1, spin accumulation in the 1D spin diffusion model can be written as:

$$\mathcal{R}_s = \frac{2p_F^2 R_N e^{-\frac{L}{\lambda_N}}}{\left(\frac{R_N}{R_F} + 2\right)^2 - \left(\frac{R_N}{R_F}\right)^2 e^{-\frac{2L}{\lambda_N}}}, \quad (5.1)$$

where R_X ($X = N, F$) is a spin resistance defined as $R_X = \frac{\lambda_X}{\sigma_X A_X (1 - p_X^2)}$. A_X is the area of cross section and p_X is a spin polarization of the material. When the device dimension is fixed, parameters which determine ΔR_S are the spin diffusion lengths of Py (λ_{Py}) and Cu (λ_{Cu}) and the spin polarization of Py (p_F). λ_{Py} and λ_{Cu} depends on the quality of the materials and p_F depends on the quality of the interface between Py and Cu⁵.

The inset of Fig. 5.7(a) shows the SEM image of our NLSV device. When a charge current flows from the upper Py wire to the Cu bridge, spin accumulation is generated at the interface between Py and Cu. The generated spin accumulation induces the spin current in the Cu strip. When another Py detector is attached to the Cu strip, a finite nonlocal voltage is generated and changes the sign, depending on the magnetic configuration of the two ferromagnets.

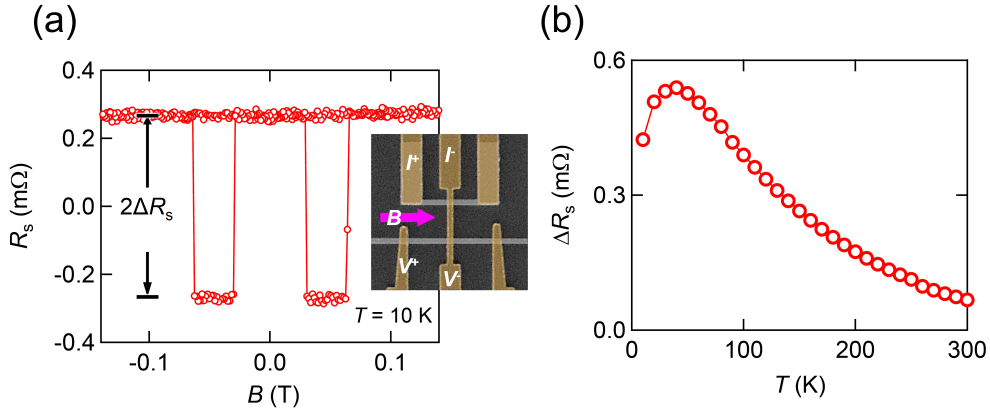


Figure 5.7: (a) A typical spin signal at 10 K. The inset shows the SEM image of the NLSV device. (b) Temperature dependence of ΔR_S .

In Fig. 5.7(a), we show a typical spin accumulation signal (or we simply call “spin signal”) of our device. The nonlocal voltage divided by the injection current, *i.e.*, R_S changes the sign, depending on the parallel (P) and antiparallel (AP) states of the two

⁵The quality of the interface depends on its roughness or the number of impurities.

Py wires. The switching field is 0.05 T. This field is determined by the dimension and configuration of the Py wires. We defined ΔR_S as show in Fig. 5.7(a). The temperature dependence of ΔR_S is plotted in Fig. 5.7(b). ΔR_S takes a maximum at $T = 40$ K and decreases with increasing the temperature. The reduction of ΔR_S at $T > 40$ K is due to the spin relaxation induced by the electron-phonon scattering in the Cu wire. According to the Elliott-Yafet mechanism [128–130], ΔR_S should monotonically increase with decreasing temperature and takes a constant value at low temperatures where there are much less phonons. Below $T = 40$ K, however, ΔR_S decreases again. Such a reduction was reported several groups [131–133]. So far, some scenarios have been proposed: oxidation [131], Kondo alloys [132], and spin reabsorption [133] at the interface between F and N, but the origin of the reduction has not been elucidated yet. At least, our experimental results are consistent with the previous reports.

Figure 5.8 shows ΔR_S^{MAX} (measured at $T = 40$ K) as a function of the resistivity of Py measured at $T = 300$ K (a) and as a function of the residual resistivity ratio (RRR) of Cu (b).

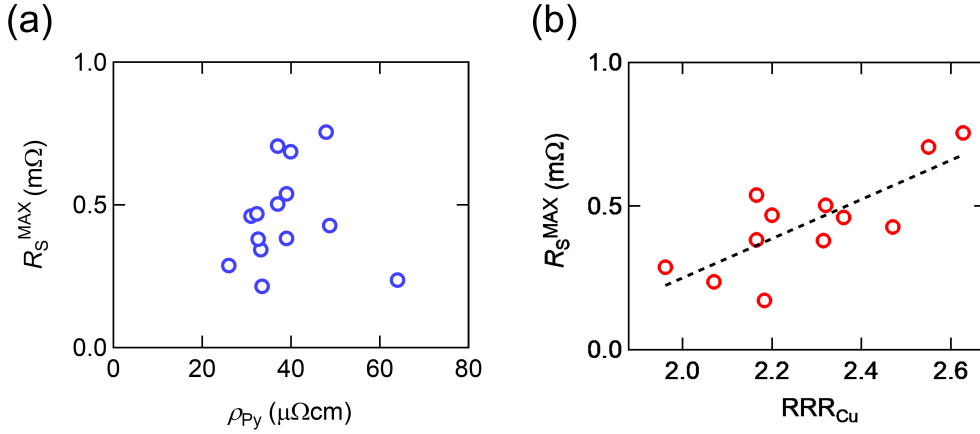


Figure 5.8: (a) The Py resistivity dependence of ΔR_S . (b) ΔR_S as a function of the RRR of Cu. The broken line is a guide for the eye.

It seems that there is no relation between ρ_{Py} and ΔR_S (Fig. 5.8(a)). Although ρ_{Py} at $T = 300$ K has a distribution from 22 to 62 μΩcm, the RRR value is almost constant (~ 1.5). On the other hand, there is a clear relation between ΔR_S and the RRR of Cu (Fig. 5.8(b)). This fact indicates that the amplitude of ΔR_S strongly depends on the number of impurities in Cu. To reduce the impurities, we used 99.9999 % Cu for the target. In addition, during the deposition of Cu, we used a cryopump with liquid N₂ to remove H₂O in the vacuum chamber. As a result, we can obtain a high-quality Cu (RRR $\sim 2.5^6$).

The quantitative analysis of the interface is difficult, but the interface can be evaluated with the measurement setup shown in Fig. 5.9.

⁶In our experience, the RRR of Cu changes by a factor of 1.5 with using and without the cryopump.

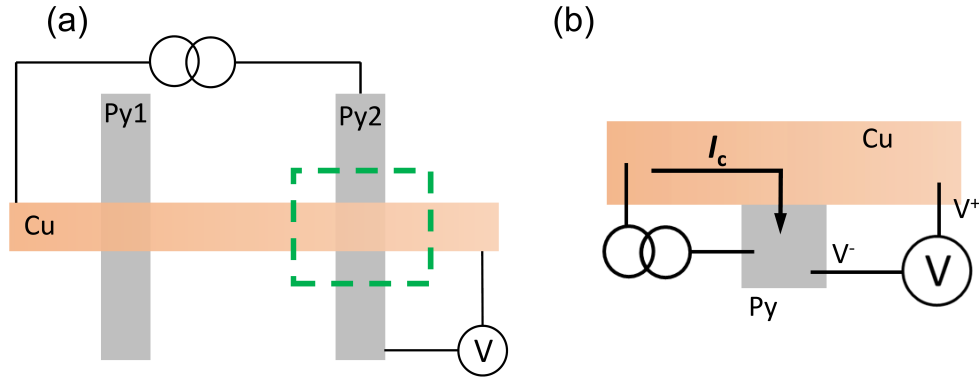


Figure 5.9: (a) The measurement setup for the estimation of the interface quality. (b) The cross-sectional image of the green region in (a).

By flowing a charge current perpendicular to the interface and measuring the voltage across it, we can check the interfacial resistance qualitatively (Fig. 5.9(b)). If the interface is an Ohmic contact, the detected voltage should be negative, reflecting an inhomogeneous current density [134]. From this measurement, however, it is difficult to determine whether the entire interface is uniformly Ohmic.

As mentioned before, we perform the Ar milling to make an Ohmic interface between F and N. In this milling process, not only the surface of the device but also the holder where the device is mounted are also etched. To investigate the effect of interfacial impurities from the holder, we inserted five different materials (Al, Py, Cu, Al, Au and stainless-steel (SUS)) in between the sample and the holder for the Ar milling process (the inset of Fig. 5.10(a)).

In Fig. 5.10(b), we show $\Delta R_S^{10\text{ K}}/\Delta R_S^{\text{max}}$ for the five different insertion materials. Apparently, $\Delta R_S^{10\text{ K}}/\Delta R_S^{\text{max}}$ takes a large value for Cu and Al, while it is small for Py and SUS.

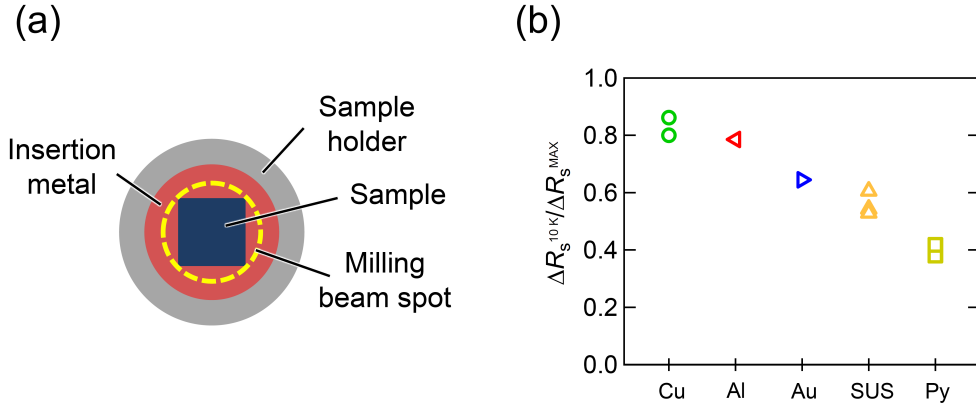


Figure 5.10: The Ar milling process for the NLSV device. (a) The schematic image of the sample holder and the insertion metal for the Ar milling. The gray circle is the sample holder, the red circle is the insertion metal, the yellow broken line shows the beam spot of Ar milling, and the blue square is the Si substrate where the device is prepared, respectively. (b) The relation between the insertion metal and the reduction rate $\Delta R_S^{10\text{ K}} / \Delta R_S^{\text{max}}$.

Especially, ferromagnetic and strong SO materials can induce an additional spin flip process. Therefore, those impurities at the interface would reduce the spin signal. These facts indicate that the reduction of ΔR_S at low temperatures are strongly affected by impurities at the interface between Py and N, and the amplitude of the reduction rate is determined by the spin-orbit interaction of the impurities. It is difficult to make further discussion, *i.e.*, why the reduction takes place below 40 K, from these data, but at least, we can clarify that the impurities at the interface is important to obtain the high-quality SH device, and we should be careful about the Ar milling process to avoid the impurities at the interface.

Chapter 6

Spin transport measurement in Spin Glass

6.1 *dc* magnetization of CuMnBi

First of all, we performed *dc* magnetization measurements of CuMnBi to determine the spin freezing temperature (T_f) of bulk and film samples. We used a commercial type superconducting quantum interference device (SQUID) magnetometer MPMS-7 (Quantum Design). We asked Prof. Toshifumi Taniguchi (Department of Earth and Space Science, Graduate School of Science, Osaka University) to measure the *dc* magnetization of CuMnBi.

In Fig. 6.1, we show the magnetization M of bulk $\text{Cu}_{99.5-x}\text{Mn}_x\text{Bi}_{0.5}$ ($x = 4.2, 8.2,$ and 10.6). With decreasing temperature, M increases since the magnetic moment of Mn follows a Curie law ($\propto 1/T$). In the ZFC process, M starts to decrease with a cusp structure. This cusp position (indicated by the arrows in the figure) corresponds to T_f . We have estimated T_f of bulk $\text{Cu}_{95.3}\text{Mn}_{4.2}\text{Bi}_{0.5}$, $\text{Cu}_{91.3}\text{Mn}_{8.2}\text{Bi}_{0.5}$, and $\text{Cu}_{88.9}\text{Mn}_{10.6}\text{Bi}_{0.5}$ to be 26 K, 36 K and 44 K, respectively. These values are almost the same as T_f of CuMn binary alloys [137, 138]. This fact clearly shows that the Bi impurities in CuMnBi does not affect to the spin glass transition.

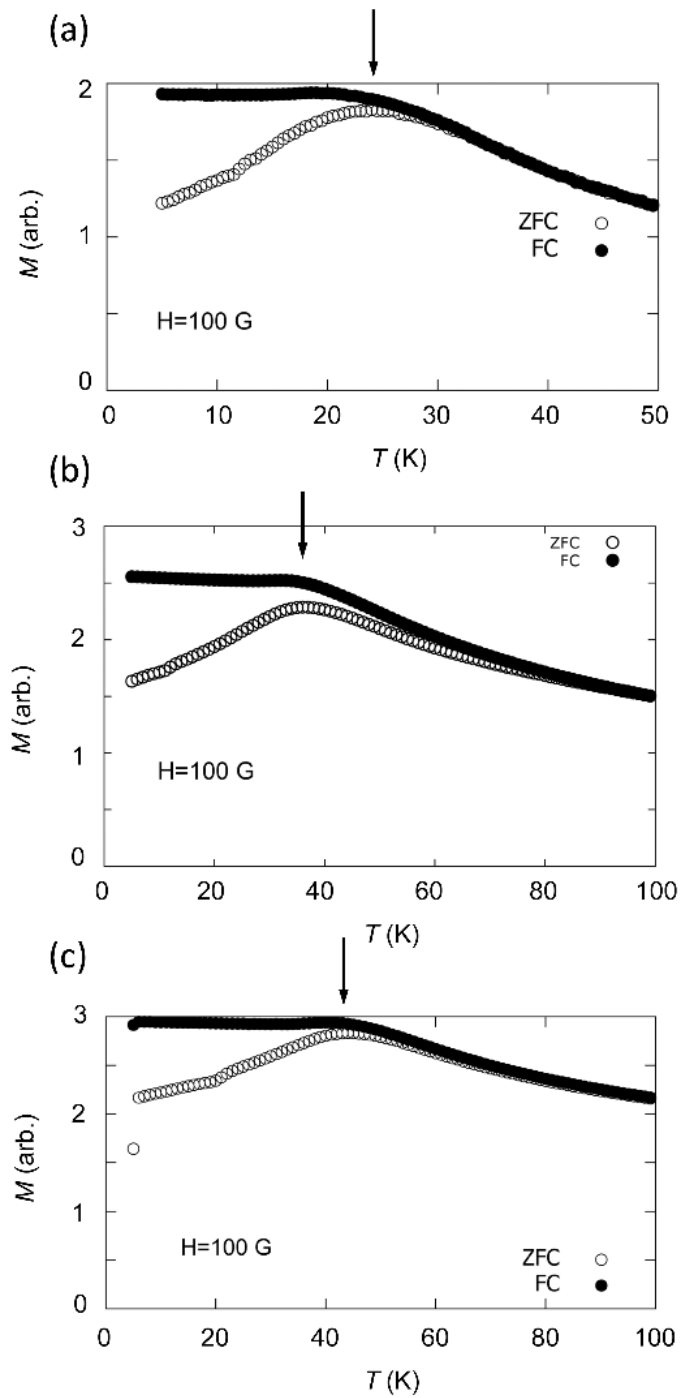


Figure 6.1: The temperature dependence of the magnetization in bulk $\text{Cu}_{99.5-x}\text{Mn}_x\text{Bi}_{0.5}$. The arrows indicate the spin glass temperatures. (a) $x = 4.2$, (b) $x = 8.2$, and (c) $x = 10.6$.

The RKKY interaction, the origin of the spin glasses, is a long-range interaction and strongly depends on the distance between magnetic impurities. Therefore, to check the thickness (or size) effect of spin glasses, we deposited a CuMnBi thin film by using an Ar sputtering and performed the similar *dc* magnetization measurement. Figure 6.2 shows a *dc* magnetization of $\text{Cu}_{88.9}\text{Mn}_{10.6}\text{Bi}_{0.5}$ thin film whose thickness is 138 nm. T_f (= 35 K) of the film is lower than that of bulk. According to the previous work about the size effect of spin glasses [139], T_f of 100 nm film is 80 ~ 90 % of bulk T_f . Thus, the present T_f obtained with the 138 nm film is quantitatively consistent with the previously reported size effect for CuMn [139].

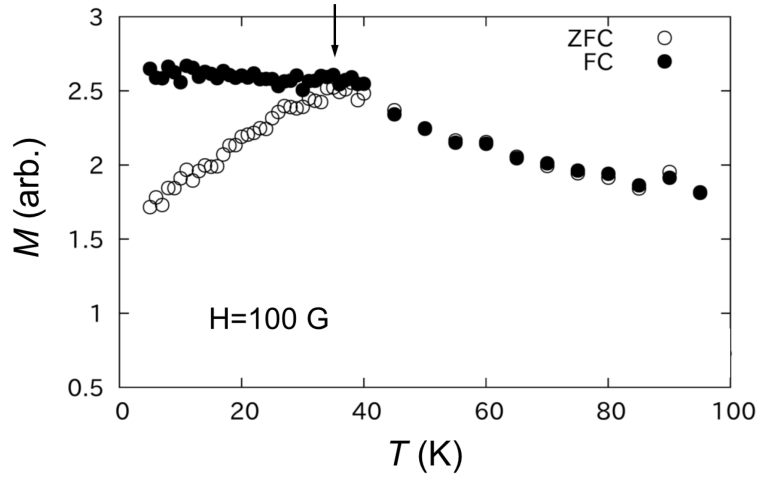


Figure 6.2: The temperature dependence of the magnetization of a $\text{Cu}_{88.9}\text{Mn}_{10.6}\text{Bi}_{0.5}$ thin film. The arrow indicates T_f of the thin film, which is about 0.8 times smaller than that of bulk.

6.2 Extraordinary Hall effect of CuMnBi

The AHEs in binary spin glass systems such as $\text{Au}_{92}\text{Fe}_8$ and $\text{Au}_{92}\text{Mn}_8$ bulk samples have been studied in Refs. [38] and [39] where the AHE and the magnetization are measured at the same time and both show a typical cusp structure at T_f [27]. We have measured the AHE for $\text{Cu}_{99.5-x}\text{Mn}_x\text{Bi}_{0.5}$. We fabricated a Hall-bar device whose thickness is 20 nm by using the photolithography technique and the Ar sputtering, as shown in the inset of Fig. 6.3(a).

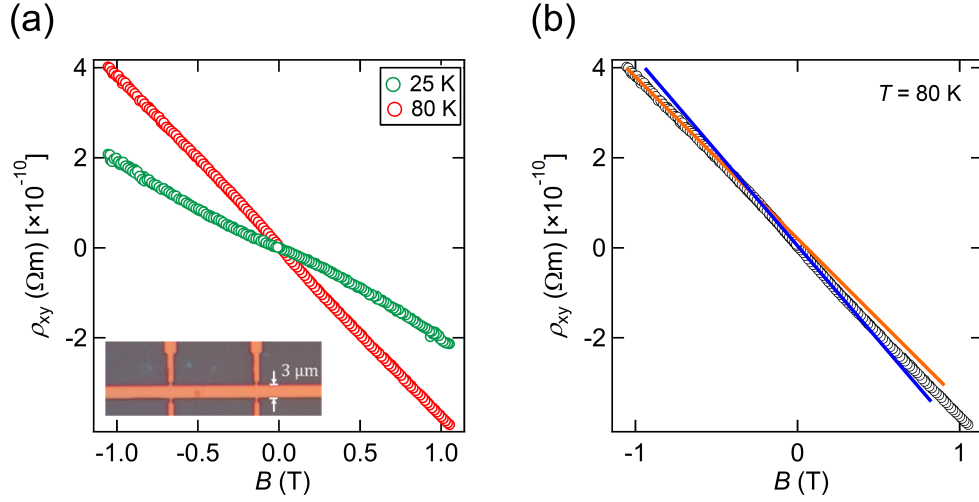


Figure 6.3: (a) Hall resistivity (ρ_{yx}) of $\text{Cu}_{95.3}\text{Mn}_{4.2}\text{Bi}_{0.5}$ at typical temperatures. The inset shows an optical microscope image of the Hal-bar device. (b) ρ_{yx} of $\text{Cu}_{95.3}\text{Mn}_{4.2}\text{Bi}_{0.5}$ at $T = 80\text{ K}$. The blue and orange lines indicate the Hall slopes in the vicinity of $B = 0\text{ T}$ and at $B = 1\text{ T}$, respectively.

The magnetic field dependence of Hall resistivity of $\text{Cu}_{95.3}\text{Mn}_{4.2}\text{Bi}_{0.5}$ is shown in Fig. 6.3. At $T = 80\text{ K}$, the Hall slope near $B = 0$ is larger than that in the high magnetic field region Fig. 6.3(b). The origin of this behavior is related with the skew scattering mechanism in the AHE as mentioned in Chap. 2. A carrier density calculated from the Hall slope at $B = 1\text{ T}$ is $\sim 8.7 \times 10^{22}\text{ cm}^{-3}$ and this value is consistent with a carrier density of Cu at room temperature ($\sim 8 \times 10^{22}\text{ cm}^{-3}$) [140]. By adopting the previous method reported by Fert [115], we took the difference between the slope at high magnetic field and the slope near the zero magnetic field region. At high magnetic field, the influence of skew scattering was negligible. Near zero magnetic field, on the other hand, the effect of skew scattering was dominant. The temperature dependence of the skew scattering term (EHE) is shown in Fig. 6.4.

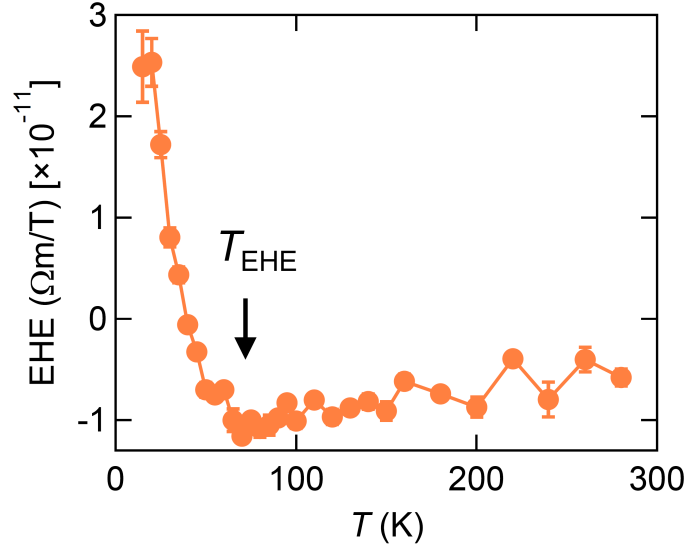


Figure 6.4: The temperature dependence of a skew scattering term (EHE) in $\text{Cu}_{95.3}\text{Mn}_{4.2}\text{Bi}_{0.5}$. The arrow indicates the temperature at which EHE takes local minimum value.

At high temperatures ($\gg T_f$), the EHE term is proportional to A/T where A is a coefficient including the SH angle α_H . In CuMnBi, the sign of α_H is negative due to the SOI of Bi. Therefore, the sign of EHE is consistent with the previous work on the SHEs in CuBi [86] and CuMnBi [13]. The EHE takes a local minimum at ~ 70 K (T_{EHE}) which is 4 times higher than T_f . The value of T_{EHE} corresponds to T^* estimated from the ISHE measurement as detailed in Sec. 6.

At low temperatures especially below $T = 30$ K, the sign of EHE is changed. The origin of the positive EHE is still open question. The Fert's theory [115] assumed that magnetic impurities could be treated as isolated localized spins because they treated diluted magnetic impurity systems. The Mn concentration of our system is 100 times higher than that of Fert's report [115]. Therefore, to understand our EHE results at low temperatures, we need a new theory including the correlation between magnetic impurities. To investigate the effect of Mn concentration, we measured the EHE in $\text{Cu}_{99.5-x}\text{Mn}_x\text{Bi}_{0.5}$ ($x = 4.2$ and 10.6). The temperature dependence of the EHE is shown in Fig. 6.5.

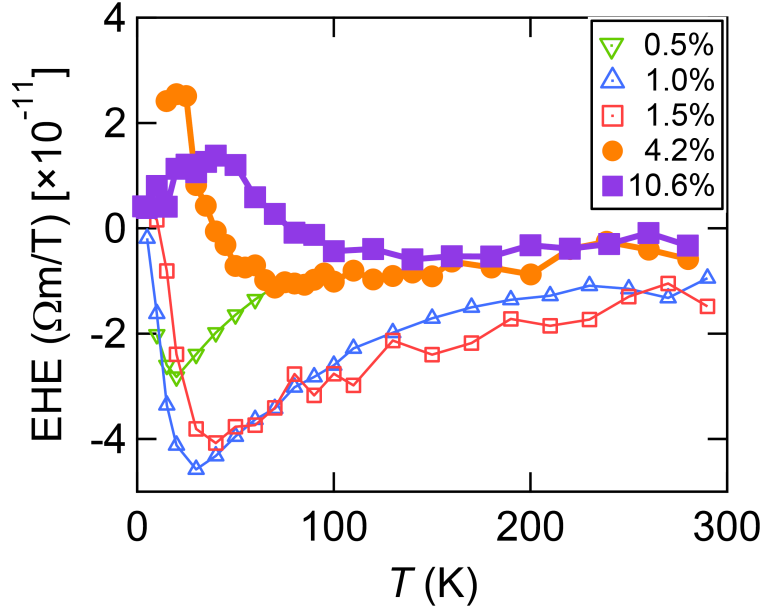


Figure 6.5: The temperature dependence of the EHE in $\text{Cu}_{99.5-x}\text{Mn}_x\text{Bi}_{0.5}$ ($x = 4.2$ and 10.6) For comparison, the EHEs in $\text{Cu}_{99.5-x}\text{Mn}_x\text{Bi}_{0.5}$ ($x = 0.5, 1.0,$ and 1.5) taken from Ref. [13] are also plotted in the same graph.

With increasing the Mn concentration, T_{EHE} shifts to the higher temperature side. For $x = 4.2$ and 10.6 , the EHE takes a maximum value at low temperatures. This temperature is very close to T_f measured in ISHE as detailed in the next section. It implies that the EHE can also detect the magnetic fluctuation of localized moments. However, to investigate the physical meaning of the EHE in the higher Mn concentration region, we need a new theory with the correlation between localized moments.

6.2.1 The surface effect of Bi impurities

Bi is known to exhibit surface and interface effects such as Edelstein effect [141] due to its strong SOI. In order to show that various phenomena of CuMnBi measured in this study are not interfacial effects but bulk effects, we fabricated a bilayer Hall bar consisting of insulating Bi_2O_3 and spin glass $\text{Cu}_{97}\text{Mn}_3$ thin films. The bilayer is continuously deposited in an ultrahigh vacuum, and the interface between $\text{Cu}_{97}\text{Mn}_3$ and Bi_2O_3 is kept clean. In this Hall-bar device, Bi could exist only at the bottom of the CuMn film. We measured the Hall resistance of the device. By using the same analysis as before, the temperature dependence of the EHE is shown in Fig. 6.6.

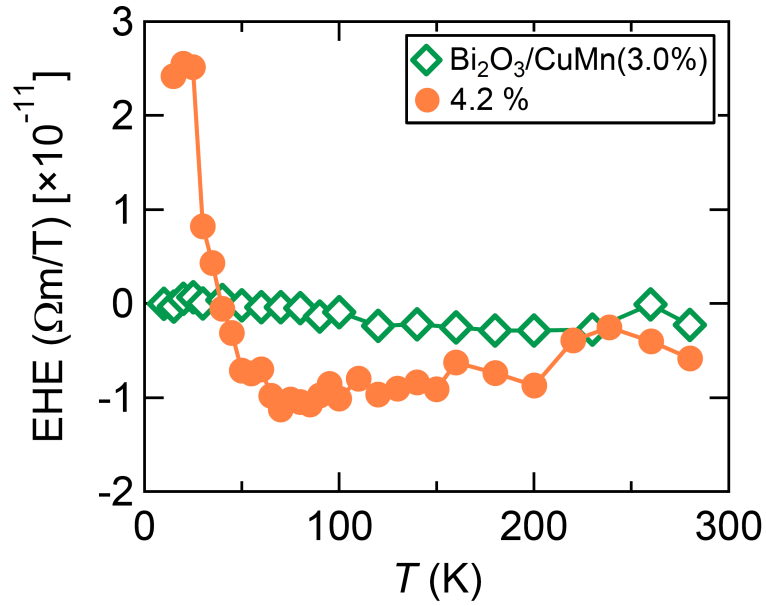


Figure 6.6: The temperature dependence of the EHE in a $\text{Bi}_2\text{O}_3/\text{Cu}_{97}\text{Mn}_3$ bilayer device. The yellow line shows the EHE of $\text{Cu}_{95.3}\text{Mn}_{4.2}\text{Bi}_{0.5}$ for comparison.

The EHE signal is almost zero in the whole temperature range. Therefore, this is a strong evidence that the measured signals do not originate from the surface or interfacial effect but bulk effect.

6.3 Inverse spin Hall effect in CuMnBi

In order to observe the ISHE in spin glasses below T_f , we fabricated the SH device based on the LSV structure with a CuMnBi wire. The typical device is shown in Fig. 6.7. The device consists of two ferromagnetic Py wires and a middle $\text{Cu}_{99.5-x}\text{Mn}_x\text{Bi}_{0.5}$ wire, which are bridged by a Cu stripe.

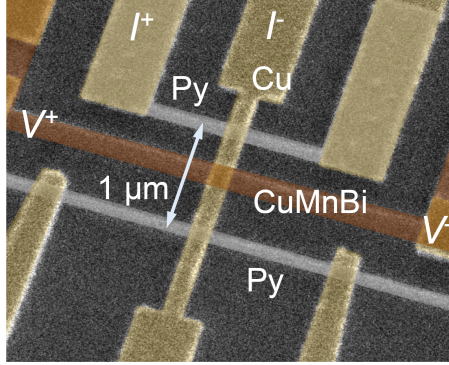


Figure 6.7: The scanning electron micrograph of a typical SH device.

By flowing an electric current from one of the Py wires (top wire) to the Cu stripe, spin accumulation is generated at the interface between Py and Cu. A spin current flows in the Cu stripe (downward) as a result of the diffusion process of spin accumulation. When a strong SO material (in the present case, $\text{Cu}_{99.5-x}\text{Mn}_x\text{Bi}_{0.5}$ ($x = 4.2, 8.2, \text{ and } 10.6$)) is placed underneath the Cu stripe within the SDL of Cu ($\sim 1 \mu\text{m}$ at low temperatures), a part of spin current is injected into $\text{Cu}_{99.5-x}\text{Mn}_x\text{Bi}_{0.5}$ because of its stronger spin-orbit interaction due to the Bi impurities. When the magnetization of the Py wire is polarized along the Cu stripe, a spin-to-charge conversion is generated along the $\text{Cu}_{99.5-x}\text{Mn}_x\text{Bi}_{0.5}$ wire direction.

The typical ISHE resistances (detected ISHE voltage divided by the injection current from Py to Cu) of $\text{Cu}_{88.9}\text{Mn}_{10.6}\text{Bi}_{0.5}$ are shown in Fig. 6.8(a) When $B > 0.2 \text{ T}$ (or $< -0.2 \text{ T}$), R_{ISHE} is fully saturated. This saturation field corresponds to the saturation field of an AMR of Py wire (Fig. 6.8(b)). At 100 K higher than T_f of bulk $\text{Cu}_{88.9}\text{Mn}_{10.6}\text{Bi}_{0.5}$, a clear negative ISHE signal ($\Delta R_{\text{ISHE}} \sim -20 \mu\Omega$) is observed. The negative ISHE originates from the ISHE at Bi impurities in Cu. The sign of ISHE is consistent with previous measurements in CuBi and CuMnBi [13, 86]. However, at low temperatures, the ISHE signals significantly vanishes at 20 K. To investigate the amplitude of ISHE, we define ΔR_{ISHE} , as shown in Fig. 6.8.

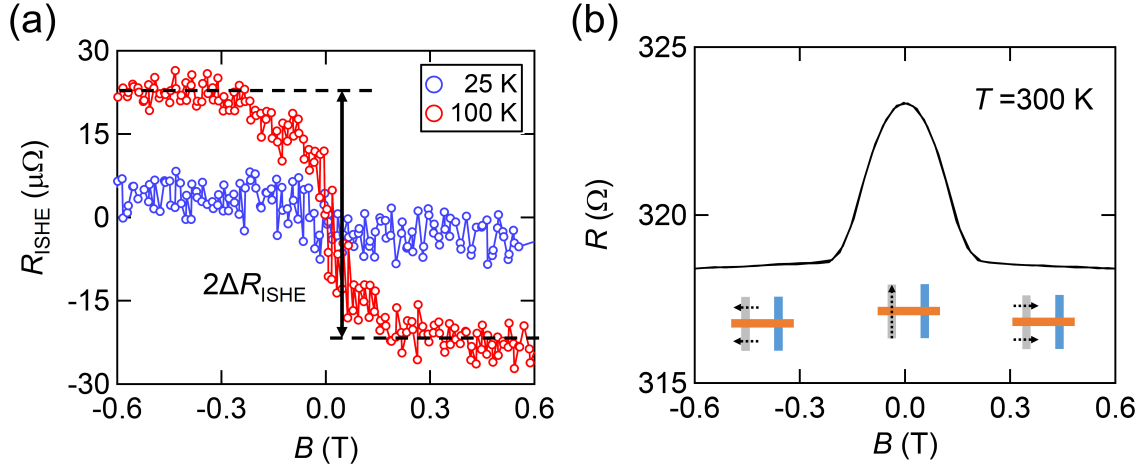


Figure 6.8: (a) ISHE resistances (R_{ISHE}) of $\text{Cu}_{88.9}\text{Mn}_{10.6}\text{Bi}_{0.5}$ measured at typical temperatures. The amplitude of the ISHE resistance ΔR_{ISHE} is defined as the black arrow. (b) An AMR of one of the Py wires. The arrows indicate the magnetization directions.

The temperature dependence of ΔR_{ISHE} in a $\text{Cu}_{88.9}\text{Mn}_{10.6}\text{Bi}_{0.5}$ nanowire is shown in Fig. 6.9.

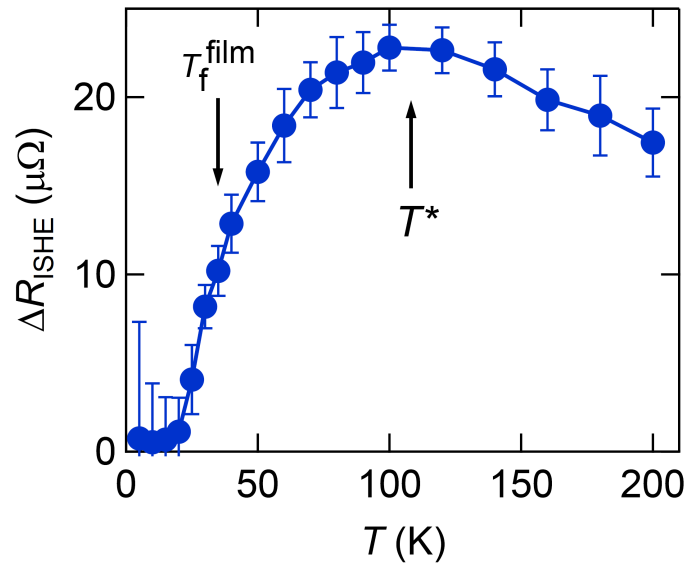


Figure 6.9: The temperature dependence of ΔR_{ISHE} in $\text{Cu}_{88.9}\text{Mn}_{10.6}\text{Bi}_{0.5}$. The black arrows indicate T^* and also T_f of film, respectively.

At high enough temperatures, ΔR_{ISHE} increases with decreasing temperatures because the SDL of the Cu channel becomes longer with temperatures. In other words, the absolute value of the injected pure spin current into the CuMnBi wire becomes larger with decreasing temperature. ΔR_{ISHE} takes a maximum value at T^* which is similar behavior in the previous work [13]. For $T < T^*$, however, ΔR_{ISHE} starts to decrease and

becomes almost zero at low temperatures especially below T_f^{film} which is determined by the magnetization measurement with the thin film, as detailed in Sec. 6.1. Such a large suppression of ISHE has never been seen for lower Mn concentrations [13]. In addition, there is no difference on ΔR_{ISHE} between FC process and ZFC process. It is intuitively not consistent with magnetization measurements of spin glasses. However, according to the previous work about ISHE [13] and electrical conductivity of spin glasses [137], the difference between ZFC and FC does not appear in CuMn. The origin of no difference between FC and ZFC may be related to the SOI of the host metal.

To investigate the Mn concentration dependence of the ISHE, we measured the ISHE in $\text{Cu}_{99.5-x}\text{Mn}_x\text{Bi}_{0.5}$ with three different concentration: $x = 4.2, 8.2,$ and 10.6 (Fig. 6.10). Here, the temperature at which ΔR_{ISHE} becomes zero is defined as T_0 .

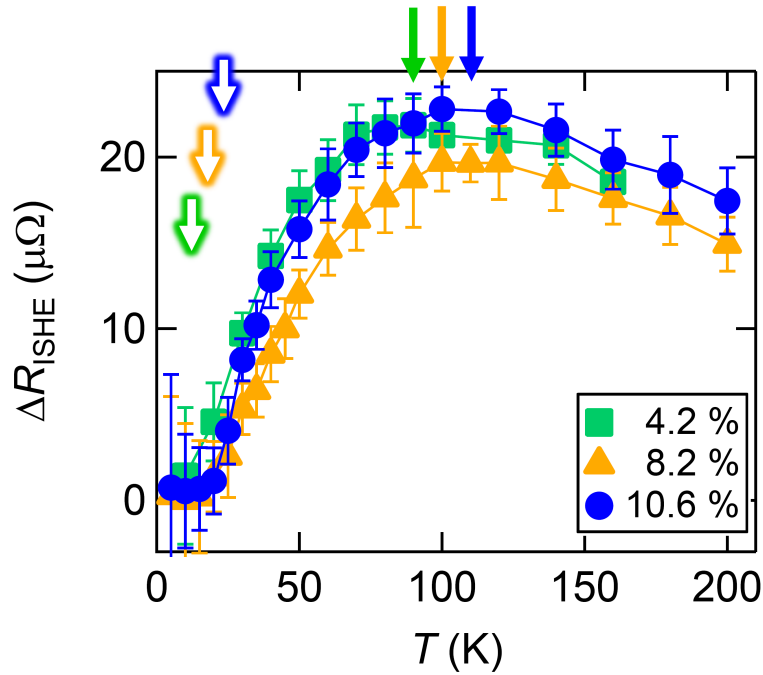


Figure 6.10: The temperature dependence of ΔR_{ISHE} of $\text{Cu}_{99.5}\text{Mn}_x\text{Bi}_{0.5}$ ($x = 4.2, 8.2,$ and 10.6). The solid arrows indicate T^* and the open arrows indicates the temperature T_0 at which ΔR_{ISHE} vanishes, respectively.

With increasing the Mn concentration, T^* and T_0 shift to the higher temperature side. This behavior is consistent with the property of spin glasses.

What is the origin of the reduction in ΔR_{ISHE} ? A generated current by the ISHE can be written as:

$$\mathbf{j}_c \propto \mathbf{j}_s \times \mathbf{s} \quad (6.1)$$

where \mathbf{j}_c is the converted charge current, \mathbf{j}_s is the injected spin current into CuMnBi and \mathbf{s} is the spin polarization of conduction electron spins. The reduction of ΔR_{ISHE} means the reduction of either \mathbf{j}_s or \mathbf{s} . When there is a SO material underneath the

Cu bridge, \mathbf{j}_s is always perpendicular to the plane and should have a finite value even though the SOI of the middle wire is quite weak. In addition, according to the previous report on CuMnBi [13], \mathbf{j}_s does not strongly depend on temperature. This indicates that it is natural to consider that the direction of \mathbf{s} is randomized in the spin glass material.

6.3.1 Spin Hall angle of CuMnBi

As mentioned above, ΔR_{ISHE} contains not only the contribution of the ISHE in CuMnBi but also the SDL of the Cu channel. Thus, in order to discuss only the effect of the ISHE in CuMnBi, we need to calculate the SH angle. The SH angle can be obtained by using λ_{CuMnBi} in the spin absorption method as detailed in 6.3.4. By substituting all the detailed parameters into Eq. (3.38) in Sec. 3.4, we can calculate the SH angle α_{H} of $\text{Cu}_{99.5-x}\text{Mn}_x\text{Bi}_{0.5}$ ($x = 4.2$ and 10.6). To focus on the effect of Mn, α_{H} of $\text{Cu}_{99.5-x}\text{Mn}_x\text{Bi}_{0.5}$ is normalized by α_{H} of $\text{Cu}_{99.5}\text{Bi}_{0.5}$: $\eta \equiv \alpha_{\text{H}}^{\text{CuMnBi}} / \alpha_{\text{H}}^{\text{CuBi}}$.

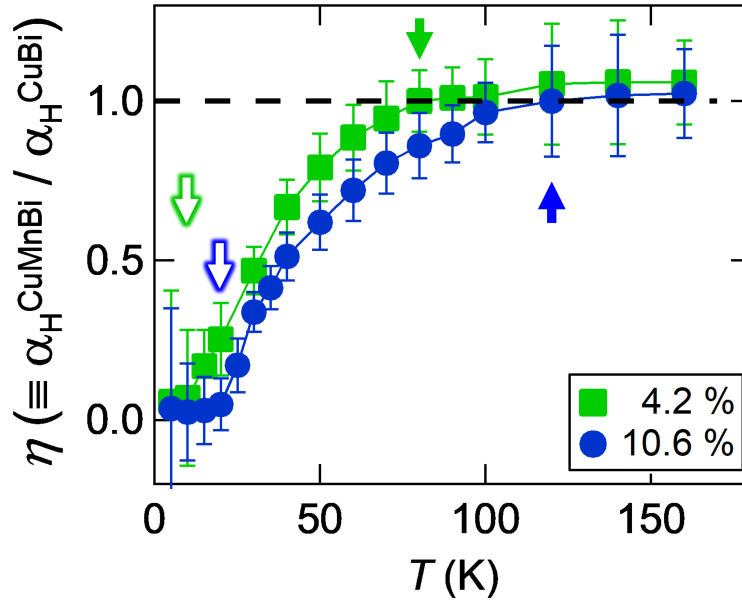


Figure 6.11: Temperature dependence of η , the SH angle of $\text{Cu}_{99.5-x}\text{Mn}_x\text{Bi}_{0.5}$ ($x = 4.2$ and 10.6) normalized by that of $\text{Cu}_{99.5}\text{Bi}_{0.5}$. Solid and open arrows indicate T^* and T_0 , respectively.

We note that the SHE of $\text{Cu}_{99.5}\text{Bi}_{0.5}$ is originated from the skew scattering at the Bi impurity sites [13, 86]. In other words, $\alpha_{\text{H}}^{\text{CuMnBi}}$ is independent of the Mn concentration. In such a situation, the skew scattering contribution from the Mn impurities in Cu is expected to be negligibly small, as indicated in Ref. [13]. Therefore, in principle, η should be 1 at any temperature. This is realized in the high temperature region for all the Mn concentrations, as shown in Fig. 6.11. T^* is defined as the lowest temperature at which the condition $\frac{\eta(T+\Delta T) - \eta(T)}{\eta(T)} < 5\%$ is fulfilled. With decreasing temperature, on the other hand, η starts to deviate from 1 at T^* and eventually reaches 0.

6.3.2 Discussion: origin of reduction of inverse spin Hall effect

As mentioned above, the reduction of ΔR_{ISHE} originates from the randomization of the spin direction \mathbf{s} . In CuMnBi, Cu and Mn have weak SOIs and these do not work as the spin scatterers in ISHE. Thus, the amplitude of the ISHE is determined by the Bi impurities. Based on these facts, the microscopic image of conduction electron spin can be illustrated as shown in Fig. 6.12.

When the Mn concentration is much higher than the Bi one, the injected conduction electron spin is firstly correlated with the Mn moments. During this process, the conduction electron spin loses its coherence. Thus, the scattering angle becomes smaller, compared to that without any correlations with the Mn moments.

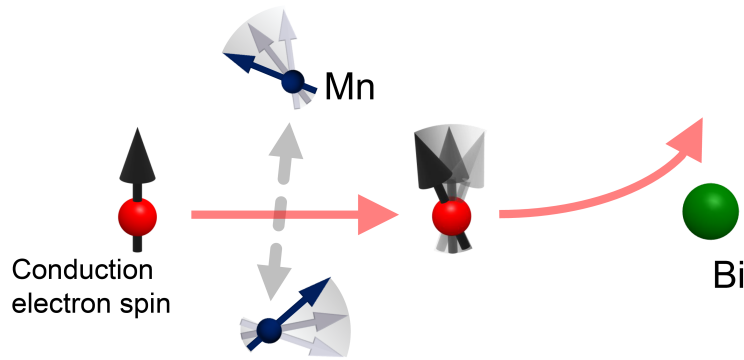


Figure 6.12: A microscopic picture of the ISHE in CuMnBi.

Furthermore, the spin scattering process at the Bi impurities does not depend on the temperature [13]. The temperature dependence of \mathbf{s} can be explained by the following scenario:

At high enough temperatures (Fig. 6.13 (a)), the Mn moments fluctuate with high frequencies and the conduction electron spins cannot follow this fast motion. Thus, the ISHE signal is simply determined by the skew scattering at the Bi impurity sites. With decreasing temperature, the fluctuation of the Mn moments is getting slower. The conduction electron spins can feel the fluctuation and the directions of conduction electron spins are randomized. Since the Mn moments are randomly frozen for $T < T_0$ (Fig. 6.13 (c)), the directions of conduction electron spins become completely random and thus the ISHE signal disappears well below T_0 .

Comparing the freezing behavior of this Mn moments with the magnetic dynamics of spin glasses, T_0 should be equivalent to T_f of the spin-glass nanowire.

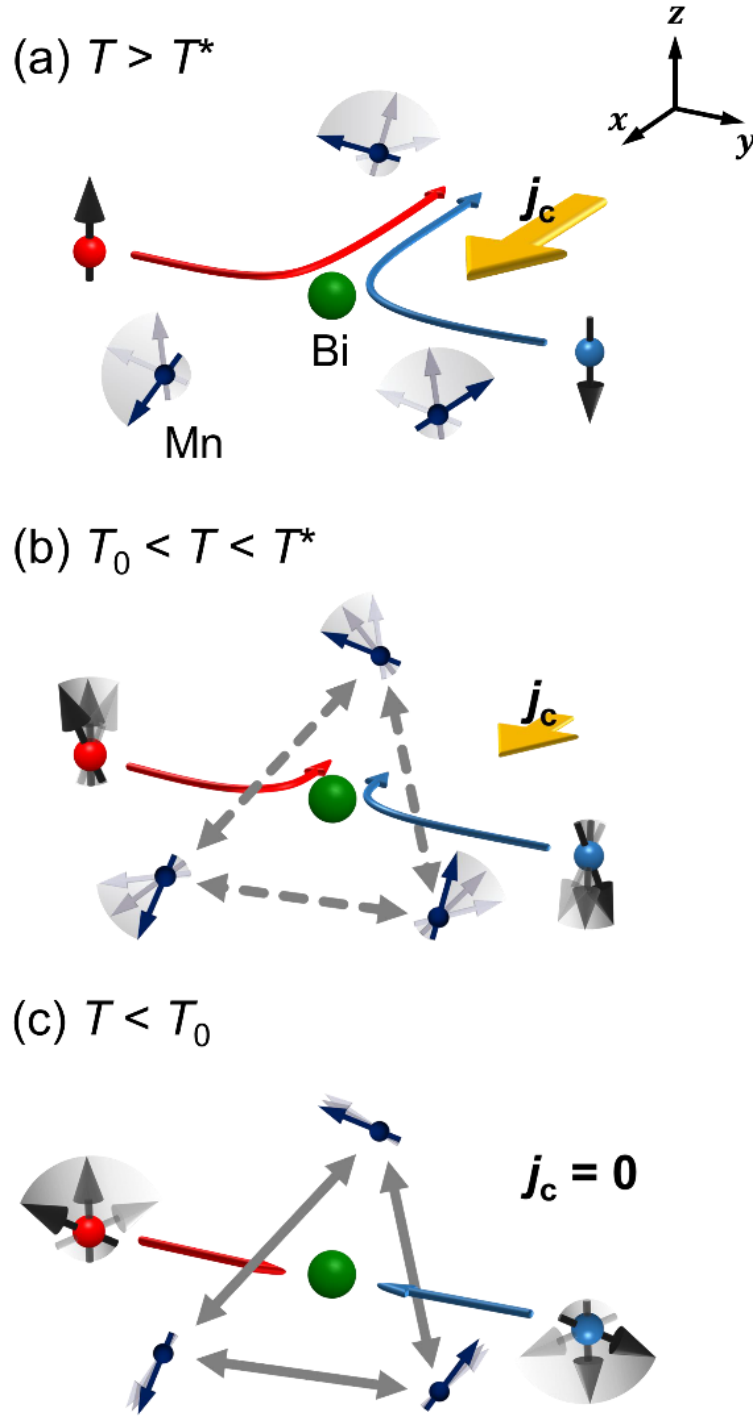


Figure 6.13: Illustrations of ISHE in CuMnBi spin glass at different temperature regions: (a) $T > T^*$, (b) $T_0 < T < T^*$, and (c) $T < T_0$. Black arrows with red and blue spheres are conduction electrons with spin-up and spin-down, respectively, and red and blue arrows show those trajectories. The shadows indicate fluctuations of conduction electron spin (shorter arrows) and magnetic moments of Mn (longer arrows). Yellow and gray arrows indicate the charge current density j_c generated at the Bi sites (green spheres) due to ISHE and a magnetic interaction between the Mn sites, respectively.

6.3.3 Spin treacle region

Finally, we relate two different temperatures $T_0 = T_f$, and T^* of the nanometer-scale spin glasses. The two temperatures are plotted as a function of Mn concentration x in Fig. 6.14.

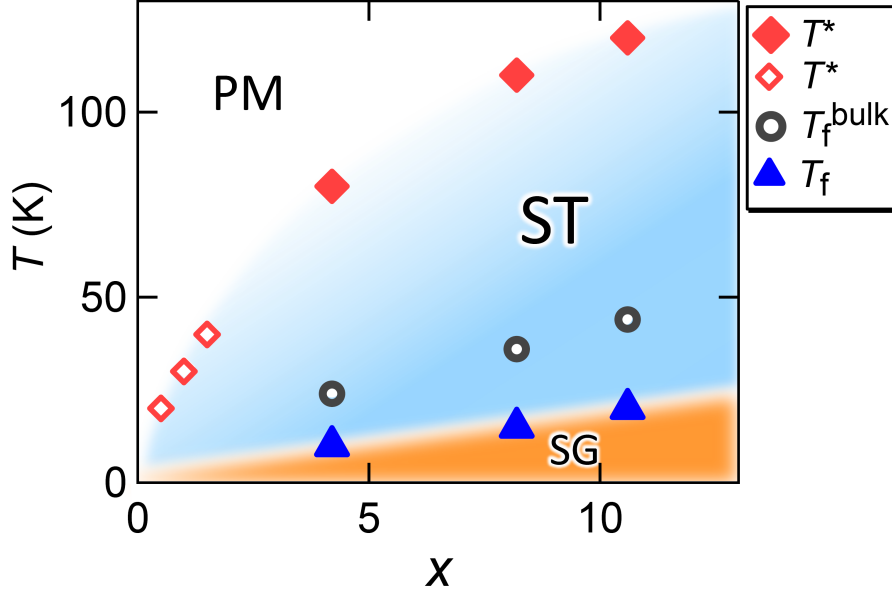


Figure 6.14: Relations of T_f and T^* with the Mn concentration x for $\text{Cu}_{99.5-x}\text{Mn}_x\text{Bi}_{0.5}$. T_f and T^* are indicated by the solid blue triangle and the solid red square respectively. Open circle indicates the spin freezing temperature T_f^{bulk} of bulk $\text{Cu}_{99.5-x}\text{Mn}_x\text{Bi}_{0.5}$ determined from the magnetization measurements. The data for $x = 0.5, 1.0$, and 1.5 (red open square) are taken from the previous work [13].

T_f increases linearly with x , as in the case of bulk spin glass [137, 138]. The spin glass phase is located at the low temperature and high magnetic impurity concentration regions, but shifted to the lower temperature side compared to the bulk spin glass phase because of the size effect of spin glasses [139]. From magnetization measurements, only a boundary between the spin glass state and the paramagnetic state is assigned. But as clearly demonstrated in this work, we have found a new regime, that is “spin treacle region”, where the magnetic moments are fluctuating before they start to freeze. The spin treacle region increases with x . Here we see that T_f linearly increases with increasing x , while T^* seems to be proportional to x^a where $a \approx 1/3$. We need further data to determine a precise exponent. This result shows how quantitative characterization of magnetic fluctuations on nanometer-scale samples is possible using spin current.

The similar behavior would seem to correspond to the results of μ SR measurements by Campbell *et al.* in AgMn and AuFe alloys (Fig. 6.15) [145].

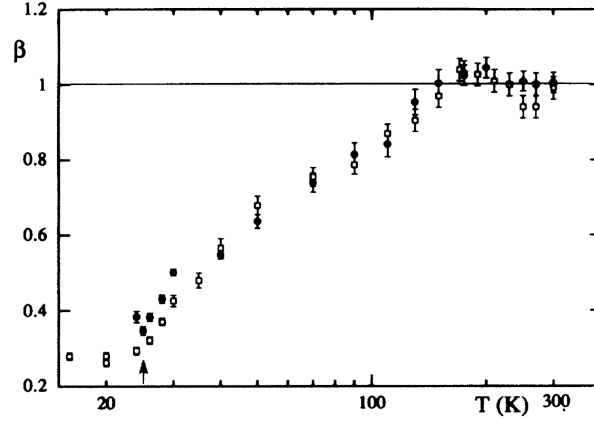


Figure 6.15: β in Eq. (6.2) of $\text{Ag}_{93}\text{Mn}_7$ obtained from μ SR measurements as a function of temperature [145].

The muon spin correlation function $P(t)$ could be fitted by a stretched exponential with $\frac{1}{3} < \beta < 1$:

$$P(t) = \langle S_\mu^z(0)S_\mu^z(t) \rangle \propto \exp [-(\lambda t)^\beta] \quad (6.2)$$

where $S_\mu^z(t)$ is the muon spin component along the direction z . At high enough temperature, $\beta = 1$ which indicates the usual simple exponential decay expected in a normal paramagnetic phase. β decreases with decreasing temperature and $\beta = \frac{1}{3}$ below the freezing temperature. Based on these results, Niimi *et al.* tried to extend this model to the evaluation of the depolarization of conduction electron spins theoretically [13]. The original theory was based on Kubo-Toyabe theory for the evaluation of an effective muon spin polarization, but they assumed that the conduction electron spin had the same analogy as muon spin: the spin current also fluctuated a characteristic frequency $\nu(T) \propto (T - T_f)^2$ which was referred from the μ SR data in Ref. [142] above T_f , and ν vanished below T_f . Figure 6.16 shows the simulated results on the effective spin polarization rate $G_z(\tau_{\text{sk}}, \nu(T))$ where τ_{sk} is the skew scattering time: $\rho_{\text{SHE}} = m/ne^2\tau_{\text{sk}}$.

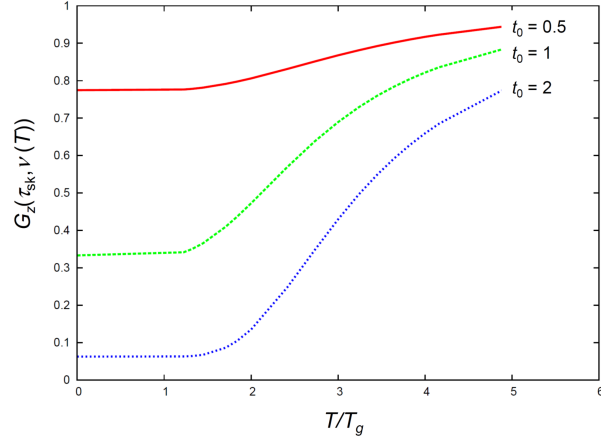


Figure 6.16: G_z calculated with the Kubo-Toyabe model [13]. t_0 represents the product of τ_{sk} and the Gaussian distribution width for the randomly fluctuating field in spin glasses.

At enough high temperature, $\nu(T)$ is large and $G_z = 1$. On the other hand, G_z starts to decrease with decreasing temperature and saturates at low temperatures. The result seems to be consistent with our experimental data. However, it does not give zero value for the spin current depolarization below T_f . This is presumably because a spin current propagates diffusively while a muon spin passes through the material ballistically. Therefore, to understand the ISHE in CuMnBi deeply, we have to investigate the relation between spin fluctuations and the SDL.

6.3.4 Spin diffusion length of CuMnBi

The spin absorption method enables us to measure not only the ISHE but also to estimate the SDL on the same device [6]. To estimate the SDL, we measure spin accumulation signals with and without the CuMnBi wire: $\Delta R_S^{\text{with}}/\Delta R_S^{\text{without}} (\equiv \eta)$. From the relation, λ_{CuMnBi} can be estimated using Eq. (3.32). In Fig. 6.17, we show the NLSV signals with and without the $\text{Cu}_{95.3}\text{Mn}_{4.2}\text{Bi}_{0.5}$ wire at 10 K.

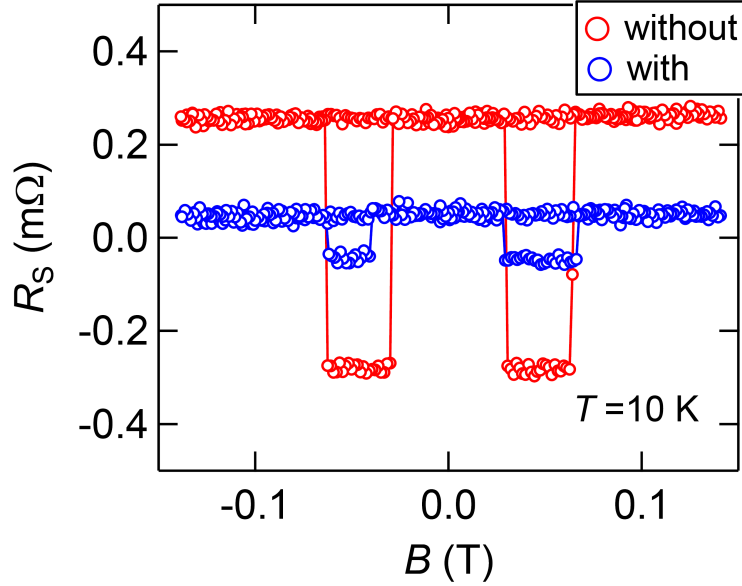


Figure 6.17: Typical NLSV signals with and without the $\text{Cu}_{95.3}\text{Mn}_{4.2}\text{Bi}_{0.5}$ wire measured at 10 K. The red and blue curves show the spin signals without and with the $\text{Cu}_{95.3}\text{Mn}_{4.2}\text{Bi}_{0.5}$ middle wire, respectively.

The results exhibit a clear spin absorption effect, assuring that the spin currents are really absorbed into the CuMnBi middle wire via the Cu strip. From the experimental results, we can calculate the spin absorption rate η : in other words, how much of spin current flowing in the Cu channel is really absorbed in the CuMnBi middle wire. From the 1D spin-diffusion model in Eq. (3.32), we can estimate the SDL of CuMnBi (λ_{CuMnBi}). Note that λ_{CuMnBi} is the only fitting parameter in Eq. (3.32), since L , R_N , R_F , ρ_{CuMnBi} , etc. are already obtained from other transport measurements.

In Fig. 6.18, we show the temperature dependence of λ_{CuBi} and λ_{CuMnBi} . λ_{CuBi} is almost constant (~ 30 nm) in this temperature region. λ_{CuMnBi} is two times smaller than λ_{CuBi} at 160 K. The difference of the SDL originates from the difference of the resistivity between CuBi and CuMnBi. With decreasing temperature, on the other hand, λ_{CuMnBi} becomes gradually shorter, and at 10 K, λ_{CuMnBi} is 3 times smaller than that at 160 K and almost one order smaller than λ_{CuBi} at 10 K. Furthermore, there is no anomaly near T_f . From this result, the large reduction of λ_{CuMnBi} originates from the Mn impurities. The result indicates that the random field generated by frustration of Mn moments affects conduction electron spins.

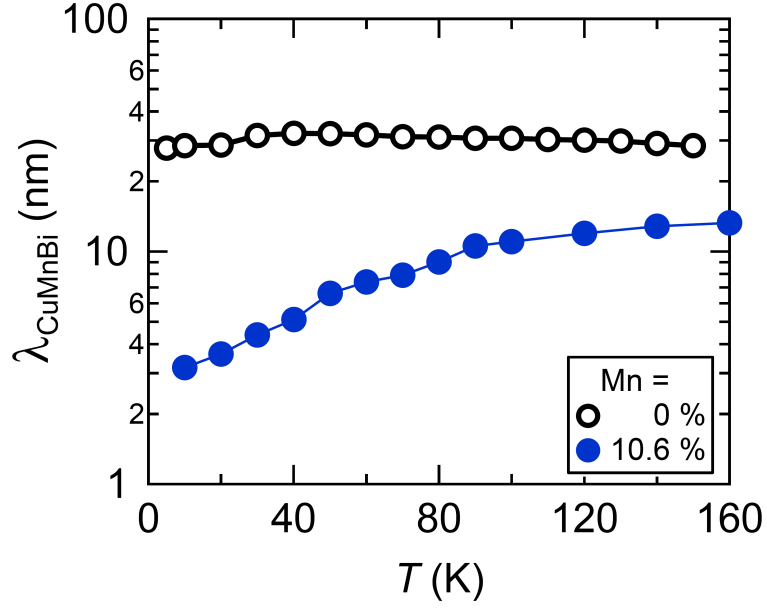


Figure 6.18: Temperature dependence of λ for CuBi and $\text{Cu}_{88.9}\text{Mn}_{10.6}\text{Bi}_{0.5}$.

The SDL λ_S can be rewritten with the spin relaxation time τ_S by using the following relation:

$$\lambda_S = \sqrt{D\tau_S}, \quad (6.3)$$

where D is the diffusion constant. The temperature dependence of $1/\tau_{\text{CuMnBi}}$ is shown in Fig. (6.19). The $1/\tau_{\text{CuMnBi}}$ increases with decreasing temperature.

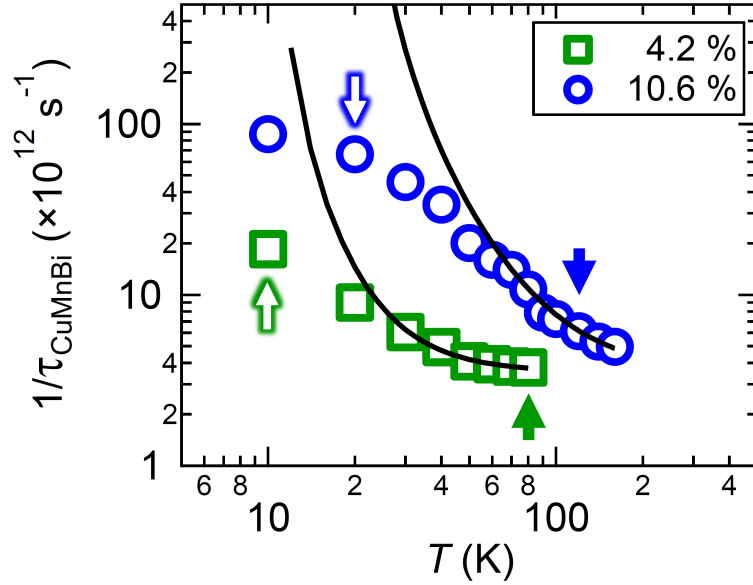


Figure 6.19: The temperature dependence of $1/\tau_{\text{CuMnBi}}$ for two Mn concentrations. The black curve is the fitting line which is proportional to $(T - T_f)^{-2}$.

The black curve indicates the curve fitting with $C/(T - T_f)^2$, where C is a constant value. The fitting works in the temperature region of $3T_f < T < T^*$, but the relation does not work, as T approach T_f . According to the Elliott-Yafet (EY) mechanism [129, 130], τ_S is proportional to T in a dirty (metallic) system, and in a clean such as semiconductors, D'yakonov-Perel (DP) mechanism is dominant where $\tau_S \propto 1/T$ [7]. However, τ_{CuMnBi} meets neither the EY nor DP mechanisms. This fact indicates that $1/\tau_{\text{CuMnBi}}$ includes the effect of spin fluctuations. The similar temperature dependence has been discussed in the depolarization rate of AgMn in μSR [142] and also in the linewidth of ESR spectrum in CuMn alloys [143, 144]. While the ESR detects spin dynamics of the Mn atom, the μSR and spin transport measurement detect the motion of muon spin and conduction electron spin, respectively. At high enough temperatures, the muon and the conduction electron spins do not feel the fast motion of Mn impurities. With decreasing temperature, the fluctuation of Mn becomes slower and the muon and conduction electron spins start to couple with this fluctuation, resulting in the further reduction of λ_{CuMnBi} . However, ESR and μSR should be not suitable to estimate τ_S near T_f because of their intrinsic time constants. Thus, a quantitative theory demonstrating this spin relaxation time is needed: ideally it should incorporate both the diffusive motion of the spin current and the effect of slow dynamics at the vicinity of T_f .

Chapter 7

Detection of Spin Fluctuations in Ag_2CrO_2

In the following section, we explain how to make the Ag_2CrO_2 thin film device. There are various methods to make a crystal thin, but there are a few reports on the fabrication of a thin film crystal from a tiny polycrystalline sample. Thus, it was necessary to establish a new method to fabricate a thin film device.

7.1 Fabrication of Ag_2CrO_2 thin film

The mechanical exfoliation technique so-called “scotch tape technique” is one of the methods to produce a thin film by exfoliating a layered crystal with a scotch tape. When the interaction between the layers, *i.e.*, van der Waals interaction, is weaker than the adhesive strength of the scotch tape, the layered material can be exfoliated by the scotch tape. This method has been well-known since Novoselov *et al.* succeeded in making a single layer of graphite with the scotch tape [17]. The method has attracted much attention as an easy technique to produce a clean two-dimensional system. Our fabrication process of Ag_2CrO_2 thin films is also based on the scotch tape method. In the case of Ag_2CrO_2 , however, the interlayer interaction is stronger than usual van der Waals materials because the exfoliation layer is the Ag_2 layer, which is close to metallic coupling. Therefore, we have established two procedures to fabricate the Ag_2CrO_2 thin film. The polycrystalline Ag_2CrO_2 was provided by Prof. Hiroyuki Yoshida at Hokkaido University.

The first procedure is as follows. First of all, we pounded Ag_2CrO_2 samples on a glass plate, in order to obtain smaller pieces of Ag_2CrO_2 . We picked up the small grains of Ag_2CrO_2 with a scotch tape (Nitto SPV363) and then pasted them onto a thermally oxidized silicon substrate with several 100 nm thick gold marks. After removing the scotch tape from the substrate, we prepared another silicon substrate without any gold marks and pushed it onto the silicon substrate with the Ag_2CrO_2 flakes and the 100 nm thick gold marks (see Fig. 7.1). While these procedures, the specimen and the substrate were warmed at 60 °C in order to weaken the bonding between the Ag_2 and CrO_2 layers and to make the exfoliation easier.

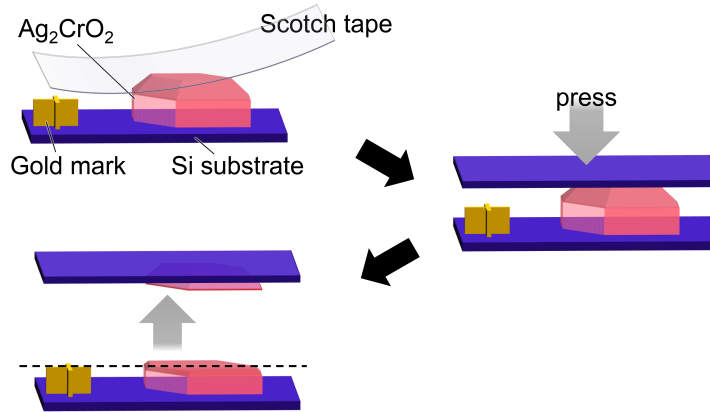


Figure 7.1: Schematics of the procedure to fabricate thin films of Ag_2CrO_2 .

In this process, some of the Ag_2CrO_2 flakes become thinner than 100 nm and relatively thick Ag_2CrO_2 flakes are attached to the substrate without the gold marks. As a result, a few thin Ag_2CrO_2 flakes remain on the substrate with the gold marks, as shown in Fig. 7.2(a). We then deposited Cu electrodes by using EB lithography (Fig. 7.2(b)). These thicknesses have been confirmed by a commercially available atomic force microscope, as shown in Fig. 7.2(c).

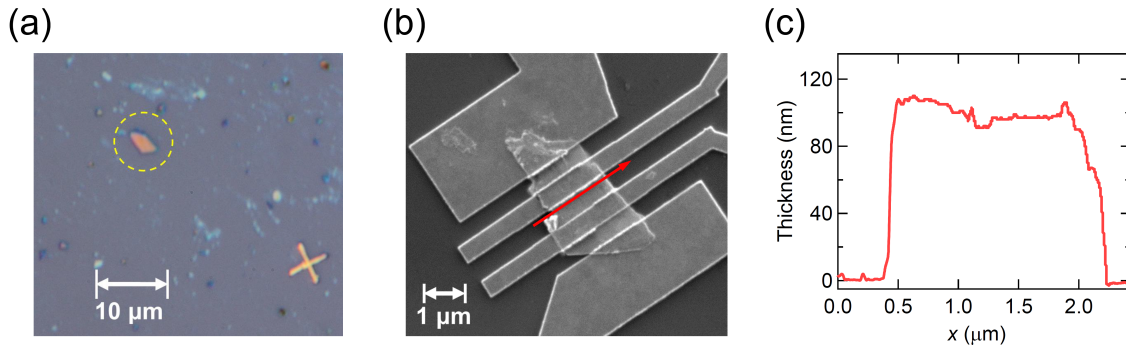


Figure 7.2: (a) Optical microscope image of an exfoliated thin Ag_2CrO_2 film. (b) The scanning electron microscope image of a fabricated device. (c) Cross section of the Ag_2CrO_2 thin film along the red arrow in (b) measured with an atomic force microscope. The thickness of the film is about 100 nm.

Thanks to this procedure, we were able to fabricate ~ 100 nm films. However, the thickness of the film is limited by the thickness of the gold mark. Thus, to fabricate a thinner film, we have to use the other procedure. The second procedure is based on the previous paper about an exfoliation method for materials that are difficult to cleave [146]. First of all, we put polycrystalline Ag_2CrO_2 samples on Nitto No. 31¹ and

¹The adhesive strength of Nitto No. 31 tape is stronger than that of Nitto SPV363 tape.

cleave them with Nitto No. 31 about 100 times. Next, we rubbed the Nitto No. 31 tape (including thin films of Ag_2CrO_2) with a Nitto SPV363 tape in order to transfer Ag_2CrO_2 thin film onto the Nitto SPV363 tape. After that, we pasted the tape onto a thermally oxidized silicon substrate with several 100 nm thick gold marks in order to transfer the thin film onto the Si substrate. While these procedures, the specimen and the substrate were kept at 60 °C because of the same reason as the previous exfoliation procedure.

7.2 STEM

In order to investigate a quality of device and also the crystal orientation, we observed a cross-sectional image of our Ag_2CrO_2 device with the scanning transmission electron microscope.

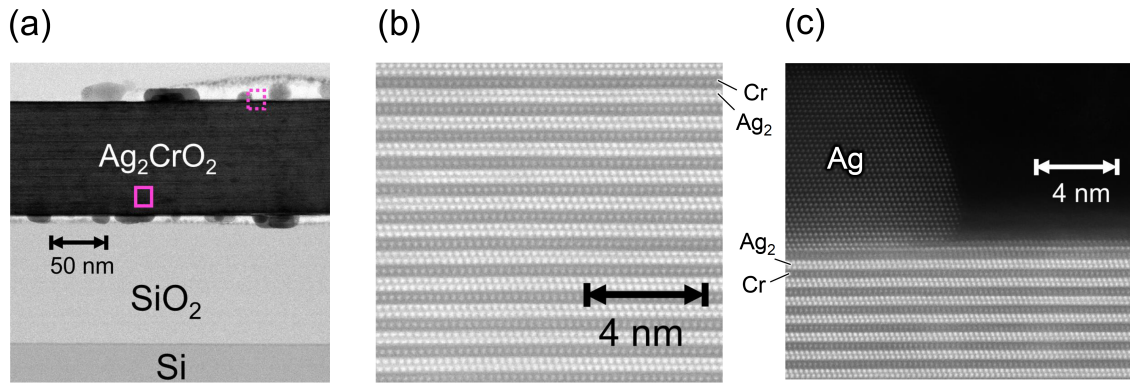


Figure 7.3: STEM images of a typical Ag_2CrO_2 device. (a) Bright-field STEM image of a wide area. (b) High angle annular dark-field STEM image in the area shown with the solid square in (a). The bright and dark spheres correspond to Ag and Cr atoms, respectively. (c) High angle annular dark-field STEM image in the area shown with the broken square in (a).

Figure 7.3(a) shows a typical cross-sectional image of our device. The STEM image clearly shows that the c -axis of Ag_2CrO_2 is perpendicular to the Si substrate. Figure 7.3(b) is a closeup STEM image of the Ag_2CrO_2 device. We can see the clear stacked Ag_2 and Cr layers which is consistent with the schematic drawing of crystal structure shown in Fig. 2.5. At the surfaces of the Ag_2CrO_2 film, there are some Ag (or Ag_2O) grains as shown in Figs. 7.3(a) and 7.3(c). This indicates that a part of Ag is segregated, although there is no segregation of Ag inside the crystal. As shown in the upper-left side of Fig. 7.3(c), the segregated Ag part is continuously connected to the most top surface of the Ag_2CrO_2 flake, showing that the Ag layer is exposed after the fabrication.

7.3 Electrical transport measurements

7.3.1 Transport properties of Ag_2CrO_2 thin film

Our device is too tiny to perform the X-ray diffraction. Therefore, we checked the quality of the film by performing the transport measurement. Figure 7.4(a) shows the resistivity of the thin Ag_2CrO_2 film in Fig. 7.2(b) as a function of temperature. We note that this is a typical result among ten different thin Ag_2CrO_2 film devices. As in the case of normal metals, the resistivity decreases with decreasing temperature, but there is a large resistivity reduction at around $T = 25$ K. At 5 K, the resistivity ρ_{xx} of the thin Ag_2CrO_2 film reaches about $3 \mu\Omega\text{cm}$. Surprisingly, this resistivity is about ten times smaller than that ($\sim 36 \mu\Omega\text{cm}$) of the polycrystalline samples.

In order to see the difference between the thin film and the polycrystalline sample more clearly, the temperature dependence of $\rho_{xx}(T)$ normalized with $\rho_{xx}(T = 5 \text{ K})$ is plotted in Fig. 7.4(b). Apparently, the normalized resistivity for the thin film is much larger and sharper at T_N compared to the polycrystalline sample. To characterize the sudden reduction of ρ_{xx} at around T_N , we plot the derivative of the normalized resistivity for both the thin film and the polycrystalline sample in Fig. 7.4(c) [18].

The peak positions indicated by arrows are located at almost the same temperature (about 25 K), which is very close to $T_N = 24$ K determined from heat capacity measurements [14]. The peak width for the thin film is narrower compared to that for the polycrystalline sample. All the above results clearly show that the crystalline nature of the exfoliated thin Ag_2CrO_2 film is much better than that of the polycrystalline samples. Thus, the demonstrated fabrication process of the thin film Ag_2CrO_2 paves the way for device applications of layered antiferromagnetic materials.

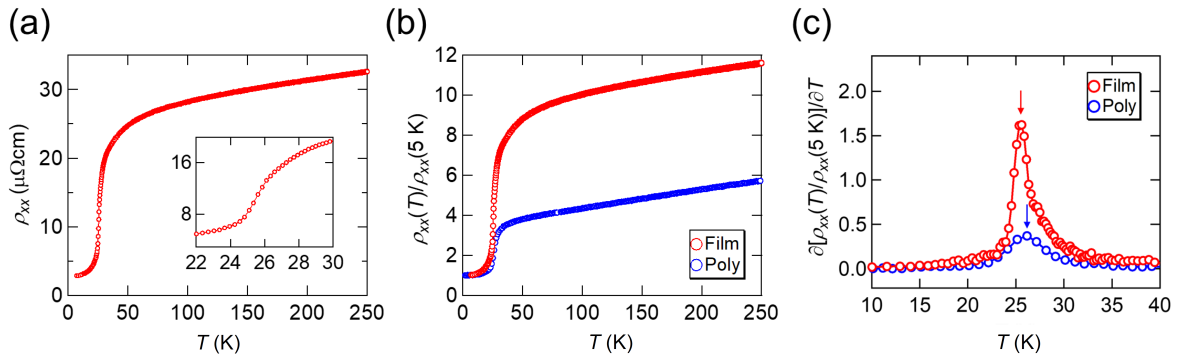


Figure 7.4: (a) Resistivity ρ_{xx} of 100 nm thick Ag_2CrO_2 film as a function of temperature. The inset is a closeup of the drastic change of ρ_{xx} near T_N . (b) Comparison of the normalized resistivity ($\rho_{xx}(T)/\rho_{xx}(5 \text{ K})$) between the thin film and the polycrystalline sample shown in Ref. [14] (c) $\partial[\rho_{xx}(T)/\rho_{xx}(5 \text{ K})]/\partial T$ vs T curves for the thin film and the polycrystalline sample. The arrows show the peak positions of the derivatives.

7.3.2 Magnetoresistance

For the Ag_2CrO_2 device, we performed MR measurements with three different magnetic field (B) directions, *i.e.*, x (in-plane along the current direction), y (in-plane perpendicular to the current direction), and z (out-of-plane along the c -axis, *i.e.*, $z \parallel c$) directions. Figure 7.5(a) shows the temperature dependence of the MRs, $\frac{\rho_{xx}(B) - \rho_{xx}(0)}{\rho_{xx}(0)}$, along the z axis.

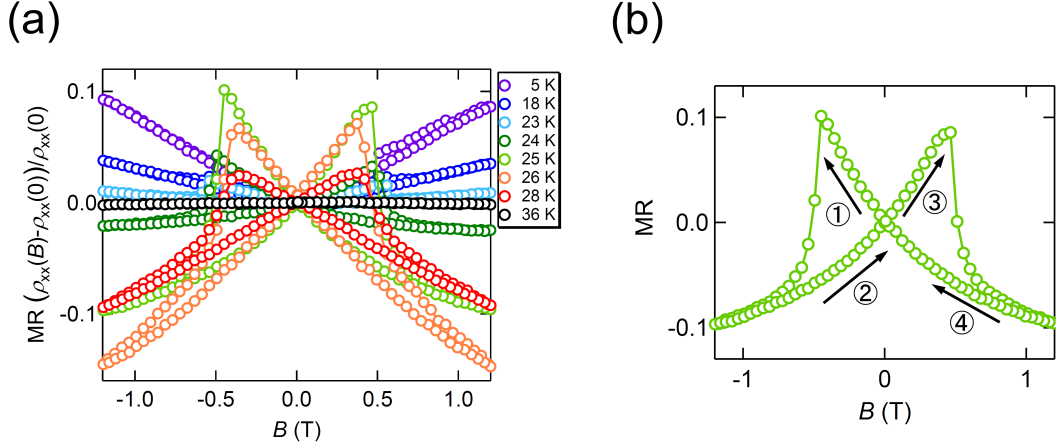


Figure 7.5: (a) MR curves along the z -axis at several different temperatures. The arrows and numbers in (b) indicate the order of the field sweep direction.

At $T = 5 \text{ K}$ ($\ll T_N$), a clear positive MR is observed at high magnetic fields. With increasing temperature, the positive slope becomes flatter. At 25 K ($\approx T_N$), the MR shows the negative sign. This trend is explained by the competition of two different mechanisms for MR, *i.e.*, the ordinary MR and the MR related to spin fluctuation. The positive MR at $T \ll T_N$ is related to the ordinary MR by the Lorentz force because the magnetic fluctuation is suppressed in this temperature region. On the other hand, when $T \sim T_N$, the magnetic scattering by thermal fluctuation of spins is enhanced. This contribution to the resistivity is suppressed by the magnetic field perpendicular to the plane, producing the negative MR.

Another unique feature is the butterfly-shaped MR at $B \approx \pm 0.5$ T. The amplitude of the butterfly-shaped MR is small when $T \ll T_N$. As we approach T_N , it becomes larger and takes a maximum at 25 K ($\approx T_N$). The maximum value reaches more than 10% at $B = 0.5$ T, which is unusually large for conventional ferromagnetic materials [147, 148]. As we raise the temperature further, the amplitude of the MR suddenly decreases and becomes zero above $T_m = 32$ K.

Figure 7.6 shows the MRs along the three directions measured at several different temperatures. In contrast to the MR along the z direction, such a drastic temperature dependence of MR has not been observed when $B \parallel x$ and $B \parallel y$, although a small negative MR can be seen below T_N . The B -angle dependence of the MR, which has never been studied for polycrystalline Ag_2CrO_2 , is another evidence that the micrometer-size thin Ag_2CrO_2 flake is most probably a single domain. This is also consistent with the STEM in Fig. 7.3.

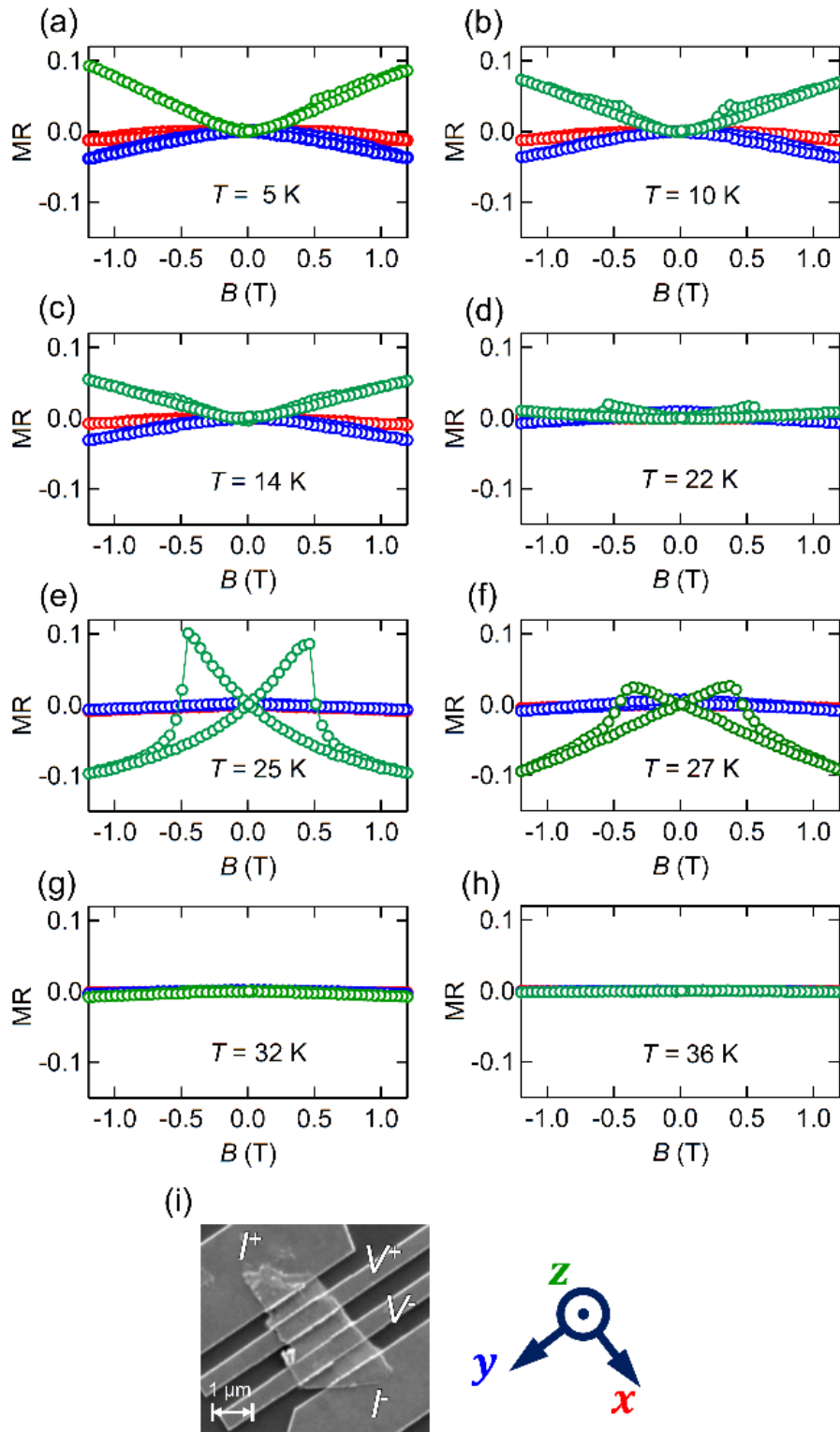


Figure 7.6: (a)-(h) MR curves at several different temperatures ($T = 5, 10, 14, 22, 25, 27, 32,$ and 36 K). The red, blue, and green curves show the MRs when B is applied along the x, y and z axes, respectively. The axes are defined as shown in (i).

To evaluate the butterfly-shaped MR observed only for $B\parallel z$, we define the amplitude of the butterfly-shaped MR, *i.e.*, $\Gamma \equiv \frac{\rho_{xx}^{\text{upper}}(B_c) - \rho_{xx}^{\text{lower}}(B_c)}{\rho_{xx}(0)}$ and the corresponding magnetic field (B_c), as illustrated in the inset of Fig. 7.7(a). Γ has a small value at low temperatures and takes a maximum (15%) at around T_N . It still has a finite value even above T_N and finally disappears at T_m . B_c in Fig. 3(b) is almost constant up to $T \approx 22$ K, and starts to decrease with increasing temperature and disappears at T_m .

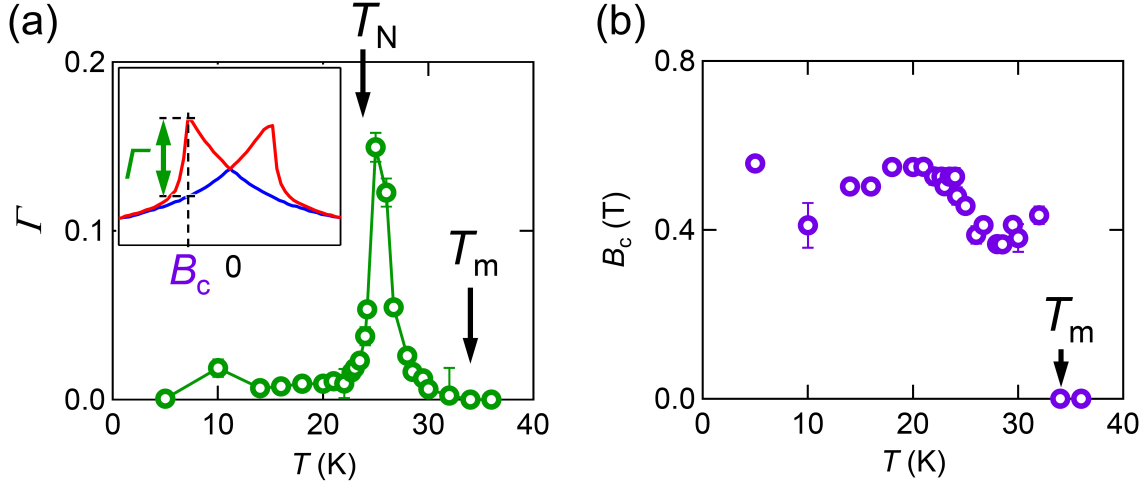


Figure 7.7: (a) The amplitude of the butterfly-shaped MR (Γ) as a function of temperature. The inset shows the definitions of Γ and B_c . The red and blue curves show ρ_{xx}^{upper} and ρ_{xx}^{lower} , respectively. (b) Temperature dependence of B_c .

Similar MR effects are often observed in ferromagnetic [147] and even antiferromagnetic [149], but the present butterfly-shaped MR is essentially different from them. MRs in conventional magnetic materials depend on the relative angle of magnetic domains, which is tuned by B . The amplitude of the MR is at most less than 1 % [148] at $B = 0.5$ T. It decreases with increasing temperature and becomes zero above the transition temperature. In the butterfly-shaped MR, however, Γ has a maximum value of 15 % near the transition temperature, which cannot be expected in conventional magnetic materials [147–149].

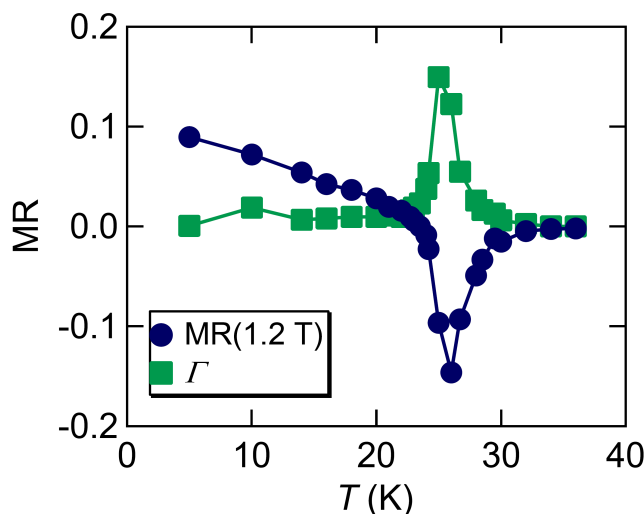


Figure 7.8: Temperature dependence of Γ and MR at $B = 1.2$ T.

Figure 7.8 shows Γ and MR at $B = 1.2$ T as a function of temperature. Apparently, the temperature at which Γ takes a maximum value corresponds to that at which the MR takes a minimum value. These experimental facts indicate that spin fluctuations of the PD state are strongly related to the butterfly-shaped MR.

7.3.3 Discussion: origin of the magnetoresistance

What is the origin of the butterfly-shaped MR? One naive consideration is that the PD spin switches at $B = B_c$. However, to polarize the PD spin with the external magnetic field, one needs more than 50 T, which is 100 times higher than the present B_c .² Here we recall that the ordered state has a finite magnetization below T_N . The nonzero magnetization is manifested in the MR curve proportional to B when $B \ll 1$ T, which is prohibited in an antiferromagnet with a combination of time-reversal and translational symmetry (Onsager's reciprocal theorem). We also recall that the butterfly-shaped MR in the present work appears only when $B \parallel c$. These features imply that the uniform magnetic moment is along the c -axis and has a strong uniaxial anisotropy. In such a situation, B suppresses the spin fluctuations when it is parallel to the moment direction, while B causes a spin flip when it is antiparallel to the moment direction. Thus, a negative and butterfly-shaped MR can be explained by the suppression of spin fluctuation and the spin-flip process induced by B , respectively.

²T. Kida and M. Hagiwara, private communications.

To verify the above argument, we consider a 2D ferromagnetic spin system with the Ising anisotropy. The experiments indicate that Ag_2CrO_2 has a finite magnetic moment with a strong anisotropy (Fig. 7.9).

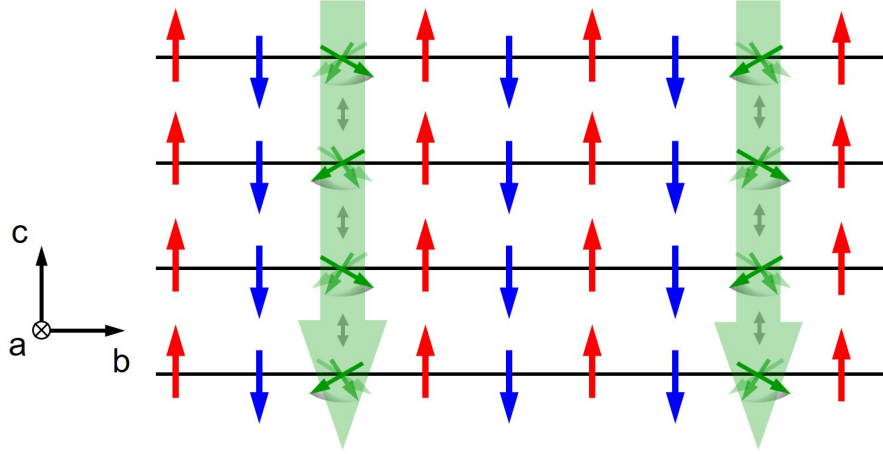


Figure 7.9: Schematic image of CrO_2 planes. If we assume a strong exchange interaction between the PD spins along the c -axis, the PD spins would behave as a quasi-one-dimensional chain along the c -axis.

Therefore, under a small magnetic field ~ 1 T, we assume that the ferromagnetic magnon well approximates the low-energy excitation states of Ag_2CrO_2 . The Hamiltonian is given by

$$\mathcal{H} = -J \sum_{\langle i,j \rangle} \mathbf{S}_i \cdot \mathbf{S}_j - \Delta \sum_i S_i^z S_i^z - B \sum_i S_i^z, \quad (7.1)$$

where $J(> 0)$ is the ferromagnetic exchange coupling between the nearest neighbor sites, $\Delta(> 0)$ is the Ising anisotropy, and i and j are the site numbers. B is applied perpendicular to the 2D plane (*i.e.*, $B \parallel c$). The uniaxial anisotropy lifts the Goldstone mode, producing a spin gap proportional to the anisotropy energy Δ ($\propto |B_c|$) (see the Appendix). For the positive magnetization, the spin gap increases (decreases) by applying the positive (negative) magnetic field and becomes zero when $B = B_c (< 0)$. The suppression of the magnetic fluctuation for $B > 0$ and the spin flip at $B = B_c (< 0)$ are intuitively explained by the spin gap modulated by B . The exactly same scenario is valid for the negative magnetization just by inverting the sign of B .

To see how B suppresses the MR, we compute the elastic scattering rate $1/\tau_{\text{mag}} \propto \rho_{xx}$ due to spin fluctuations at finite T by Born approximation:

$$\frac{1}{\tau_{\text{mag}}} \propto T \left\{ F_1 \left(2 + \frac{2\Delta + \mu_{\text{eff}} B}{2Jk_F^2 a_0^2} \right) - F_2 \left(2 + \frac{2\Delta + \mu_{\text{eff}} B}{2Jk_F^2 a_0^2} \right) \right\}, \quad (7.2)$$

where k_F is the Fermi wave number, μ_{eff} is the effective ferromagnetic moment, a_0 is the lattice constant between the neighboring effective ferromagnetic moments, $F_1(x) = \frac{1}{\sqrt{x^2 - 1}}$ and $F_2(x) = \frac{x}{\sqrt{x^2 - 1}} - 1$. A fit to the experimental data with Eq. (S8) is shown in Fig. 7.10; the butterfly-shaped MR near T_N is well-reproduced by the present theoretical model. The strong exchange interaction along the c -axis develops strong correlation of spins along the c -axis. Therefore, we assume that the quasi-one-dimensional chain along the c -axis behaves as a large single spin in our 100 nm thick sample. Since the lattice constant of the c -axis is 0.866 nm, the total effective magnetic moment μ_{eff} along the c -axis is estimated to be $\frac{100}{0.866} \times 0.4\mu_B \sim 45\mu_B$ where $0.4\mu_B$ is the effective magnetic moment per unit cell [14]. By assuming $k_F a_0 \sim 1$ (as in the case of a typical metal), both J and Δ are estimated to be about 10 K, which is comparable to T_N .

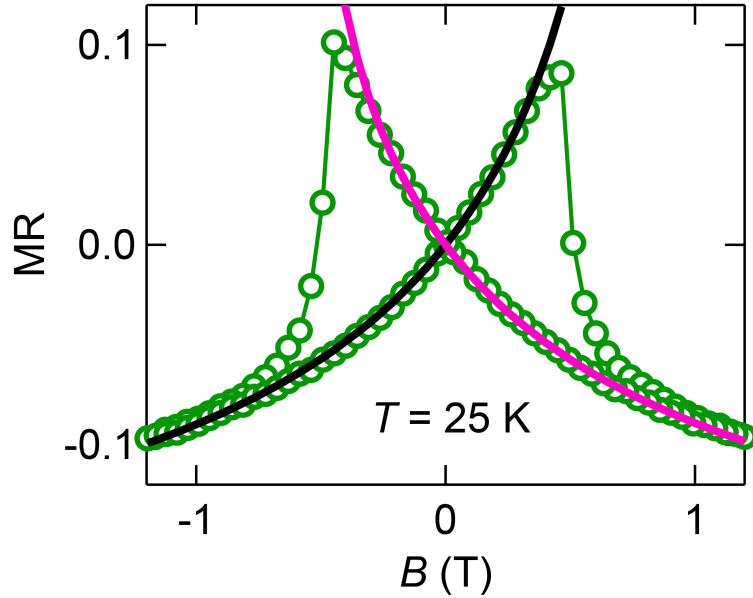


Figure 7.10: The fitting result of MR at $T = 25\text{K}$ with Eq. (S8).

7.3.4 Hall effect

Next, we fabricated Hall-bar devices and measured the Hall resistivity as shown in the inset of Fig. 7.11(a). The obtained Hall resistivity included a small component of the longitudinal resistivity, similar to the curve in Fig. 7.4. Thus, we plot the asymmetric component of the Hall resistivity ρ_{yx}^{asym} at three representative temperatures in Fig. 7.11(a). Note that ρ_{yx}^{asym} is quantitatively consistent with ρ_{yx} of polycrystalline Ag_2CrO_2 samples [60]. As mentioned in the introduction, a small fraction of magnetization in Ag_2CrO_2 was reported below T_N . Nevertheless, $\rho_{yx}^{\text{asym}} = 0$ at $B = 0$ in the whole temperature range. As shown in Fig. 7.11(b), on the other hand, ρ_{yx}^{asym} at $B = 1$ T has a cusp structure at $T_m = 32$ K where the butterfly-shaped MR disappears. The spin fluctuations also explain the enhancement of anomalous Hall resistivity near T_N .

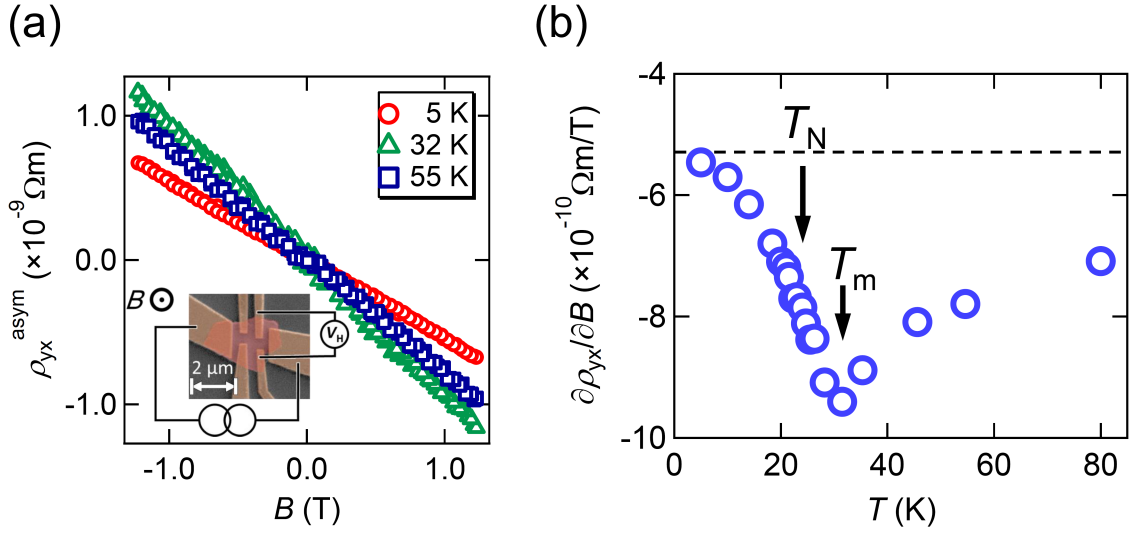


Figure 7.11: (a) ρ_{yx}^{asym} at typical temperatures ($T = 5, 32, 55$ K). The inset shows an SEM image of Ag_2CrO_2 device for the Hall measurement. (b) Temperature dependence of the derivative of ρ_{yx}^{asym} at $B = 0$. The broken line in (b) shows the contribution from the normal Hall effect, which is obtained from the data at the lowest temperature.

The similar AHE was observed in PdCrO_2 (Fig. 7.12) [150]. The crystal structure of PdCrO_2 is shown in the inset of Fig. 7.12.

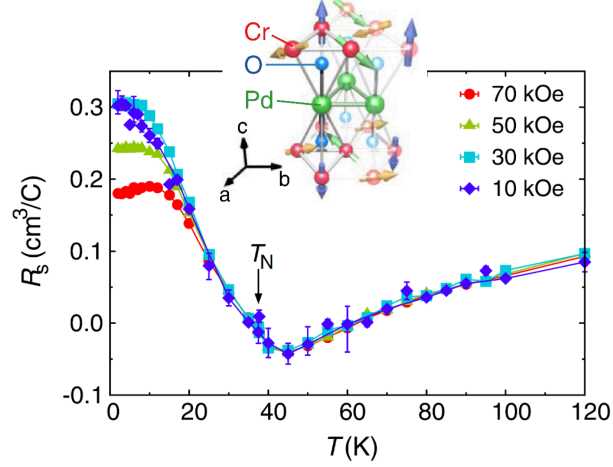


Figure 7.12: AHE in PdCrO_2 . The inset is the crystal structure of PdCrO_2 .

PdCrO_2 has a 120° spin structure with the canted Cr spins along the c -axis ($> 5^\circ$). The net magnetization of PdCrO_2 along the c -axis is small, but a canted spin component (or a spin scalar chirality) at the Cr sites generates such a large AHE. It is also known as the extrinsic topological Hall effect [151]. On the other hand, such a canted spin is not allowed in a conventional Ising model. However, a recent numerical study has found that the spin canting can be produced by the interfacial Dzyaloshinskii-Moriya interaction and the thermal fluctuation [153]. The temperature dependence of the extrinsic topological Hall conductivity shows the maximum around T_N . This temperature dependence is consistent with our Hall results (Fig. 7.13).

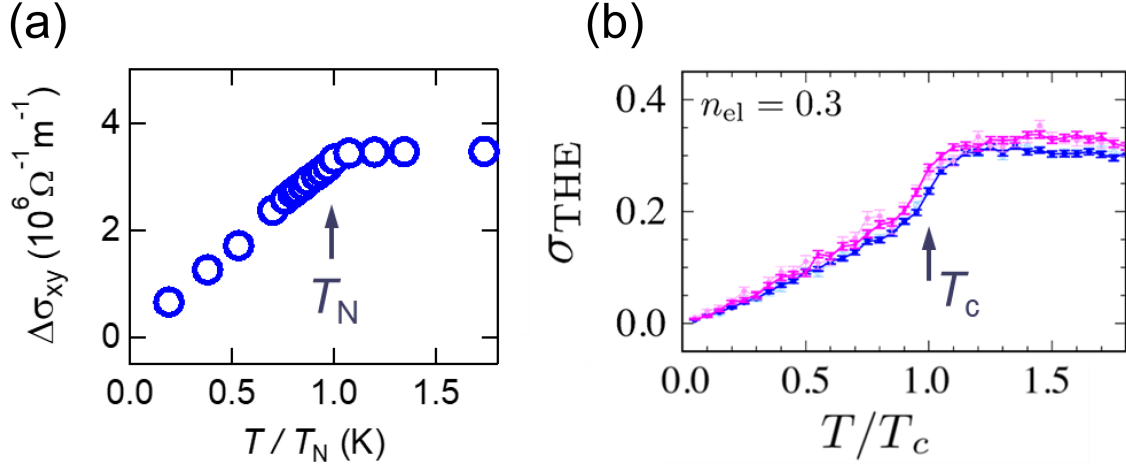


Figure 7.13: (a) Hall conductivity of Ag_2CrO_2 . $\Delta\sigma_{xy}$ has been calculated by subtracting the contribution of the ordinary Hall effect at $T \rightarrow 0$ from σ_{xy} at finite T . (b) The numerically calculated result of the extrinsic Hall effect [153]. n_{el} is the carrier density.

In the case of Ag_2CrO_2 , the uniaxial anisotropy is expected to suppress the canting, preserving the collinear state as the ground state, *i.e.*, no intrinsic topological Hall effect appears. In contrast, at finite T under a small B , the fluctuation of spins produces a finite scalar chirality because of the interfacial Dzyaloshinskii-Moriya interaction [152]. Since the crystal structure of Ag_2CrO_2 has a center symmetry, Dzyaloshinskii-Moriya interaction at the interface of crystals cannot be expected [154]. But a recent report on a Heisenberg magnet, the interfacial Dzyaloshinskii-Moriya interaction produced by the interface between the sample and the substrate cant the spin, potentially inducing a magnetic order with a finite scalar chirality [155]. Thus, the thickness dependence of the Hall effect is needed to investigate the interface effect between Ag_2CrO_2 and the Si substrate.

Chapter 8

Conclusions and perspectives

In this thesis, in order to clarify the magnetic dynamics of nanoscale frustrated magnets from the viewpoint of electric and spin conductivity measurements, we have performed spin transport measurements in ternary alloy spin-glass CuMnBi and magnetotransport measurements in Ag₂CrO₂ thin films. The following knowledge was obtained from the present work.

First of all, spin transport measurements have been performed using CuMnBi ternary alloy spin glasses to elucidate the relation between the spin current and spin fluctuations. For this purpose, we have investigated carefully the Mn concentration dependence of the ISHE and SDL. The SH angle of Cu_{99.5-x}Mn_xBi_{0.5} is constant in the temperature range $T > T^*$ corresponding to the paramagnetic state, but starts to decrease below T^* and eventually vanishes at the spin freezing temperature T_f of the spin glass nanowire. The determined T_f linearly increases with increasing the magnetic impurity concentration, as in the case of bulk spin glasses. In the temperature region of $T_f < T < T^*$, we have found the “spin treacle” regime, which has not been distinguished by other conventional experimental techniques for bulk spin glasses. This result is a demonstration of the usefulness of spin transport measurements in frustrated magnetic materials.

In addition, we found that the SDL of CuMnBi monotonously decreases with decreasing temperature regardless of some characteristic temperatures such as T^* and T_f . At much higher temperatures than T_f , the spin relaxation time τ_S follows a $(T - T_f)^2$ law which is different with the conventional spin diffusion theory in a metal. The origin of the temperature law has not still been unveiled, but the present result shows how quantitative characterization of magnetic fluctuations on nanometer-scale samples is possible using spin current, and raises an important issue about the role of magnetic localized moments in the spin diffusion process.

Secondly, we have established the fabrication procedure of Ag₂CrO₂ thin film device from the polycrystalline Ag₂CrO₂ sample. This method enables us to obtain a single crystal like material from the polycrystalline one and is useful for studying mesoscopic physics using such a complex material. The MR of the Ag₂CrO₂ sample have been measured. It turns out that the butterfly-shaped MR can be seen only when the magnetic field is applied along the c -axis. This fact indicates that the PD spins have a strong uniaxial anisotropy in Ag₂CrO₂. The butterfly-shaped MR takes a maximum value of 15 % at around the transition temperature, suggesting that spin fluctuations

are essential. The result is well-explained by the theoretical model based on the 2D magnetic system with the Ising anisotropy.

We have also found the additional Hall component in Ag_2CrO_2 to the ordinary Hall effect although the AHE does not appear in the conventional Ising system. The temperature dependence of the Hall coefficient has the same tendency as that of the butterfly-shaped MR. Thus, rich physics is further expected in such a magnetically frustrated system coupled to conducting electrons.

As the perspectives, the detailed origin of the spin treacle regime and the relation between T_f and T^* have not been fully understood yet. The origin of the temperature dependence of the SDL has not been explained either. To elucidate them, we need the detailed Mn concentration dependence of T^* .

In present work, we only investigated the CuMnBi ternary alloy system. Therefore, to check the universality of the spin treacle region, spin transport measurements in other spin glass systems are required. Recently, we have measured the inverse spin Hall effect in $\text{Au}_{78}\text{Fe}_{22}$ and the similar saturation has been observed (Fig. 8.1).

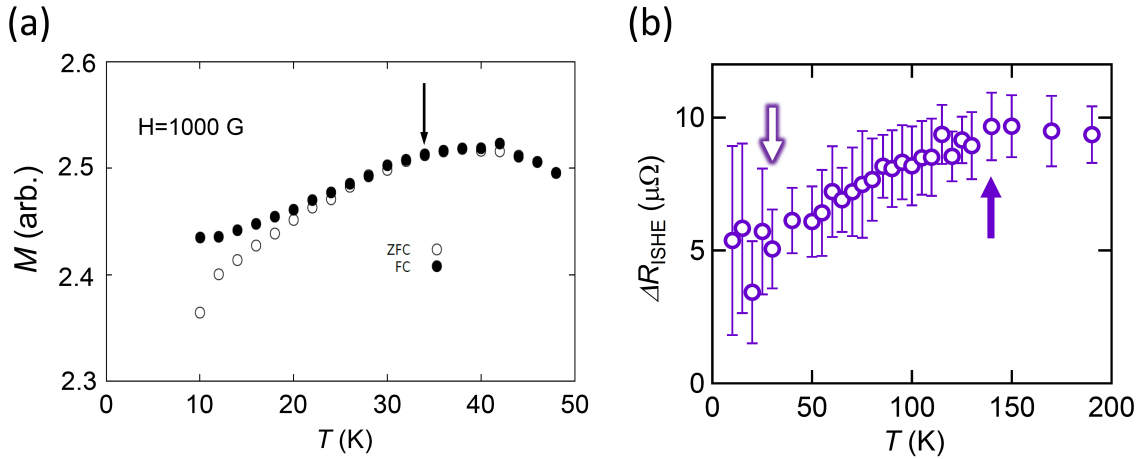


Figure 8.1: (a) *Dc* magnetization measurement of 20 nm thick $\text{Au}_{78}\text{Fe}_{22}$ film. The arrow indicates T_f . (b) The temperature dependence of ISHE in $\text{Au}_{78}\text{Fe}_{22}$. The open and solid arrows indicate T_f of nanowire and T^* , respectively.

This is a supportive result of the realization of the spin treacle region. To further establish the universality of the spin treacle regime in spin glasses, one has to make a test for the other concentrations of AuFe and also other combinations of host and impurity materials.

As for the 2D triangular antiferromagnetic system, we need to check whether the present theoretical model can explain a similar butterfly-shaped MR realized in other antiferromagnetic materials. We will also elucidate the mechanism of the Hall effect by measuring the film thickness dependence of the MR and the Hall effect.

We will integrate the Ag_2CrO_2 thin film into the SH device to perform the spin transport in the Ag_2CrO_2 thin film. Figure 8.2 is an SEM image of the prototype of the SH device with Ag_2CrO_2 .

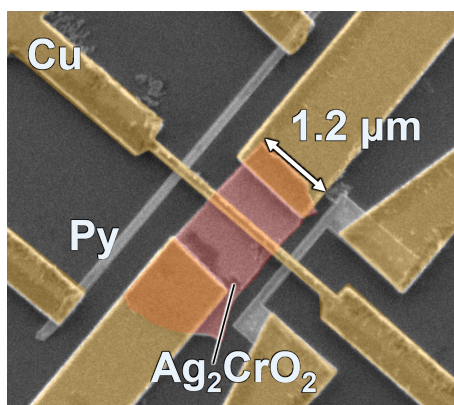


Figure 8.2: SEM image of the SH device with Ag_2CrO_2 .

An etching method such as Ar milling is usually used to produce a nanowire, but in order to avoid any damage by the Ar milling, a nanowire in this device has been formed by exfoliating Ag_2CrO_2 with the scotch tape. By measuring the spin transport in Ag_2CrO_2 , we will be able to obtain more information about the relation between a spin current and PD spins from the viewpoint of spin fluctuations. The SDL of Ag_2CrO_2 would also be an interesting issue.

Appendix

Theoretical calculation of magnetoresistance of Ag_2CrO_2

In this Appendix, we show detailed explanations on our theoretical calculation. As mentioned in the main text, we start with a 2D ferromagnetic spin system with the Ising anisotropy (see Eq. (7.1)). Due to this uniaxial anisotropy, a spin gap with the anisotropy energy 2Δ is generated, as shown in Fig. S3. For the positive magnetization, the spin gap increases (decreases) by applying the positive (negative) magnetic field. At $B = B_c (< 0)$, the spin gap becomes zero and the spin flip takes place.

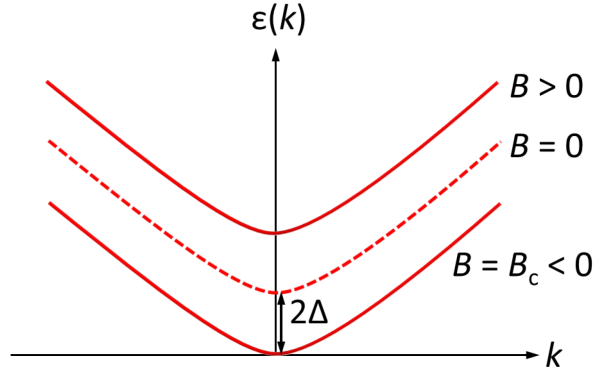


Figure S3: Dispersion relation of magnons with the uniaxial anisotropy for the positive magnetization. Because of the anisotropy energy 2Δ , the energy band is shifted and becomes zero when $B = B_c (< 0)$.

We expand the model in Eq. (7.1) to the quadratic order in S^x and S^y , assuming the S^x and S^y components are sufficiently small. Within this approximation, Eq. (7.1) reads:

$$\begin{aligned} \mathcal{H} &\sim \sum_{\vec{k}} [2J \{2 - \cos(k_x) - \cos(k_y)\} + 2\Delta + B] \left(S_{\vec{k}}^x S_{-\vec{k}}^x + S_{\vec{k}}^y S_{-\vec{k}}^y \right), \\ &\sim \sum_{\vec{k}} \omega_{\vec{k}} \left(S_{\vec{k}}^x S_{-\vec{k}}^x + S_{\vec{k}}^y S_{-\vec{k}}^y \right), \end{aligned} \quad (\text{S1})$$

where $J > 0$ is the ferromagnetic exchange coupling between the nearest neighbor sites, $\Delta > 0$ is the Ising anisotropy, B is the applied magnetic field along the z direction, \vec{k} is the wave vector, and $\omega_{\vec{k}} = Jk^2 + 2\Delta + B$ is the energy of the spin wave with momentum \vec{k} . Using Eq. (S1), we calculate the relaxation time originating from spin fluctuations, *i.e.*, τ_{mag} . The magnetoresistance (MR) due to the spin fluctuations is theoretically expressed with the B dependence of τ_{mag} :

$$\frac{\rho_{xx}(B) - \rho_{xx}(0)}{\rho_{xx}(0)} = \tau(0) \left(\frac{1}{\tau_{\text{mag}}(B)} - \frac{1}{\tau_{\text{mag}}(0)} \right), \quad (\text{S2})$$

$\tau_{\text{mag}}(B)$ is the relaxation time originating from the magnetic scattering and $\frac{1}{\tau(B)} = \frac{1}{\tau_{\text{mag}}(B)} + \frac{1}{\tau_{\text{imp}}}$ is the quasi-particle relaxation time (τ_{imp} is the relaxation time by impurity scatterings). We here assumed that the impurity scattering is insensitive to B ; the MR is a consequence of the B dependence of $\tau_{\text{mag}}(B)$.

τ_{mag} is obtained by using the scattering matrix $W_{\vec{k}\alpha \rightarrow \vec{k}'\beta}$:

$$\frac{1}{\tau_{\text{mag}}^\alpha(B)} = \sum_{\beta, \vec{k}'} W_{\vec{k}\alpha \rightarrow \vec{k}'\beta} \left(1 - \frac{v_{\vec{k}'\beta}^x}{v_{\vec{k}\alpha}^x} \right). \quad (\text{S3})$$

where $v_{\vec{k}\alpha}^x = k_x/m$ is the velocity of electrons with momentum \vec{k} and spin α (m is the mass of an electron and $\hbar = 1$). Here we assume that the electric field is applied along the x direction and the electron dispersion $\varepsilon_{\vec{k}} = k^2/(2m)$. Within the first Born approximation, $W_{\vec{k}\alpha \rightarrow \vec{k}'\beta}$ reads:

$$\begin{aligned} W_{\vec{k}\alpha \rightarrow \vec{k}'\beta} &\sim \frac{2\pi J_K^2}{N} \left\langle \left(\delta \vec{S}_{\vec{k}-\vec{k}'} \cdot \vec{\sigma}_{\beta\alpha} \right) \left(\delta \vec{S}_{\vec{k}'-\vec{k}} \cdot \vec{\sigma}_{\alpha\beta} \right) \right\rangle \delta(\varepsilon_{\vec{k}\alpha} - \varepsilon_{\vec{k}'\beta}), \\ &\sim \frac{2\pi J_K^2}{N} \delta_{\alpha\beta} \left\langle S_{\vec{k}-\vec{k}'}^x S_{\vec{k}'-\vec{k}}^x + S_{\vec{k}-\vec{k}'}^y S_{\vec{k}'-\vec{k}}^y \right\rangle \delta(\varepsilon_{\vec{k}\alpha} - \varepsilon_{\vec{k}'\beta}), \end{aligned}$$

where $\delta \vec{S}_{\vec{k}} \equiv \vec{S}_{\vec{k}} - S\hat{z}$, $\vec{S}_{\vec{k}} \equiv \frac{1}{\sqrt{N}} \sum_i \vec{S}_i e^{i\vec{k}\cdot\vec{R}_i}$, and J_K is the Kondo coupling between the itinerant electrons and the localized moments. The magnitude of spin fluctuation can be calculated within the linear spin wave approximation:

$$\langle S_{\vec{k}}^{x,y} S_{-\vec{k}}^{x,y} \rangle = \frac{1}{2\beta\omega_{\vec{k}}},$$

where $\beta = 1/T$ is the inverse temperature ($k_B = 1$) and a relation $\omega_{\vec{k}} = \omega_{-\vec{k}}$ is assumed. Therefore, $W_{\vec{k}\alpha \rightarrow \vec{k}'\beta}$ becomes:

$$W_{\vec{k}\alpha \rightarrow \vec{k}'\beta} \sim \frac{2\pi J_K^2 S}{N\beta\omega_{\vec{k}'-\vec{k}}} \delta_{\alpha\beta} \delta(\varepsilon_{\vec{k}\alpha} - \varepsilon_{\vec{k}'\beta}). \quad (\text{S4})$$

By substituting Eq. (S4) into Eq. (S3), the relaxation time due to spin fluctuation can be obtained as follows:

$$\frac{1}{\tau_{\text{mag}}^\alpha(B)} = 2\pi J_K^2 S T \int \frac{dk'^2}{(2\pi)^2} \frac{1}{\omega_{\vec{k}'-\vec{k}}} \left(1 - \frac{v_{\vec{k}'\alpha}^x}{v_{\vec{k}\alpha}^x} \right) \delta(\varepsilon_{\vec{k}\alpha} - \varepsilon_{\vec{k}'\alpha}). \quad (\text{S5})$$

By integrating over the Fermi surface, Eq. (S5) reads:

$$\begin{aligned} \frac{1}{\tau_{\text{mag}}^\alpha(B)} &= \frac{J_K^2 S m T}{2\pi} \int \frac{d\theta}{J\{(k_F^\alpha)^2 + (k_F^{\bar{\alpha}})^2 - 2k_F^\alpha k_F^{\bar{\alpha}} \cos \theta\} + 2\Delta + B} \left(1 - \frac{k_F^{\bar{\alpha}}}{k_F^\alpha} \cos \theta \right), \\ &= \frac{J_K^2 S m T}{2Jk_F^\alpha k_F^{\bar{\alpha}}} \left[F_1 \left(\frac{k_F^\alpha}{k_F^\alpha} + \frac{k_F^{\bar{\alpha}}}{k_F^\alpha} + \frac{2\Delta + B}{2Jk_F^\alpha k_F^{\bar{\alpha}}} \right) - \frac{k_F^{\bar{\alpha}}}{k_F^\alpha} F_2 \left(\frac{k_F^\alpha}{k_F^\alpha} + \frac{k_F^{\bar{\alpha}}}{k_F^\alpha} + \frac{2\Delta + B}{2Jk_F^\alpha k_F^{\bar{\alpha}}} \right) \right]. \end{aligned} \quad (\text{S6})$$

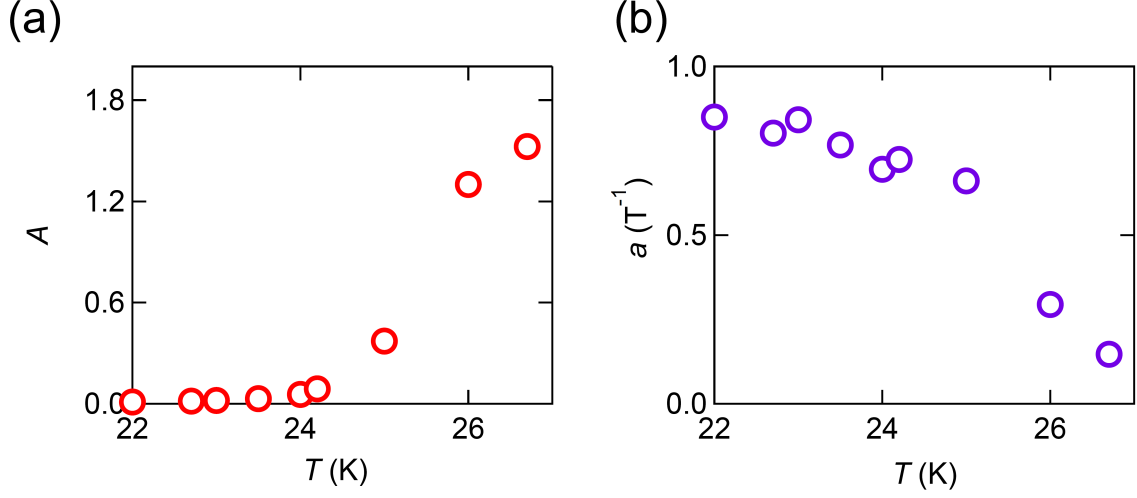


Figure S4: (a) Fitting result of the MR at $T = 25$ K. (b) A and (c) a obtained from the fitting with Eq. (S8).

Here the two functions F_1 and F_2 are $F_1(x) = \frac{1}{\sqrt{x^2 - 1}}$ and $F_2(x) = \frac{x}{\sqrt{x^2 - 1}} - 1$, respectively; α ($= \uparrow$ or \downarrow) and $\bar{\alpha}$ ($= \downarrow$ or \uparrow) denote the spin directions, and k_F^α is the Fermi wave number for spin α . Equation (S6) shows that the relaxation time due to spin fluctuation depends only on the Fermi wave number.

Since Ag_2CrO_2 has a small magnetic moment, it is reasonable to assume $k_F^\uparrow \sim k_F^\downarrow \sim k_F$. Therefore, we obtain the following expression for τ_{mag} :

$$\frac{\hbar}{\tau_{\text{mag}}(B)} \sim \frac{J_K^2 S m k_B T}{2Jk_F^2 a_0^2} \left\{ F_1 \left(1 + \frac{2\Delta + \mu_{\text{eff}} B}{2Jk_F^2 a_0^2} \right) - F_2 \left(1 + \frac{2\Delta + \mu_{\text{eff}} B}{2Jk_F^2 a_0^2} \right) \right\}, \quad (\text{S7})$$

which is the same as Eq. (7.2) in the main text. k_F is the Fermi wave number, μ_{eff} is the effective ferromagnetic moment, a_0 is the lattice constant between the neighboring effective ferromagnetic moments, In Eq. (S7), \hbar and k_B are explicitly written here to compare the experimental data. To fit the experimentally obtained MR curves with Eqs. (S2) and (S7), the following expression is useful:

$$\frac{\rho_{xx}(B) - \rho_{xx}(0)}{\rho_{xx}(0)} = A \left\{ \sqrt{\frac{aB_c}{aB_c + 2}} - \sqrt{\frac{a(B + B_c)}{a(B + B_c) + 2}} \right\}, \quad (\text{S8})$$

where A and a are fitting parameters. As shown in Fig. S4(a), the experimental data can be nicely fitted using Eq. (S8). We note that in principle Eq. (S8) can be used only in the vicinity of T_N . Figure S4 shows the obtained A and a values as a function of T . A is small below T_N and rapidly increases near T_N . On the other hand, a is more or less constant below T_N and rapidly decreases above T_N .

J and Δ can be estimated by using the following relations:

$$J = \frac{\mu_{\text{eff}}}{2ak_{\text{F}}^2 a_0^2}, \quad (\text{S9})$$

$$\Delta = \frac{B_c \mu_{\text{eff}}}{2}. \quad (\text{S10})$$

It should be stressed that Eqs. (S9) and (S10) give rough estimations for J and Δ , since in principle J and Δ should depend on all the microscopic details. As mentioned in the main text, the uniform magnetic moment is along the c -axis. In addition, we assume that the exchange interaction along the c -axis is much larger than that in the plane. Such a situation is common for antiferromagnets with partially disordered phases [156–158] and is necessary for a stable PD phase in Monte Carlo simulations [159, 160].

References

- [1] C. Lacroix, P. Mendels and F. Mira, *Introduction to Frustrated Magnetism* (Springer, Berlin, 2010).
- [2] H. T. Diep, *Frustrated Spin Systems* (World Scientific, Singapore, 2013).
- [3] K. Binder and A. P. Young, *Rev. Mod. Phys.* **58**, 801 (1986).
- [4] H. Kawamura and T. Taniguchi, “Spin glass” in *Handbook of Magnetic Materials*, **24**, (2015).
- [5] J. Sinova *et al.*, *Rev. Mod. Phys.* **87**, 1213 (2015).
- [6] Y. Niimi and Y. Otani, *Rep. Prog. Phys.* **78**, 124501 (2015).
- [7] M. I. D’yakonov and V. I. Perel, *JETP Lett.* **13**, 467 (1971).
- [8] J. E. Hirsch, *Phys. Rev. Lett.* **83**, 1834 (1999).
- [9] Y. K. Kato *et al.*, *Science* **306**, 1910 (2004).
- [10] E. Saitoh *et al.*, *Appl. Phys. Lett.* **88**, 182509 (2006).
- [11] S. O. Valenzuela and M. Tinkham, *Nature* **442**, 176 (2006).
- [12] D. H. Wei *et al.*, *Nat. Commun.* **3**, 1058 (2012).
- [13] Y. Niimi *et al.*, *Phys. Rev. Lett.* **115**, 196602 (2015).
- [14] H. Yoshida, E. Takayama-Muromachi and M. Isobe, *J. Phys. Soc. Jpn.* **80**, 123703 (2011).
- [15] M. Matsuda, C. de la Cruz, H. Yoshida, M. Isobe, and R. S. Fishman, *Phys. Rev. B* **85**, 144407 (2012).
- [16] J. Sugiyama *et al.*, *Phys. Rev. B* **88**, 184417 (2013).
- [17] K. S. Novoselov *et al.*, *Science* **306**, 666 (2004).
- [18] H. Taniguchi *et al.*, *AIP Advances* **8**, 025010 (2018).
- [19] T. Kadowaki and H. Nishimori, *Phys. Rev. E* **58**, 5355 (1998).

-
- [20] V. Cannella and J. A. Mydosh, Phys. Rev. B, **6**, 4220 (1972).
- [21] S. Nagata, P. Keesom and H. Harrison, Phys. Rev. B, **19**, 3, 1633 (1979).
- [22] C. Violet and R. Borg, Phys. Rev. **149**, 540 (1963).
- [23] H. Scheuer, J. B. Suck, A. P. Murani, and M. Löwenhaupt, J. Magn. Magn. Mater. **14**, 241 (1979).
- [24] T. Taniguchi H. Matsuyama, S. Chikazawa, Y. Miyako, J. Phys. Soc. Jpn. **52**, 4323 (1983).
- [25] S. F. Edwards and P. W. Anderson, Journal of Physics F: Metal Physics, **5**, 965 (1975).
- [26] D. Sherrington and S. Kirkpatrick, Phys. Rev. Lett. **35**, 1792 (1975).
- [27] G. Parisi, Phys. Rev. Lett. **43**, 1754 (1979).
- [28] G. Parisi, Phys. Rev. Lett. **50**, 1946 (1983).
- [29] D. J. Thouless, P. W. Anderson and R. G. Palmer, Philosophical Magazine, **35**, 593 (1977).
- [30] T. Taniguchi and Y. Miyako, J. Phys. Soc. Jpn. **57**, 3520 (1988).
- [31] J. Ferré, J. Rajchenbach and H. Maletta, J. of Appl. Phys. **52**, 1697 (1981).
- [32] L. E. Wenger and P. H. Keesom, Phys. Rev. B **13**, 4053 (1976).
- [33] I. A. Campbell, P. J. Ford and A. Hamzić, Phys. Rev. B **26**, 5195 (1982).
- [34] N. River and K. Adkins, J. Phys. F: Met. Phys. **5**, 1745 (1975).
- [35] I. A. Campbell, Phys. Rev. Lett. **47**, 1473 (1981).
- [36] L. R. Walker and R. E. Walstedt, Phys. Rev. Lett. **38**, 514 (1977).
- [37] L. R. Walker and R. E. Walstedt, Phys. Rev. B **22**, 3816 (1980).
- [38] T. Taniguchi *et al.*, Phys. Rev. Lett. **93**, 246605 (2004).
- [39] F. Wolff Fabris *et al.*, Phys. Rev. B **74**, 214201 (2006).
- [40] N. E. Israeloff, M. B. Weissman, G. J. Nieuwenhuys and J. Kosiorowska, Phys. Rev. Lett. **63**, 794 (1989).
- [41] T. Capron *et al.*, Phys. Rev. Lett. **111**, 187203 (2013).
- [42] G. H. Wannier, Phys. Rev. **79**, 357 (1950).
- [43] M. Mekata, J. Phys. Soc. Jpn. **42**, 76 (1977).

-
- [44] T. Nikuni and H. Shiba, J. Phys. Soc. Jpn. **62**, 3268 (1993).
- [45] S. Fujiki, K. Shutoh, Y. Abe and S. Katsura, J. Phys. Soc. Jpn. **52**, 1531 (1983).
- [46] D. P. Landau, Phys. Rev. B **27**, 5604 (1983).
- [47] H. Takayama, K. Matsumoto, H. Kawahara, and K. Wada, J. Phys. Soc. Jpn. **52**, 2888 (1983).
- [48] H. Kawamura, S. Miyashita, J. Phys. Soc. Jpn. **53**, 4138 (1984).
- [49] T. Takagi and M. Mekata, J. Phys. Soc. Jpn. **64**, 4609 (1995).
- [50] M. F. Collins and O. A. Petrenko, Can. J. Phys. **75**, 605 (1997).
- [51] S. Mitsuda, H. Yoshizawa, N. Yaguchi and M. Mekata, J. Phys. Soc. Jpn. **60**, 1885 (1991).
- [52] S. Mitsuda, N. Kasahara, T. Uno and M. Mase, J. Phys. Soc. Jpn. **67**, 4026 (1998).
- [53] M. Mekata *et al.*, J. Phys. Soc. Jpn. **62**, 4474 (1993).
- [54] K. Fushiya *et al.*, J. Phys. Soc. Jpn. **83**, 113708 (2014).
- [55] H. Nakamura *et al.*, J. Phys. Cond. Matt. **11**, 1095 (1999).
- [56] J. Rossat-Mignod *et al.*, Phys. Rev. B **16**, 440 (1977).
- [57] S. A. M. Mentink *et al.*, Phys. Rev. Lett. **73**, 1031 (1994).
- [58] H. Yoshida *et al.*, Phys. Rev. B **73**, 020408(R) (2006).
- [59] H. Yoshida *et al.*, J. Phys. Soc. Jpn. **77**, 074719 (2008).
- [60] T. Kida, A. Okutani, H. Yoshida and M. Hagiwara, Phys. Proc. **75**, 647 (2015).
- [61] W. Thomson, Proc. Roy. Soc. **8**, 546 (1857).
- [62] N. F. Mott, Proc. R. Soc. London, Ser. A **153**, 699 (1936).
- [63] E. H. Hall, Philos. Mag. **19**, 301 (1880).
- [64] R. Karplus and J. M. Luttinger, Phys. Rev. **95** (1954).
- [65] M. N. Baibich *et al.*, Phys. Rev. Lett. **61**, 2472 (1988).
- [66] G. Binasch, P. Grunberg *et al.*, Phys. Rev. B **39**, 4828 (1989).
- [67] J. S. Moodera *et al.*, Phys. Rev. Lett. **74**, 3273 (1995).
- [68] T. Miyazaki and N. Tezuka, J. Magn. Magn. Mater. **139**, 231 (1995).

-
- [69] S. Yuasa *et al.*, Nat. Mater. **3**, 868 (2004).
- [70] S. S. P. Parkin *et al.*, Nat. Mater. **3**, 862 (2004).
- [71] J.-G. (J.) Zhu and C. Park, Materialstoday **9**, 36 (2006).
- [72] S. S. Parkin *et al.*, J. Appl. Phys. **85**, 5828 (1999).
- [73] S. Tehrani *et al.*, J. Appl. Phys. **85**, 5822 (1999).
- [74] M. Pannetier-Lecoeur *et al.*, Appl. Phys. Lett. **98**, 153705 (2011).
- [75] M. Johnson and R. H. Silsbee, Phys. Rev. Lett. **55**, 1790 (1985).
- [76] F. J. Jedema, A. T. Filip and B. J. van Wees, Nature **410**, 345 (2001).
- [77] T. Kimura J. Hamrle and Y. Otani, Phys. Rev. B **72**, 014461 (2005).
- [78] T. Kimura *et al.*, Phys. Rev. Lett. **98**, 156601 (2007).
- [79] L. Vila, T. Kimura and Y. Otani, Phys. Rev. Lett. **99**, 226604 (2007).
- [80] T. Tanaka *et al.*, Phys. Rev. B **77**, 165117 (2008).
- [81] M. Morota *et al.*, Phys. Rev. B **83**, 174405 (2011).
- [82] C. Du *et al.*, Phys. Rev. B **90**, 140407 (2014).
- [83] E. Segasta and Y. Omori *et al.*, Phys. Rev. B (R) **94**, 060412 (2016).
- [84] T. Seki *et al.*, Nat. Mater. **7**, 125 (2008).
- [85] Y. Niimi *et al.*, Phys. Rev. Lett. **106** 126601 (2011).
- [86] Y. Niimi *et al.*, Phys. Rev. Lett. **109** 156602 (2012).
- [87] L. Zhu, D. C. Ralph and R. A. Buhrman, Phys. Rev. Appl. **10**, 031001 (2018).
- [88] B. F. Miao *et al.*, Phys. Rev. Lett. **111**, 066602 (2013).
- [89] S. M. Wu, J. Hoffman, J. E. Pearson and A. Bhattacharya, Appl. Phys. Lett. **105** 092409 (2014).
- [90] D. Tian *et al.*, Phys. Rev. B **94**, 020403(R) (2016).
- [91] K. S. Das, W. Y. Schoemaker, B. J. van Wees and I. J. Vera-Marun, Phys. Rev. B **96**, 220408(R) (2017).
- [92] J. D. Gibbons, D. MacNeill, R. A. Buhrman and D. C. Ralph, Phys. Rev. Appl. **9**, 064033 (2018).
- [93] M. Kimata *et al.*, Nature **565**, 627 (2019).

-
- [94] J. Kondo, Progress of Theoretical Physics **27**, 772 (1962).
- [95] B. Gu, T. Ziman, and S. Maekawa, Phys. Rev. B **86**, 241303(R) (2012).
- [96] R. S. Hayano *et al.*, Phys. Rev. B **20**, 850 (1979).
- [97] L. Frangou *et al.*, Phys. Rev. Lett. **116**, 077203 (2016).
- [98] R. Zhang and R. F. Willis, Phys. Rev. Lett. **86**, 2665 (2001).
- [99] D. Petti *et al.*, Appl. Phys. Lett. **102**, 192404 (2013).
- [100] Y. Ohnuma, H. Adachi, E. Saitoh, and S. Maekawa, Phys. Rev. B **89**, 174417 (2014).
- [101] Z. Qiu *et al.*, Phys. Nat. Commun. **7**, 12670 (2016).
- [102] A. Kundt, Ann. Phys. (Berlin) **285**, 257 (1893).
- [103] E. M. Pugh, Phys. Rev. **36**, 1503 (1930).
- [104] N. Nagaosa *et al.*, Rev. Mod. Phys. **82**, 1539 (2010).
- [105] D. J. Thouless, M. Kohmoto, P. Nightingale and M. den Nijs, Phys. Rev. Lett. **49**, 405 (1982).
- [106] T. Jungwirth *et al.*, Phys. Rev. Lett. **88**, 207208 (2002).
- [107] S. Onoda and N. Nagaosa, J. Phys. Soc. Jpn. **71**, 19 (2002).
- [108] K. von Klitzing, G. Dorda and M. Pepper, Phys. Rev. Lett. **45**, 494 (1980).
- [109] J. Smit, Physica (Amsterdam) **24**, 39 (1958).
- [110] C. Hurd, "The Hall Effect in Metals and Alloys" (1972).
- [111] A. Fert and O. Jaoul, Phys. Rev. Lett. **28**, 303 (1972).
- [112] S. P. McAlister, J. of Appl. Phys. **49**, 1616 (1978).
- [113] A. Hamzić, S. Senoussi, I. A. Campbell and A. Fert, J. Magn. Magn. Mater. **15-18**, 921 (1980).
- [114] J. L. Tholence and R. Tournier, J. de Phys. **32** Colloq. CI (1971) C1-211.
- [115] A. Fert, A. Friederich and A. Hamzic, J. Magn. Magn. Mater. **24**, 231 (1981).
- [116] L. Berger, Physica (Amsterdam) **30**, 1141 (1964).
- [117] L. Berger, Phys. Rev. B **2**, 4559 (1970).
- [118] A. Fert and P. M. Levy, Phys. Rev. Lett. **106**, 157208 (2011).

-
- [119] D. Hou *et al.*, Phys. Rev. Lett. **114**, 217203 (2015).
- [120] S. Onoda, N. Sugimoto and N. Nagaosa, Prog. Theor. Phys. **116**, 61 (2006).
- [121] S. Onoda, N. Sugimoto and N. Nagaosa, Phys. Rev. B **77**, 165103 (2008).
- [122] Y. Zhang, J. Železný, Y. Sun, J. van den Brink and B. Yan, **20**, 073028 (2018).
- [123] M. Seemann, D. Koedderitzsch, S. Wimmer and H. Ebert, Phys. Rev. B **92**, 155138 (2015).
- [124] G. Yin, Y. Liu, Y. Barlas, J. Zang and R. K. Lake, Phys. Rev. B **92**, 024411 (2015).
- [125] P. B. Ndiaye, C. A. Akosa and A. Manchon, Phys. Rev. B **95**, 064426 (2017).
- [126] S. Takahashi and S. Maekawa, Sci. Technol. Adv. Mater. **9**, 014105 (2008).
- [127] S. Takahashi and S. Maekawa, Phys. Rev. B **67**, 052409 (2003).
- [128] I. Žutić, J. Fabian and S. Das Sarma, Rev. Mod. Phys. **76**, 323 (2004).
- [129] R. J. Elliott, Phys. Rev. **96**, 266 (1954).
- [130] Y. Yafet, in Solid State Physics, edited by F. Seitz and D. Turnbull, (Academic, New York, 1963), Vol. 14.
- [131] T. Kimura, T. Sato and Y. Otani, Phys. Rev. Lett. **100**, 066602 (2008).
- [132] K.-W. Kim *et al.*, Phys. Rev. B **95**, 104404 (2017).
- [133] Kimura T. (2014) Lateral Spin Transport (Diffusive Spin Current). In: Xu Y., Awschalom D., Nitta J. (eds) Handbook of Spintronics. Springer, Dordrecht
- [134] J. M. Pomeroy and H. Grube, Appl. Phys. Lett. **105**, 094503 (2009).
- [135] V. K. Dugaev, P. Bruno and J. Barnas, Phys. Rev. B **64**, 144423 (2001).
- [136] A. A. Burkov and L. Balents, Phys. Rev. Lett. **91**, 057202 (2003).
- [137] P. J. Ford and J. A. Mydosh, Phys. Rev. B **14**, 2057 (1976).
- [138] P. Gibbs, T. M. Harden and J. H. Smith, J. Phys. F: Met. Phys. **15**, 213 (1985).
- [139] G. G. Kenning, J. M. Slaughter and J. A. Cowen, Phys. Rev. Lett. **59**, 2596 (1987).
- [140] C. Kittel, in *Introduction of Solid State Physics* 7th ed. (Wiley 1996).
- [141] J. C. Rojas Sánchez *et al.*, Nat. Commun. **4**, 2944 (2013).
- [142] Y. J. Uemura, *et al.*, Phys. Rev. B **31**, 546 (1985).

-
- [143] K. Okuda and M. Date, J. Phys. Soc. Jpn. **27**, 839 (1969).
- [144] D. L. Leslie-Pelecky *et al.*, J. Appl. Phys. **75**, 6489 (1994).
- [145] I. A. Campbell *et al.*, Phys. Rev. Lett. **72**, 1291 (1994).
- [146] Y. Yamasaki *et al.*, 2D Mater. **4**, 041007 (2017).
- [147] J.-E. Wegrowe *et al.*, Phys. Rev. Lett. **82**, 3681 (1999).
- [148] D. Zhang *et al.*, Phys. Rev. B **97**, 184433 (2018).
- [149] H. Masuda *et al.*, Sci. Adv. **2**, e1501117 (2016).
- [150] H. Takatsu *et al.*, Phys. Rev. Lett. **105**, 137201 (2010).
- [151] H. Ishizuka and N. Nagaosa, Sci. Adv. **4**, eaap9962 (2018).
- [152] H. Ishizuka and N. Nagaosa, New J. Phys. **20**, 123027 (2018).
- [153] Y. Kato and H. Ishizuka, Phys. Rev. Appl. **12**, 021001 (2019).
- [154] M. Bode *et al.*, Nature **447**, 190 (2007).
- [155] G. Chen *et al.*, Nat. Commun. **4**, 2671 (2013).
- [156] W. P. Lehmann, W. Breitling and R. Webe, J. Phys. C: Solid State Phys. **14**, 4655 (1981).
- [157] S. E. Nagler *et al.*, Phys. Rev. B **27**, 1784 (1983).
- [158] F. Matsubara, S. Inawashiro and H. Ohhara, J. Phys. : Condens. Matter **3**, 1815 (1991).
- [159] N. Todoroki and S. Miyashita, J. Phys. Soc. Jpn. **73**, 412 (2004).
- [160] O. Koseki and F. Matsubara, J. Phys. Soc. Jpn. **69**, 1202 (2000).

Acknowledgements

First and foremost, I would like to express my sincerest gratitude to Prof. Yasuhiro Niimi, the advisor of the author. He taught me many things necessary for research, including how to write documents, make a presentation and carry out research and how to manipulate equipment.

I would like to appreciate Prof. Kensuke Kobayashi for accepting me belonging to his group. His advice was always accurate and provided a good opportunity to consider essential natures of the research.

I thank Prof. Tomonori Arakawa for their guidance, discussions, suggestions on experimental techniques and physics.

I really appreciate Prof. Bo Gu, Prof. Timothy Ziman and Prof. Sadamichi Maekawa for fruitful discussions and suggestions about theoretical interpretations of spin transport measurements in spin glasses.

I also thank Prof. Toshifumi Taniguchi for magnetization measurements in spin glasses and teaching me about spin glasses.

I appreciate Prof. Hiroyuki Yoshida for providing us with the polycrystalline Ag_2CrO_2 and experimental suggestions.

I'm grateful to Prof. Hiroaki Ishizuka for theoretical interpretations and calculations of MR in Ag_2CrO_2 . Without his support, the results of Ag_2CrO_2 would not have been finalized. I would like to express my gratitude.

I thank Prof. Hirokazu Tada and Prof. Kohei Hamaya for the use of the lithography.

I really appreciate to Prof. Kawamura, Prof. Ogawa, and Prof. Kuroki for their agreements to be the second referees of this thesis. Thanks to their suggestions, the thesis was better organized.

I thank all the members of Kobayashi group for miscellaneous help. Especially, Mr. Shota Suzuki, Takashi Ibe, Masashi Tokuda and Mori Watanabe and Eria Imada supported my experiments. I also thank Ms. Junko Sasaki and Ms. Akiko Takao for helpful back-office tasks.

I appreciate financial aid by Support Center for Advanced Telecommunications Technology Research, Foundation, Osaka University Foundation for the Future and Murata Science Foundation.

Finally, I would like to express special gratitude to my dear family for providing support over the years.

Lists of publication

- [1] H. Taniguchi, S. Suzuki, T. Arakawa, H. Yoshida, Y. Niimi, and K. Kobayashi, “Fabrication of thin films of two-dimensional triangular antiferromagnet Ag_2CrO_2 and their transport properties”, *AIP Advances* **8**, 025010 (2018).
- [2] S. Suzuki, H. Taniguchi, T. Kawakami, M. Cosset-Cheneau, T. Arakawa, S. Miyasaka, S. Tajima, Y. Niimi, and K. Kobayashi, “Electrical contacts to thin layers of $\text{Bi}_2\text{Sr}_2\text{CaCu}_2\text{O}_{8+\delta}$ ”, *Applied Physics Express* **11**, 053201 (2018).
- [3] M. Tokuda, N. Kabeya, K. Iwashita, H. Taniguchi, T. Arakawa, D. Yue, X. X. Gong, X. F. Jin, K. Kobayashi, and Y. Niimi “Spin transport measurements in metallic Bi/Ni nanowires”, *Applied Physics Express* **12**, 053005 (2019).
- [4] H. Taniguchi, M. Watanabe, M. Tokuda, S. Suzuki, E. Imada, T. Ibe, T. Arakawa, H. Yoshida, H. Ishizuka, K. Kobayashi, and Y. Niimi “Butterfly-shaped magnetoresistance in triangular-lattice antiferromagnet Ag_2CrO_2 ”, *Scientific Reports* **10**, 2525 (2020).
- [5] H. Taniguchi, M. Watanabe, T. Ibe, M. Tokuda, T. Arakawa, T. Taniguchi, B. Go, T. Ziman, S. Maekawa, K. Kobayashi and Y. Niimi “Spin Treacle in a Frustrated Magnet Observed with Spin Current” submitted to *Physical Review Letters*.

Lists of presentations in international conferences

List only peer-reviewed and first author’s presentations at international conferences.

Poster

- [6] H. Taniguchi, M. Maki, T. Arakawa, T. Taniguchi, Y. Niimi, and K. Kobayashi “Strong suppression of spin Hall Effect in spin-glass metal” PASPS 9 (Kobe, Japan, August 2016)
- [7] H. Taniguchi, K. Yamagishi, T. Arakawa, T. Taniguchi, Y. Niimi, and K. Kobayashi “Extraordinary Hall effects and spin Hall effects in ternary alloy spin glasses” Spin TECH IX (Hakata, Japan, June 2017)

Oral

- [8] H. Taniguchi, T. Arakawa, T. Taniguchi, Y. Niimi, and K. Kobayashi “Disappearance of spin Hall effect in spin glass state due to strong spin fluctuation” PASPS22 (Osaka, Japan, December 2017)
- [9] H. Taniguchi, T. Arakawa, T. Taniguchi, Y. Niimi, and K. Kobayashi “Strong suppression of spin Hall effects induced by spin fluctuations” INTERMAG2018 (Marina bay sands, Singapore, April 2018)

-
- [10] H. Taniguchi, M. Watanabe, M. Tokuda, S. Suzuki, T. Ibe, T. Arakawa, H. Yoshida, H. Ishizuka, K. Kobayashi, and Y. Niimi “Butterfly-shaped magnetoresistance and topological Hall effect induced by spin fluctuations on triangular lattice” MMM Annual conference 2019 (Las Vegas, USA, November 2019)
- [11] H. Taniguchi, M. Tokuda, T. Taniguchi, T. Arakawa, B. Go, T. Ziman, S. Maekawa, K. Kobayashi, and Y. Niimi “Determination of Spin Freezing Temperature in Nanoscale Spin Glasses” MMM Annual conference 2019 (Las Vegas, USA, November 2019)

Award

- [12] IEEE Magnetic Society Best Student Presentation Award finalist (Marina bay sands, Singapore, 2018)